NANYANG TECHNOLOGICAL UNIVERSITY

Distributed Control and Power Quality Improvement in Hybrid AC/DC Microgrids

Jin Chi

School of Electrical & Electronic Engineering

2013

Distributed Control and Power Quality Improvement in Hybrid AC/DC Microgrids

Jin Chi

School of Electrical & Electronic Engineering

A thesis submitted to the Nanyang Technological University in partial fulfillment of the requirement for the degree of Doctor of Philosophy

2013

Acknowledgements

This thesis and related research work would not have been possible without the instruction and support of the following people.

First and foremost, I would like to express my sincere gratitude and appreciation to my supervisor, Assoc. Prof. Dr. Peng WANG who was abundantly helpful and provided invaluable assistance, support and guidance. The appreciation to Assoc. Prof. Dr. Peng WANG is not limited to his valuable research guidance. I would also like to appreciate his generous patience for my slower research progress due to my week background. In addition, He always gave me sufficient latitude to explore ideas and new areas. Beyond all that, I value the opportunities that he provided me to undertake a number of non-thesis related projects which broadened my background and enriched my professional experience.

Deepest gratitude is also due to the members of unofficial supervisory committee, Prof. Dr. Poh Chiang LOH, Aalborg University, Denmark, and Prof. Dr. Yang MI, Shanghai University of Electric Power, China. Without their knowledge sharing, guidance and assistance, this study would not have been successful. Special thanks are given to Prof. Dr. Poh Chiang LOH, who shared new research idea with me and taught me useful simulation and experiment skills.

My acknowledgement is then extended to Prof. Dr. Frede BLAABJERG and Jesep M. GUERRERO, Aalborg University, Denmark, for their valuable ideas and insightful comments on my research works during my visiting in Aalborg University as an exchange student. In particular, I would like to thank Professor Frede BLAABJERG for financial support in exchange student duration.

In the laboratory, I am equally thankful to Mr. Thomos FOO, Ms. Chia-Nge Tak HONG and Ms. Grace ONG from the Laboratory of Clean Energy Research, and Mr. Benny CHIA and Miss Christina WONG from the Laboratory of Water Energy Research, for their uncounted technical support in installations of academic software and setups of

experimental prototype.

I would also like to express my love and gratitude to my beloved families for their understanding and endless love through the duration of my studies. My parents have inspired me throughout my life and have taught me never to give up. My wife who was accompanying me in the last year of my PhD period has given me great support and encouragement. Deepest gratitude is again given to my beloved families because of their understanding and support during this period of struggle.

Last but not least, I would like to convey thanks to Nanyang Technological University for providing the financial support and laboratory facilities.

Table of Contents

Summary

Global concerns on fossil fuel depletion and environmental pollution have initiated an increasing demand for renewable energy such as solar, wind and fuel cells etc. More distributed generations (DGs) powered by renewable energy sources (RESs) will be entering into the existing electricity network in the near future. Clustering a few DGs, loads and storages together forms entities known as microgrids which merge advantages of individual DG units to arrive at an operating efficiency and system reliability that can never be attained by any single DG. Realization of those advantages accompanies the development of various essential power conditioning interfaces and their associated control for tying multiple DGs to the microgrids, and then tying the microgrids to the traditional power systems. Moreover, the intermittent characteristics of most green sources like photovoltaic (PV) arrays, wind turbines (WT) strongly rely on climatic or environmental condition, which makes RES uncontrollable. To overcome those inherent deficiencies, power electronics is the key enabling technology for the interconnection between RESs and the utility grid, providing more control flexibilities so as to fulfill system reliability and power quality requirements.

The proliferation of popular RESs like PV and fuel cells, and energy storages (ESs) like batteries and ultra-capacitors, which are all DC by nature, facilitates widespread application of DC microgrid in many industry systems, commercial buildings and residential complex. The advantages of DC microgrids include better compatibility, higher efficiency and robust stability. To cope with the stochastic nature of RESs, stable operation of a standalone DC microgrid with multiple DC sources, ESs and loads invariably involves the development of flexible and reliable control strategies for power balancing in both power generation and consumption ends. A coordination control scheme among multiple DC sources and ESs interfaces is implemented using a novel hierarchical control technique to maintain DC bus voltage within the limits while harvesting maximum renewable energy and prolonging storage lifetime.

Combining the DC microgrid and the dominated AC system forms the scenario — hybrid AC/DC microgrid, which would be, in concept, the presence of both DC and AC microgrids with sources, storages, loads and appropriate interlinking converters (ICs)

tied between them. Hybrid AC/DC microgrid has been becoming a popular concept to provide an effective solution for unlimited large-scale integration of various DGs and distributed storages (DSs) because of its higher efficiency and better compatibility. Normal operations of hybrid system include local energy management within each sub-grid and power exchange tuning between two sub-grids, which usually involve multi-layer supervision system and advanced energy management algorithm with vast communication links. However, it is impractical to linkup widely dispersed DGs through communication wirings. This would undoubtedly degrade system redundancy. The challenge is thus to avoid the wiring by developing appropriate decentralized control. With this in mind, a global power sharing (GPS) control is proposed to manage local power sharing (LPS) in individual sub-grid and GPS throughout the entire hybrid system.

Due to the load variations at the demand end and the intermittent renewable power at the supply end, the hybrid AC/DC microgrid can hardly be fully autonomous unless the DSs are placed for energy buffering, power balancing and fault riding-through. The storages, such as batteries, ultra-capacitors, flywheels etc., can be configured to behave in different manners according to specific microgrid applications and their respective features. Storages with high energy like batteries are usually placed for long-term system operation, serving as a controlled current source. While the high power storages like ultra-capacitors are usually controlled as a voltage source, maintaining system power balance in transient state. In this sense, different control schemes for DSs would undoubtedly increase the complexity of power management in hybrid AC/DC microgrid in spite of DS locations in AC or DC microgrid. Therefore, fulfilling the requirement of "plug-and-play" is getting difficult since all DSs are not controlled in a coincident way. To avoid the complexity of power management and enforce a coincident control scheme to DSs, a hybrid microgrid scenario with three buses including AC, DC, and DS buses is proposed. LPS in individual sub-grid, GPS throughout entire hybrid system and storage power sharing (SPS) among DS units are well elaborated. To restrain unexpected GPS behaviors and reduce the usage of DSs, a multi-level power exchange control strategy is developed to schedule the activation sequences among LPS, GPS and SPS.

The interlinking converter between AC and DC microgrids can be used not only to manage fundamental power flow among two sub-grids but also to serve as an active

power filter (APF), drawing harmonic current from AC to DC microgrid so as to improve the power quality in AC sub-grid. The ripple power injected into the DC microgrid results in voltage ripple in DC bus voltage, which is harmful for stable operation of DC system. A DC-link compensator (DLC) is therefore developed to sink the harmonic power, transferring it to auxiliary DLC. In this way, the variation of the DC bus voltage can be limited within an accepted band even with a relative smaller DC-link capacitance.

The hierarchical control scheme for standalone DC microgrids, the fully decentralized control for hybrid AC/DC microgrids, the distributed control for hybrid AC/DC/DS microgrids and power quality improvement for hybrid AC/DC microgrid have been verified in theory, simulation and experiment, and will definitely facilitate the application and development of hybrid AC/DC microgrid in low voltage distribution systems.

List of Figures

List of Tables

List of Abbreviations

AC	Alternative Current
ACwC	AC loads with Converter
APF	Active Power Filter
BESS	Battery Energy Storage System
BM	Bus Monitoring
CCC	Constant-Current Charging
CC-CV	Constant Current and Constant Voltage
CERTS	Consortium for Electric Reliability Technology Solutions
CPL	Constant Power Load
CSI	Current Source Inverter
CV	Constant Voltage
CVC	Constant-Voltage Charging
DAC	Digital-Analog Converter
DBS	DC Bus Signaling
DC	Direct Current
DER	Distributed Energy Source
DG	Distributed Generation
DLC	DC-Link Compensator
DS	Distributed Storage
DVD	Digital Video Disk
EMF	Electromotive Force
EMS	Energy Management System
ES	Energy Storage
ESR	Equivalent Series Resistant
ESS	Energy Storage System
EV	Electric Vehicle
GPS	Global Power Sharing
HL I	Hierarchical level I
HL II	Hierarchical level II
HL III	Hierarchical level III
HVDC	High Voltage Direct Current

IC	Interlinking Converter
ICC	Interrupted Charge Control
INC	Incremental Conductance
LED	Light-Emitting Diode
LPS	Local Power Sharing
MPP	Maximum Power Point
MPPT	Maximum Power Point Tracking
MTBF	Mean Time Between Failures
NRS	Non-Renewable Source
NTU	Nanyang Technological University
PCC	Point of Common Coupling
PI	Proportional-Integral
PLL	Phase Lock Loop
P&O	Perturb and Observe
PEV	Plug-in Electric Vehicle
PR	Proportional-Resonant
PV	Photovoltaic
RES	Renewable Energy Source
RMS	Root Mean Square
SoC	State of Charge
SPS	Storage Power Sharing
THD	Total Harmonic Distortion
VCO	Voltage Controlled Oscillator
VSD	Variable Speed Drives
VSI	Voltage Source Inverter
WERL	Water and Energy Research Laboratory
WT	Wind Turbines

Chapter 1 Introduction

1.1. Background and Motivations

During the last two decades, distributed generations (DGs), powered by various renewable and nonconventional micro-sources, have been gradually becoming an attractive option for configuring modern or future electrical grids because of the advantages of environmental friendliness, expandability and flexibility [1]. When a few DGs and loads are further clustered together, entities known as microgrids are formed, which in concept, are larger controllable distributed generators that effectively merge the advantages of various nonconventional sources to arrive at an operating efficiency and system reliability that can never be attained by any single micro-source [2, 3].

Accompanying this advancement in DG and microgrids is the development of various essential power conditioning interfaces and their associated control for tying the DGs in a microgrid, and between the microgrids and the traditional power systems [4, 5]. With such interconnection, the renewable energy sources with intermittent characteristics, such as photovoltaic (PV), wind and fuel cells, can be connected to the utility with stable operations under proper control scheme. Moreover, the microgrid operation is highly flexible, allowing it to freely operate in the grid-connected or islanded mode of operation [6-8].

So far, the applications of AC microgrids have been widely spread because of its main advantage of compatibility with the existing AC system infrastructure. This is understandable based on the dominant role that AC distribution has long served in the traditional grid. Although not rapidly developed, the applications of DC microgrid can also be found more than a decade back [9, 10], but its popularity has not grown much then, until the recent decade when the researches and applications of renewable energy have been rapidly developed [11-13]. Nowadays, the popularity of DC microgrids are growing further due to the proliferation of popular “green sources” like PV and fuel cells, and energy storages (ESs) like batteries and ultra-capacitors, which are all DC by nature. Given also that a huge portion of modern loads are electronic circuits that need

DC rather than AC supply, forming of DC microgrids might indeed be more efficient since less power conversion stages are required [14].

Being convinced of respective features of AC and DC microgrids, the natural idea is to form a more likely scenario — hybrid AC/DC microgrid, which would be the coexistence of both AC and DC microgrids with sources, storages and loads appropriately organized between them [12]. The two microgrids can then be tied together by proper interfacing converters, which preferably should be simple like the traditional six-switch half-bridge AC/DC converter with mature control schemes and proved stable performances in order to avoid unnecessary complexity and cost. This hybrid AC/DC microgrid can therefore provide an effective solution for integration of unlimited DGs, distributed storages (DSs) and various AC/DC loads with higher efficiency and better compatibility.

In general, reliable and economical operations of such a complex hybrid AC/DC microgrid usually depend heavily on local controllers for basic operations of power conditioning interfaces in the low layer and advanced energy management system (EMS) with mass information exchange in the high layer for overall system optimization. However, this kind of centralized control scheme may suffer degraded system redundancy during the malfunction of communication carriers [15]. What if the failures in communication networks occur? Is it possible to ride-through the communication failures? Or is there a solution for maintaining reliable operations without communication networks which can hardly be afforded and built up in the rural and remote areas?

With the above concerns in mind, the challenge is then to decentralize the control for DC sources, AC sources and interfacing converter so that the power flow is always appropriately managed within each microgrid as well as throughout the whole hybrid microgrid regardless of whether the load change happens in the AC, DC or both microgrids. Considering the power exchange between two microgrids, fully decentralized control however cannot be as straightforward as the decentralized control simply applied to DGs in single microgrid since power information in both microgrids cannot be easily gathered in a decentralized manner. Because of that, a rule of power

exchange between AC and DC microgrids under fully decentralized control needs to be developed. Although fully decentralized control gives the answer to the solution of previous concerns, system with decentralized control is however lack of optimal fashion since each power module is unaware of the others [16]. The follow-up thought is to explore an improved control strategy which is capable of not only managing the overall system power flow in decentralized manner, but also increasing the system optimal fashion to a certain degree. This challenge is therefore the core motivation of this research work.

1.2. Objectives

The focus of this Ph.D research work is the development of control schemes for reliable operations and power quality improvement of hybrid AC/DC microgrids. The main objectives of this research work are briefly summarized as:

- To discuss the feasibility of AC and DC microgrids and make a comparison between two types of microgrids in terms of economical, technical and environmental benefits of renewable based DGs.

- To give an overview of significant research on the efficiency advantages of DC distribution system over AC.

- To illustrate the infrastructure of hybrid AC/DC microgrids and address the accompanied advantages of combination of AC and DC microgrids.

- To give a comprehensive review of existing control schemes for wireless power sharing in distributed systems.

- To build up a practical DC microgrid in laboratory and develop associated control strategy for proper operations with respect to maximum energy harvest, effective battery management and utilization priority of renewable energy.

- To expand independent power sharing control in individual AC or DC microgrid to the hybrid system and develop a broadened wireless power sharing method throughout entire hybrid AC/DC microgrid.

- To develop a distributed control strategy for coordination operations between DGs and distributed storages in hybrid microgrids system.

- To investigate on the harmonic suppression in hybrid AC/DC microgrids and attempt to explore effective solutions [17].

- To extend the concept of active power filter in AC microgrids to DC microgrids and solve out the hybrid AC/DC active power filters.

1.3. Major Contributions

The main contributions of this research work can be summarized as follows:

1.3.1. A hierarchical controlled DC microgrid

A practical DC microgrid is developed in Water and Energy Research Laboratory (WERL) in Nanyang University of Technology, Singapore. The coordination control among multiple DC sources and ESs is implemented using a novel hierarchical control technique. The bus voltage essentially acts as an indicator of supply-demand balance. A wireless control is implemented for reliable operation of the grid. A reasonable compromise between maximum power harvest and effective battery management is further enhanced using coordination control based on a central EMS. The feasibility and effectiveness of the proposed control strategies have been eventually tested by a DC microgrid in WERL.

1.3.2. Global power sharing throughout a hybrid AC/DC microgrid

Power sharing issues of an autonomous hybrid microgrid have been investigated. The hybrid microgrid comprises DC and AC subgrids interconnected by power electronic interfaces. A global power sharing (GPS) control is developed to manage power flows among all sources distributed throughout the two types of subgrids, which is certainly

tougher than pre-existing power sharing methods developed for individual AC or DC microgrid. This broadened power sharing control relies on coordinated operation of DC sources, AC sources, and interlinking converters (IC), scheduling all sources to share the total load throughout the entire hybrid AC/DC microgrid. The proposed method has been verified in simulation and experimental tests. The hybrid microgrid concepts are likely to benefit renewable or nonconventional distributed generations (DGs), where both AC and DC sources are present.

1.3.3. Distributed control for autonomous operation of a hybrid AC/DC/DS microgrid

The hybrid system can hardly be fully autonomous if distributed storages (DSs) are not considered. Storages can be placed for energy buffering, power balancing and fault riding-through. A hybrid AC/DC/DS microgrid configuration is proposed based on the layout of hybrid AC/DC system. In this three-bus system, sources and storages with same type are placed together in the relevant bus. Storages with the coincident control scheme would beneficially reduce the complexities in coordination control among three buses. The wireless power management of such a complex AC/DC/DS system would certainly rely on the development of a distributed control strategy, which manages the power flow within each network and tunes the power exchanges amongst three networks. The proposed distributed control strategy for three-bus AC/DC/DS hybrid system has subsequently been verified in both simulation and laboratory-scale experimental results.

1.3.4. Hybrid AC/DC active power filter for power quality improvement in a hybrid AC/DC microgrid

In a hybrid AC/DC microgrid system, the ICs interconnecting AC and DC microgrids can also operate as shunt active power filters (APF) to buffer harmonic power generated from the AC side. The shunt APF usually employs very large electrolytic capacitors in DC bus to maintain relatively constant DC bus voltage. These capacitors are however known to be bulky, suffering from expensive cost and short lifetime. A DC-link compensator (DLC) is developed to eliminate harmonic power in DC bus and very small electrolytic capacitors or even film type capacitors can be used instead. The DC side power quality can therefore be improved with proper design of DLC which is

constructed with small passive components and features very simple circuit configuration. Finally, simulation and experimental results are provided to prove that the proposed DLC concept can be a very promising harmonic solution for industrial applications of APFs.

1.4. Organization

This thesis is composed of seven chapters including this introductory chapter. The following six chapters are arranged as follows:

Chapter 2 introduces the concept of hybrid AC/DC microgrid as well as its main advantages. After a brief review of DGs and microgrids, the feasibility of AC and DC microgrids are compared. An example of hybrid AC-DC microgrids structure is then described in order to address the potential aims of a test bed hybrid microgrid. Finally, the main advantages of proposed hybrid AC/DC microgrid have been summarized.

Chapter 3 presents the implementation of a hierarchical control scheme for reliable operation of a standalone PV/battery based DC microgrid. The layout of a standalone DC microgrid is first described. The proposed hierarchical control applied to the DC system is then analyzed. Control structures of each power module for different modes of operations are subsequently obtained. Finally, the effectiveness of the proposed hierarchical control scheme has been experimentally verified through a lab-scale DC microgrid.

Chapter 4 proposes a GPS control for active power sharing of an autonomous hybrid AC/DC microgrid. The hybrid AC/DC structure is first introduced. The rudimentary droop control and its improved variants are reviewed. The power sharing in individual AC and DC sub-grid are then described. Upon accurate power sharing in both sub-grids, the principle of GPS is elaborated with the help of mathematical and graphical explanations. Finally, the simulation and experiment results have been provided to prove the effectiveness of the proposed control scheme for active power sharing of an autonomous hybrid AC/DC microgrid.

Chapter 5 proposes a distributed control for autonomous operation of hybrid

AC/DC/DS microgrid. The infrastructure of a three-bus hybrid AC/DC/DS microgrid is first described. To maintain reliable operation and achieve improved optimal degree, a distributed control scheme including a fully decentralized control for reliable operation of overall hybrid system and a multi-level power exchange control for optimal degree improvement is then introduced. Finally, simulation and experiment results are provided to show the effectiveness of the proposed distributed control stragety.

Chapter 6 proposes hybrid AC/DC active power filters which includes a conventional three-phase three-wire shunt APF for harmonic attenuation in AC microgrid and an active DC power filter — DLC for harmonic power decoupling in DC-link. In this chapter, the principle of shunt APF is first reviewed and a common problem inherent in the existing shunt APF applications is addressed. To illustrate this common accompanied problem, the minimum requirement of DC-link capacitance for three-phase three-wire shunt APF is then analyzed. In order to resolve the issues caused by the common inherent problem of shunt APF, the concept of DLC and its operation principle are subsequently explained. To verify the effectiveness of proposed hybrid AC/DC APF, comprehensive simulation and experimental results have been finally carried out.

Finally, Chapter 7 concludes this research work and proposes future research work based on the achievements of this work.

Chapter 2 Concept of Hybrid AC/DC Microgrid

2.1. Introduction

Alternative current (AC) has been the dominant power supply medium for over a century since the end of "the war of currents" [18] in which Thomas Edison and George Westinghouse became adversaries due to Edison's promotion of direct current (DC) for electric power distribution over AC advocated by Westinghouse. War of the currents was ultimately won by AC, and has been the platform for electrical transmission across the world since then. The key behind AC's victory was the invention of the transformers which could easily step-up the voltage levels for long distance power transfer with lower transmission losses. The points of AC being the standard choice include easier transformation into different levels for various applications, capability of long distance power transmission and inherent characteristics from the fossil energy driven rotating machine. AC power system gradually became the top engineering achievement of the 20^{th} century. However, problems along with the development, such as high energy costs, aging of current power system infrastructure and limited funds to construct new large power plants and long distance transmission lines, constraint the meet of the growing energy demands.

On the other side, the advantage of DC transmission was re-recognized accompanied with the progress of advanced power electronics techniques. The major application is power electronics-based high voltage DC (HVDC) transmission, which integrates DC penetration inside AC-dominated transmission networks. Since the past two decades, DC grids have shown resurgence due to the development and deployment of renewable DC power sources and their inherent compatibility for various DC loads in industrial systems [19, 20], commercial buildings [13, 21] and residential complex [22-25]. Reasons of the gaining popularity for DC grids include better compatibility [26-28], higher efficiency [29-32] and robust stability [33-36]. The shift from AC to DC system facilitates easier control of individual load performance, increased integration of renewable energy sources (RESs) and distributed energy storages [37]. This trend calls for a re-examination of the traditional AC power system structure and its efficiency. An alternative solution might be the hybrid AC/DC power system,

coexisting both AC and DC systems based on existing AC infrastructure.

This Chapter first reviews the distributed generations (DGs) and microgrids. The feasibility of AC and DC microgrids are then overviewed in Section 2.3. Section 2.4 subsequently introduces the hybrid AC/DC microgrids concept as well as its main advantages over individual AC or DC microgrids. The follow-up is an example of hybrid AC-DC microgrids structure with detailed description in order to address the potential aims of a test bed of a hybrid microgrid. Finally, conclusions are drawn in the last section.

2.2. Review of Microgrids

2.2.1. Distributed generation

Several definitions of DG have been found in the literatures [38-40]. Among those, one general and commonly used definition suggested in [38] is "distributed generation is an electric power source connected directly to the distributed network or on the customer side of the meter." Other DG definitions in terms of DG names, ratings and power delivery area are summarized as below [39]:

- DG names: Distributed generation is named "dispersed generation" in North America, while the corresponding terms used in South American countries, Europe and some Asian countries are called "embedded generation" and "decentralized generation", respectively.
- DG rating: There is no common DG rating definition since the maximum capacity of a grid connected DG depends on the distribution system's capacity and its voltage level. However, some technical issues related to DG can vary significantly with the rating. Therefore, the following distinction for DG rating are usually suggested [38]:
    1) Micro distributed generation: ~1 Watt < 5 kW;
    2) Small distributed generation: 5 kW < 5 MW;
    3) Medium distributed generation: 5 MW < 50 MW;
    4) Large distributed generation: 50 MW < ~300 MW.

- DG power delivery area: The definition for DG power delivery area has not yet been specified, but normally the energy produced from DG is supposed to be consumed within the distributed network. In some cases, if DG produced energy exceeds the distribution network load demand where DGs are installed, DGs can feed back some of their generated electric power to the transmission system.

The definition of DG has been gradually specified with the development of the technologies and applications in the past two decades. Nowadays, technological innovation, the changing economic and regulatory environments have resulted in a renewed interest for DG [40]. In addition, DG encompasses a wide variety of new and emerging technologies that utilize an equally wide array of renewable and non-conventional micro-sources, including fuel cells, photovoltaic cells, wind turbines, and microturbines, etc. Those green sources offer competitive generation options and promise better economics with high reliability, high efficiency and reduced emissions. Another factor that contributes to this evolution is power electronic technologies, which provide DGs controllable and flexible interface to the utility grid.

DG applications in distribution systems have many benefits [41]. In summary, a DG system responds to the increasing power demands and pollution emission concerns while providing low cost, reliable energy. To reduce the emissions, DG system can produce the power with high efficiency by introducing "green", renewable micro-sources. Moreover, to enhance productivity, DG system is able to improve system reliability and quality of power delivered by employing various power electronics with flexible controllability. Although both the customer and supplier can benefit a lot from the DG application, there still exist some technical limits and challenges in reality and extension on DG application.

On the one hand, DGs must meet various operating criteria with reliable, dispatchable, of the proper size and at the proper locations. On the other hand, there will be several emerging power quality issues related to the installation of DG to the conventional power system, such as voltage regulation, voltage flicker, harmonic distortion and other factors [42]. In addition, protection malfunctions such as breaker reclosing problem,

over-current protection and relaying interference may be misapplied with the installation of DGs [1, 43]. With regards to sudden connection and disconnection of DGs, the steady-state and transient stability of distributed power system may be degraded and it may also damage the customer facilities as well as the DG itself, and thus, lead to some safety concerns [19, 44].

2.2.2. Microgrid systems

Although the penetration of DGs at medium and low voltages is largely increasing all over the world, controlling a potentially huge number of DGs creates a daunting new challenge for operating and controlling the network safely and efficiently [45]. To overcome these problems [1], an effective solution is to cluster the loads, DGs and power electronic interfaces together, forming the architecture of so called microgrids [46]. The Microgrid is becoming more attractive, since it can optimally group DG systems to effectively merge advantages of various nonconventional sources to arrive at an operating efficiency and system reliability that can never be attained by any single micro-source [3, 45]. The concept of microgrid, discussed in [46], is described as a essentially combination of generation sources, loads and energy storage, interfaced through fast acting power electronics. Then, this combination of units is connected to the distribution network through a single point of common coupling (PCC) and appears to the power network as a single unit.

The standardized definition for microgrid has been originally made by an US organization named Consortium for Electric Reliability Technology Solutions (CERTS). It defines the microgrid as a cluster of loads and micro-sources operating under a unified controller within a certain local area [3]. CERTS is also concentrating on the research of distributed energy sources integration, integration of battery-based energy storage element and energy management system (EMS) in microgrid and has made great contribution to these research areas [47-49]. In a broad sense, microgrids are tiny power systems which integrate various components such as controlled and uncontrolled loads, DG units and storage elements coordinately operating together with controlled power electronics devices.

Being systematic organization of DG systems, microgrids are treated as controlled

entities, operating as dispatchable generators or loads to provide power or meet the needs of upstream networks with regard to the utility side. Microgrids can merge various renewable energy sources which can offer higher efficiency and environmental friendly energy compared to conventional power systems. For the customers, microgrids can contribute to local special demands in thermal and electricity needs as well as power quality improvement in terms of local voltage and frequency regulation. They feature uninterruptible power supply functions for critical loads and become the suitable candidate to provide energy in rural areas where transmission and distribution system hardly reach out [50].

2.3. AC Microgrids versus DC Microgrids

Based on the properties of sources and loads applied to construct the microgrids and the manners of power delivery, existing power distribution architectures can be generally classified into dominated AC microgrids, resurgent DC microgrids and emerged hybrid AC-DC microgrids. The feasibility of AC and DC microgrids are described and compared in this section, the hybrid AC-DC microgrid as well as its main advantages are then introduced in the following section.

2.3.1. Feasibility of AC microgrids

In spite of the initial widespread use of DC systems, they were almost completely superseded by AC systems due to its apparent limitations of short-distance power transmission capability [26]. In general, the AC system had won over the DC system for several reasons. First, the voltage levels can be easily transformed in AC systems, thus providing the flexibility of different voltages for generation, transmission, and consumption. Secondly, AC generators are much simpler than DC generators while the AC motors are much simpler and cheaper than DC motors. Due to the predominately AC electrical transmission and distribution system, the integration of the AC microgrid thus can bring remarkable benefits to the conventional power system. For instance, it can utilize the RESs to reduce the pressure on the shortage of fossil energy. The AC microgrids can also be extended to the rural area where the distributed power system is difficult to build. Furthermore, it can produce reliable power electricity to local load in case of the occurrence of disturbances and it is disconnected from the mains grid

working in the islanding mode [51, 52].

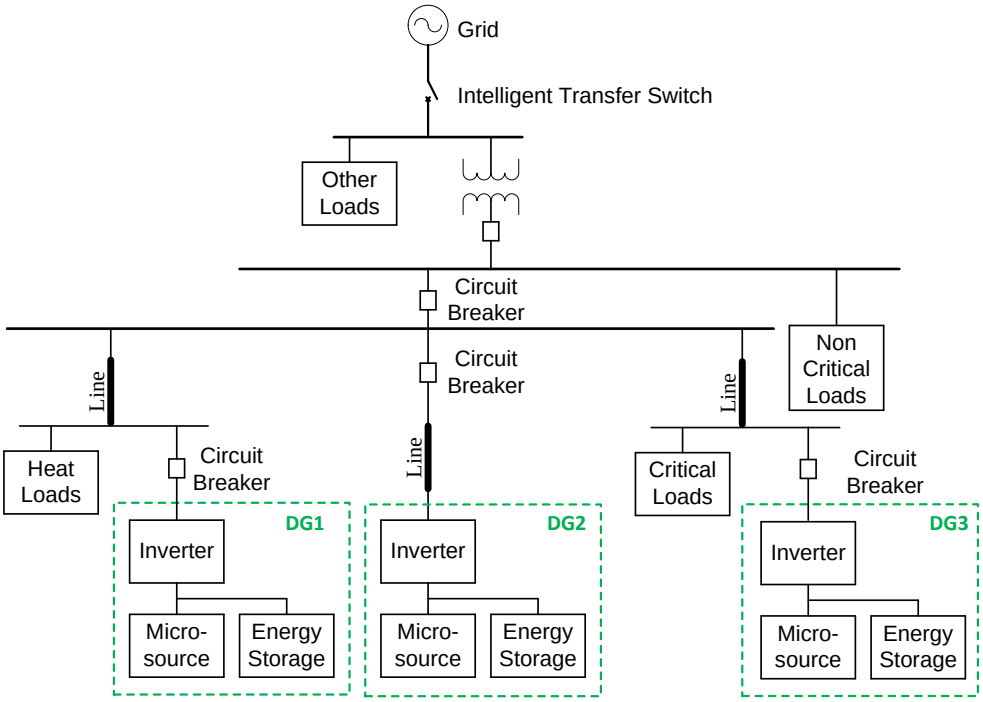

Figure 2.1. Basic AC microgrid structure.

A typical example of an AC microgrid is shown in Figure.2.1. The microgrid is connected to the mains through an intelligent transfer switch, allowing it freely to operate in both grid-connected and islanded modes. Three DG systems with global and their local loads are drawn in Figure 2.1. Each DG unit can be generally formed by a micro-source (e.g. microturbines, photovoltaic, wind turbines, and fuel cells etc.), a power conditioning interfaces (inverter in this system) and an energy storage device. DG1 is installed for supplying a heat load, while DG2 and DG3 are connected to the corresponding bus, responsible for both voltage regulation and load support. Typical examples of AC powered household loads are the washing machine, refrigerator, microwave oven, dishwasher, etc. In between each DG unit and a bus, there is a circuit breaker for fault protection in the microgrids or from the grids. This kind of microgrid structure feature less losses, local voltage and power support and flexible power flow control.

2.3.2. Feasibility of DC microgrids

The debate on use of DC as a power distribution alternative has been rousing for decades

[34]. Recently, it has been well-proven that the DC microgrid becomes more attractive and has been gaining much popularity over AC microgrid in industry systems, commercial buildings and residential applications. The potential advantages of DC microgrid can be summarized in following aspects:

1) Better compatibility: modern electrical loads are primarily constituted by variable speed drives (VSD), lighting, computers and servers in data centers, and plug-in electric vehicle (PEV), which are more compatible with operating at DC voltage [27, 31]. On the other hand, most RESs including PV arrays, and fuel cells, as well as energy storages like batteries and ultra-capacitors are DC by nature. DC power architectures therefore seem to have great potential for increased compatibility with high penetration of RESs.
2) High efficiency: in traditional AC microgrid, most of the loads found in various commercial and residential installations require front end AC-DC conversion devices. Various storage systems and renewable sources interact with these loads and the AC microgrid through DC-AC converters. These multistage power conversions in both supply-demand ends cause power losses with reduced system efficiency [12, 30, 31, 53]. It is investigated in [30] that losses of a DC microgrid system for residential appliance are around 15% lower than the losses in AC system for the same system configuration.
3) Better Stability: in AC system, both the voltage amplitude and frequency (or phase angle) control are required, which results in synchronization and stability issues. In DC system, the only electrical quantity that should be taken care of is DC bus voltage. Therefore, the absent of reactive power in DC microgrid gives rise to more straightforward stability assessment as well as lower losses in the cables [34].
4) Higher reliability: Most components in DC microgrids have relatively lower mean time between failures (MTBF), which indicates a higher reliability [53].

A typical DC microgrid structure is shown in Figure 2.2. The DC microgrid contains multiple sources, storages and loads with their associated power electronics interfaces. As shown in Figure 2.2, parallel PV arrays are connected to the DC bus via DC/DC converters. A wind generation is tied to grid through an AC/DC rectifier. Two battery units, serving as the storage elements, are connected to the bus through bidirectional

DC/DC converters, allowing the storages to be capable of charging or discharging. The loads can be directly tied to the grid or through load converters. Typical examples of DC powered household loads include the laptop, cell phone, cable modems, wireless internet router, etc.

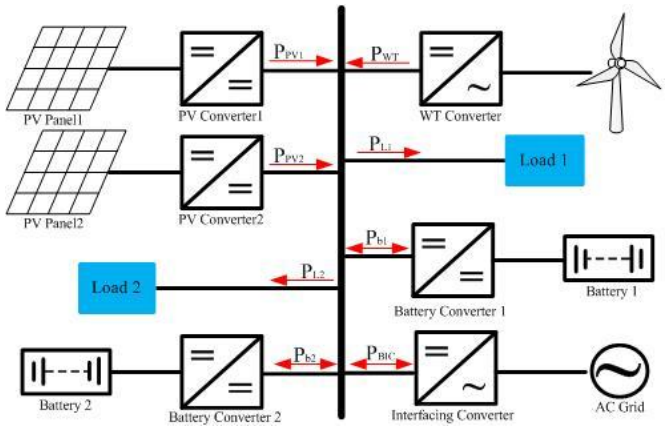

Figure 2.2. Basic DC microgrid structure.

2.4. Hybrid AC/DC Microgrids

2.4.1. Why hybrid AC/DC microgrids?

Although DC microgrids show various aforementioned advantages, having DC microgrids alone however might not be readily accepted now, since AC distribution is presently dominant and is expected to be so for the next few decades. Therefore, a more likely scenario will be a hybrid AC/DC microgrid which is the coexistence of both AC and DC microgrids with sources, storages and loads appropriately organized between them. The reasons of proposing the hybrid concept can be summarized in terms of gradual changes in load types and DGs as follows.

1) Load trend from AC to DC

The earliest power supply systems were established to supply the lighting, heating and motor driving loads. AC or DC loads and generators were formerly designed and installed to adapt the respective supply systems at the initial stage of an AC or DC system. AC systems haven't been spread to be the standard until AC won and became the dominant supply system. Since then, all loads are required to adopt AC supply

systems, whereas DC loads were connected to the AC system through AC/DC rectifiers without in-depth consideration of the efficiency of those additional conversion stages. The weaknesses of AC transmission have been completely overshadowed by the considerable advantages.

Table 2.1. Some typical loads in future power systems.

Loads	AC	DC	ACwC
UPS and energy storage		√	
Electrochemical processes		√	
Electronics loads		√	
Electric arc furnace	√	√	
Future motor driver	√	√	√
Heating	√	√	√
Railway	√	√	√
Future lighting		√	
Future air conditioner			√

With the development of power electronics interfaces and the associated control for higher efficient energy utilization and more flexible control implementation, an inconvenient truth that has occurred quietly in conventional AC power systems is the load trend from AC to DC type. It is not difficult to find the modern electrical power system that, DC loads and AC loads with AC converters (ACsC) are playing the dominant role in most AC power systems. This phenomenon is also mainly due to the consistent significant reduction of pure AC loads in conventional power systems. Most loads in households and commercial buildings, like computers, printers, DVD players and home theater system are DC by nature. On the other hand, the common AC loads driven by AC motors, such as washing machines, refrigerators, air conditioners, and industry equipment are being gradually replaced by AC motors with build-in DC/AC inverters to adjust the motor speed and save energy. Furthermore, the efficient AC fluorescent lamps, which have almost replaced the earliest incandescent bulbs, are now being gradually replaced by the more efficient light-emitting diodes (LEDs). Table 2.1 lists the primary loads in the future power systems. It can be seen from Table 2.1 that most of the future loads will be DC in nature. Therefore, efficient utilization of different types of loads might be achieved by emerging DC grid with DC load into existing AC infrastructure [14].

2) Increasing integration of renewable energy sources

Growing energy demand facilitates wide-spread applications of RESs, such as PV arrays, wind turbine generators (WTG), fuel cells, energy storage systems (ESSs) and electric vehicles (EVs). The increasing integration of renewable-based DGs into microgrids is another prominent event occurred in current AC power system.

For those RESs, PV arrays and fuel cells generally require DC/AC inverters for grid connections. Further complicated control circuit for the inverters is also needed for system synchronization and harmonic-free power production. ESSs essentially require charging/discharging interfaces for grid connections. The charging/discharging controllers are also the necessary element for EVs, allowing it freely to absorb power from the grid in charging stage or release stored power to the grid in discharging stage. The increasing penetration of DC-type RESs and evolution load trend from AC to DC make us conceiving that "is it possible to upgrade the current AC distributed system with DC microgrid?" The answer for this question might be hinted from the following analysis on multiple conversions and the additional efficiency losses in existing AC distribution systems.

3) Power conversions in AC and DC systems

Power conversions for different sources and loads in AC and DC systems are analyzed in this sub-section as below.

In an AC microgrid, DC sources like PV arrays and fuel cells need to be converted into AC through DC/AC inverters before grid connections. If this kind of DC power is eventually consumed by DC loads, further AC/DC rectifiers are needed. For ACwC loads, the power conversion flow is DC-AC-DC-AC, and a DC/AC inverter, an AC/DC rectifier, and a DC/AC inverter are required.

For the AC sources, no additional conversion is required if it is finally consumed by AC loads. For DC loads, the power conversion flow is AC-DC, and an AC/DC rectifier is required. For ACwC load, the conversion flow is AC-DC-AC, and both the AC/DC inverter and DC/AC rectifier are required.

In the DC microgrid, no additional conversion stage is required if the DC loads are

supplied by DC sources. If the DC sources are finally consumed by AC or ACwC loads, the conversion flow should be DC-AC, and a DC/AC rectifier is needed.

For the AC sources, additional DC/AC inverters are required if their power are finally consumed by AC loads, and the power conversion flow is AC-DC. For ac and ACwC loads, the conversion flow is AC-DC-AC, and both AC/DC rectifier and DC/AC inverter are required.

For illustrative purpose, the power conversion flow for different sources and loads in AC and DC microgrids are shown in Table 2.2.

Table 2.2. Power conversion flow for different sources and loads in AC and DC microgrids.

System	Source	DC load	AC load	ACwC load
AC	DC	DC-AC-DC	DC-AC	DC-AC-DC-AC
	AC	AC-DC	—	AC-DC-AC
DC	DC	—	DC-AC	DC-AC
	AC	AC-DC	AC-DC-AC	AC-DC-AC

2.4.2. An example of hybrid AC/DC microgrids structure

Figure 3.2 shows the structure of a hybrid AC/DC microgrid, which is constructed in the Water and Energy Research Lab (WERL) with support from Schneider Electric Singapore and Nanyang Technological University (NTU), Singapore. The hybrid system consists of a 400V, three-phase AC grid with 8 nodes and a 380V DC grid with 8 nodes. Both AC and DC grids can be configured into radial or ring configurations. Two bidirectional converters interconnect the two microgrids together. On AC side, it has an 18kW AC programmable source, 7.5kW WTG simulator, 4.5kW electrical load, and 3.3kW resistive load. On DC side, a 20kW DC programmable source, a 14.5kW electrical load, a 3.3kW resistive load, 1.45kW solar simulator, and 28.8kW battery storage are drawn. A 5kW physical PV arrays on the rooftop can be either connected to the grid through a DC/AC inverter or coupled to DC grid through a DC/DC boost converter. A 1.2kW fuel cell with a 5kWh hydrogen tank as the energy storage is connected to the AC grid and can be also tied to the DC grid. The main purpose of constructing this hybrid AC/DC microgrid is to build up a test bed for: (1)

investigating different hybrid infrastructures; (2) studying independent and coordination control for various converters; (3) testing suitable voltage levels for DC microgrid; (4) exploring new problems due to the connection of DC sources and loads; (5) developing new topology for efficient and reliable operation of hybrid microgrid; (6) exploring and testing new DC protection schemes; (7) developing energy management systems for the hybrid microgrid.

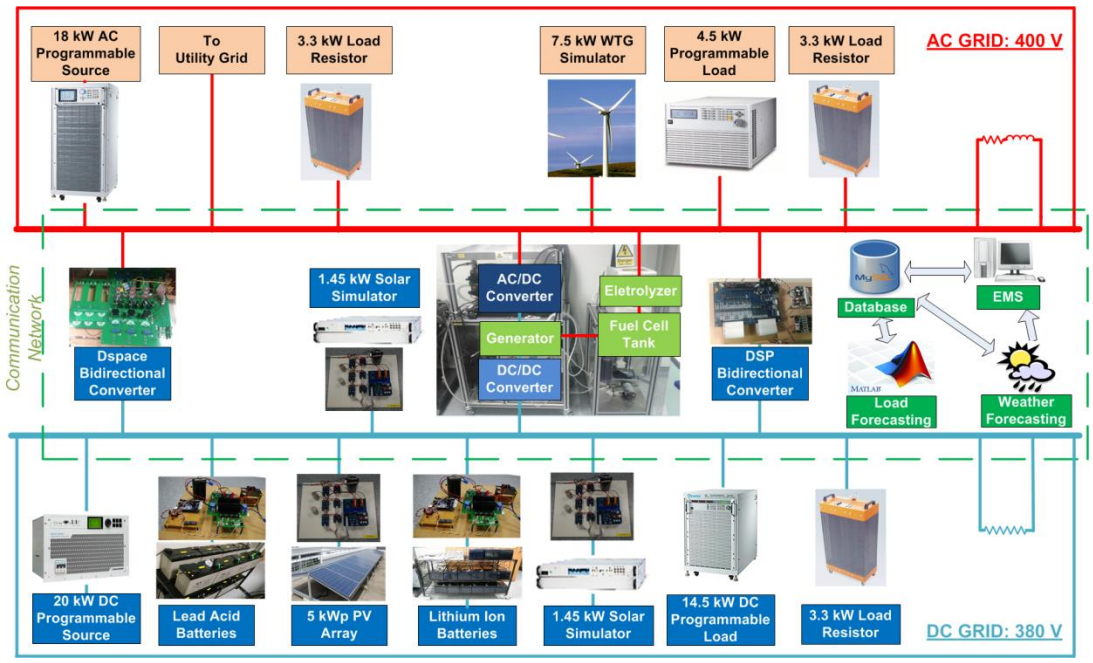

Figure 2.3. A hybrid AC/DC microgrid in the WERL, NTU.

2.4.3. Main advantages of hybrid AC/DC microgrids

As stated in the above analysis, multiple power conversions can be reduced with the proposed hybrid AC/DC structure. The advantages of the hybrid system can be summarized as follows:

a) The elimination of unnecessary multiple power conversion stages benefit a reduction of total conversion losses.

b) The elimination of front-end rectifiers for DC and ACwC loads in the present AC system can feature the simplification of electric equipment and cost reduction.

c) The original harmonic current in AC grid can be attenuated by sinking it to the DC grid through the interlinking converters, and control for harmonic compensation will be easier due to large connections of DC load in the DC microgrid.

d) Negative and zero sequence current, which are mainly caused by unbalanced loads

in AC system can be absorbed by the DC microgrid, and the neutral wire in sub-transmission may be eliminated with reduced transmission losses.

2.5. Conclusions

This chapter introduces the concept of hybrid AC/DC microgrid as well as its main advantages. After a brief review of DGs and microgrids, the feasibility of AC and DC microgrid are presented. The reason of proposing hybrid solution is then illustrated in Section 2.4. An example of the hybrid AC-DC microgrids structure is subsequently described in order to address the potential aims of a test-bed hybrid microgrid. Finally, the main advantages of proposed hybrid AC/DC microgrid have been summarized.

Chapter 3 Hierarchical Controlled DC Microgrid

3.1. Introduction and Literature Review

With increasing penetration of solar power in distribution systems and rapid load evolution from AC to DC, DC microgrids are becoming attractive because of their higher efficiency for integration of DC sources and loads [12, 33, 54]. The advantages of DC microgrids include better compatibility, higher efficiency and robust stability. Being featured with those advantages, the applications of DC microgrids have been broadened in industry systems, commercial buildings and residential complex. The paradigm shift from AC to DC system facilitates easier control of individual load performance, increased integration of renewable energy sources (RESs) and distributed energy storages.

In general, stable operation of a standalone DC microgrid with multiple DC sources, energy storages (ESs) and loads consistently relies on the flexible and reliable control strategies for attenuating intermittence from renewable sources and balancing power between the supply and demand ends. Moreover, maintaining DC bus voltage within the limits while maximally utilizing renewable energy and prolonging storage lifetime involve coordinative combination of power balancing control and high-layer energy management strategy.

Power balancing strategies for microgrid control can be generally classified as the centralized, decentralized and distributed [16]. For centralized control, system information is acquired by a central controller so as to schedule tasks, make control decisions and realize the global optimization [55, 56]. However, failures in communication links among converters may degrade system reliability. This constrain can be avoided by decentralized control in which power electronic converters operate based on local quantities measurements [57, 58]. Nevertheless, this improvement is at the cost of suffering limited system stability and losing optimal operation fashion because each converter is lack of the information and operation status of others [59].

Concerning the drawbacks of power balancing strategies in centralized and

decentralized manners, distributed control provide an alternative solution on optimizing resource utilization while retaining system reliability [60-62]. A typical distributed control strategy applied to DC microgrid is DC bus signaling (DBS), in which bus voltage is used as a communication carrier to determine the operation modes of converters according to the predefined voltage thresholds. By using DBS, the overall system redundancy can be maintained since each unit within the system only measures the DC bus voltage to schedule proper operation modes [16]. However, some extreme conditions such as over-current / voltage charging, fully charging / under discharging for storages are not considered. In fact, effective operations of sources and loads in respond to the extreme conditions for storages can be hardly achieved if the elements electrical quantities cannot be exchanged.

In [61], DBS is extended to control a grid-coupling DC microgrid where different bus voltage levels are predefined to distinguish different system operation modes and determine mode switching. Although both stand-alone and grid-connected operations can be scheduled by the voltage level signaling, this control strategy inherently suffers two major drawbacks. On the one hand, the number of sources and storages within the system is restricted by the number of voltage levels, which cannot be divided unlimitedly due to the DC bus voltage tolerance. One the other hand, adding sources with higher priority involves changing the states of all other sources with a lower priority, which restrains the realization of “plug and play”. For the above limitations, voltage level signaling can only be suitable for a small-scale microgrid with limited number of sources and storages [63].

Droop control has been proved to be an effective method to merge multiple sources and storages with a same priority so that they can operate in a same voltage band, proportionally sharing load according to their ratings. Unlike AC microgrids, where frequency is consolidated throughout the system, the voltage terminal of each unit in a DC microgrid is slightly different due to the voltage drop. This would lead to power sharing inaccuracy. To solve the problem of inaccurate power sharing, a distributed control strategy utilizing low band-width communication is proposed in [62]. Nevertheless, the utilization priority of renewable sources, non-renewable sources (NRS) and storages are not considered.

Considering the limitations of the aforementioned distributed control strategies, it is necessary to combine distributed control and high-layer supervision system together. With this intention, this chapter introduces a hierarchical control strategy for reliable and economical operations of standalone DC microgrids. The hierarchical control strategy includes three hierarchical levels. Hierarchical Level I (HLI) is the primary control to maintain bus voltage within specified limits through scheduling the operation modes of converters. The bus voltage in this level essentially acts as an indicator of supply-demand balance. A wireless control is employed for reliable operation of the grid. Hierarchical Level II (HLII) is the secondary control to achieve real-time voltage regulation capability for the system's power modules and prioritizations for charging/discharging of the batteries with different state of charges (SoCs). A reasonable compromise between maximum power harvesting and effective battery charging is addressed in this level using coordination control based on a central energy management system (EMS). Hierarchical Level III (HLIII) handles extreme operating conditions such as sudden load and source changes due to system failures through load shedding or ballast. The feasibility and effectiveness of the proposed hierarchical control strategy have been tested on a DC microgrid in the laboratory.

3.2. System Configuration

Figure 3.1 shows the configuration of the PV/battery based DC microgrid in this chapter, where multiple sources, storages and loads are drawn. Each PV module is comprised of a PV panel and a DC/DC boost converter, while each storage system contains a storage element and a bidirectional buck-boost converter. A DC source is connected to the bus via a DC/DC boost converter, serving as the non-renewable source (NRS).

Reliable and economical operation of a standalone DC microgrid depend on the coordination control of associated interfacing terminals of sources and storages as shown in Figure 3.1. Those terminals can be generally categorized into power and slack terminals. The power terminals, such as PV modules in maximum power point tracking (MPPT) mode, battery energy storage system (BESS) in charging/discharging modes and constant power load (CPL), can either supply or consume power. The slack terminals primarily maintain the bus voltage by accommodating the power imbalance

caused by the load and source variations. Typical examples of slack terminals are BESSs and PV modules in bus monitoring mode (BM), regulating the DC bus voltage.

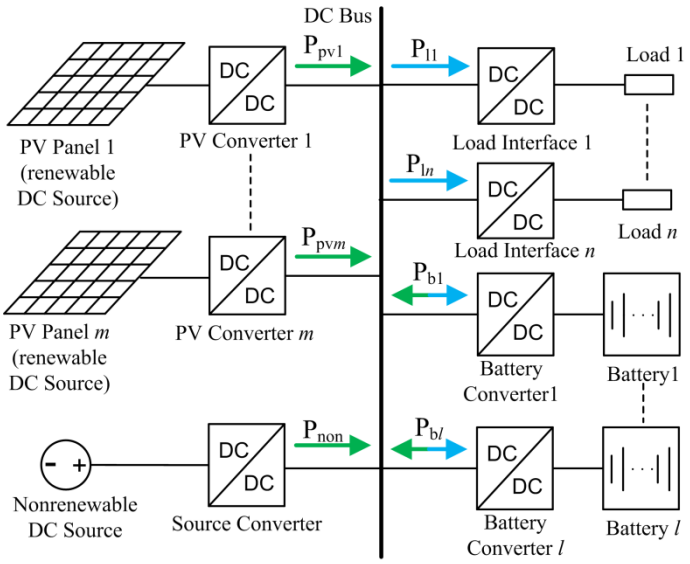

Figure 3.1. Configuration of DC microgrid.

3.3. Hierarchical Control

For stable grid operation, at least one slack terminal is required at any time to maintain the bus voltage within the limits by maintaining overall power balance. Neglecting power loss on DC network, the instantaneous power balance in the DC bus is expressed as

$$\sum_{i=1}^{m} P_{pvi}(t) + \sum_{j=1}^{n} P_{bj}(t) - \sum_{k=1}^{l} P_{lk}(t) = 0 \tag{3-1}$$

where m, n and l are the number of PV modules, BESSs and loads respectively; P_{pvi} (t) is the power generated by i^{th} PV module; P_{bj} (t) is the power injected into the bus from j^{th} BESS which is positive when BESS is discharged; P_{lk} (t) is the power consumed by the k^{th} load. Instantaneous power balance at the DC bus is a complicated multiple objective control problem including maximizing renewable energy harvest, optimizing usage of BESSs and maintaining bus voltage within its limits under loads and resources variations. Therefore, a three-level hierarchical control is proposed to achieve reliable and economical system operations in this section.

The proposed method is based on DC bus signaling (DBS) in which the bus voltage is divided into five regions using the four predefined voltage thresholds determined by specific operation requirements as shown in Figure 3.2. The voltage difference between neighboring thresholds should be carefully selected so that it's neither too small to avoid malfunction during modes switching due to measurement errors nor too big to avoid significant bus voltage variations which may affect normal operation of the load. The relationship among the threshold values is expressed as

$$V_{L2} < V_{L1} < V_{dcn} < V_{H1} < V_{H2} \tag{3-2}$$

where V_{dcn} is the nominal DC bus voltage; V_{L2} and V_{H2} are the boundaries of allowable bus voltage band; V_{H1} and V_{L1} are the threshold values activating the battery charging and discharging respectively.

It should be noted that the threshold values vary with the nominal voltage and operating requirements of a particular system. So far, the standardization of DC grid requirements such as the optimal voltage level and the tolerance band of bus voltage have not been commonly established in spite of its well-recognized operations with higher efficiency, better compatibility. Different DC voltage tolerances are defined in [16, 61] for low and medium voltage DC microgrids, respectively. Considering that most of the DC loads are CPL, which employ front-end load converters to establish required operating voltage regardless of the variations in the input voltage. From a control point of view, the variations in DC bus voltage can be viewed as an input voltage disturbance for the entire frond-end converters of CPLs. Therefore, voltage variations in a pecified range can be acceptable for most of the DC loads. According to the above references, the voltage threshold values in this research work are predefined in Table 3.1, where V_{dcn} is set at 300V, V_{H1} and V_{H2} are configured at 5% and 10% above V_{dcn}, respectively, while V_{L1} and V_{L2} are 5% and 10% below V_{dcn}, respectively.

Table 3.1. Voltage thresholds for hierarchical controlled DC microgrids.

V_{L2}	V_{L1}	V_{dcn}	V_{H1}	V_{H2}
270V	285V	300V	315V	330V

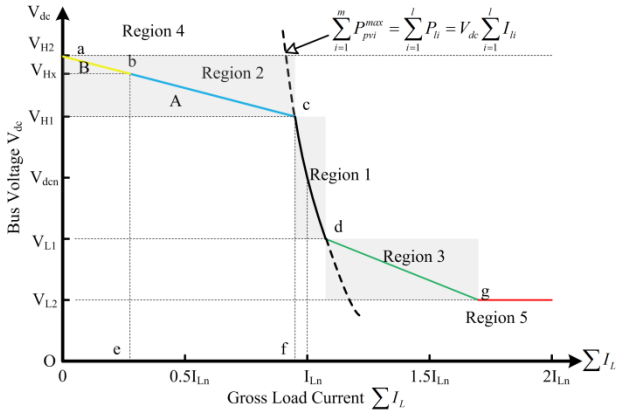

Figure 3.2. I-V characteristic of DC bus voltage under HLI control.

3.3.1. Hierarchical level I (HLI) control

The main objective of HLI control is to harvest the maximum power from RESs and maitain reliability of basic operations when communication network for information sharing among converters fails. Detailed control schemes for different operation regions are described as follows.

1) Region 1: $V_{L1} \leq V_{dc} \leq V_{H1}$

To avoid frequent battery charging/discharging micro-cycles due to minor change of loads or power generation, Region 1 is set as the operation zone in which all BESSs are in idle mode. In this region, PV converters operate in MPPT mode to extract maximum renewable energy, continuously supplying loads. The bus voltage within this region indicates that the power between sources and loads is balanced as shown in equation (3.3). Due to the lack of slack terminal, bus voltage is allowed to change within Region 1 according to power variation in the loads and sources.

$$\sum_{i=1}^{m} P_{pvi}(t) = \sum_{j=1}^{l} P_{lj}(t) \tag{3-3}$$

2) Region 2: $V_{H1} < V_{dc} \leq V_{H2}$

When PV modules generate more power than the required demand during high solar penetration periods, the bus voltage falls into Region 2 and the BESSs are activated to store the surplus power. Power sharing among BESSs is implemented by droop control as shown in Figure 3.3. To equally distribute the voltage regulation capacity of BESSs within Region 2, a linear droop is adopted as

$$V_{bj}^{ref} = \begin{cases} V_{H1} - m_{bj} I_{bj}^{o}, & I_{bj}^{o} < 0 \\ V_{L1} - m_{bj} I_{bj}^{o}, & I_{bj}^{o} > 0 \end{cases} \tag{3-4}$$

where V_{bj}^{ref} , I_{bj}^{o} and m_{bj} are the reference voltage, bus side current and droop coefficient of j^{th} BESS, respectively. Equation (3.4) is the charging and discharging droop expressions for $I_{bj}^{o} < 0$ and $I_{bj}^{o} > 0$, respectively.

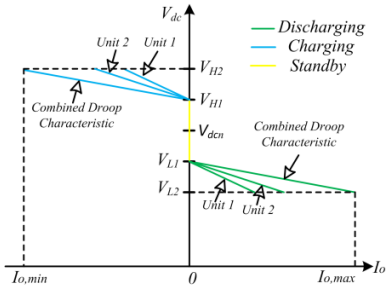

Figure 3.3. Batteries droop characteristic.

Combined with BESS droop characteristics, the system droop characteristic in Region 2 is shown as trajectory *c*-*b* in Figure 3.2. The charging current of the batteries in this region may exceed their maximum allowable values. To prevent batteries from over-current charging while extracting maximum renewable power, the PV converters need to be switched from MPPT to BM mode in case the last BESS reaches its maximum charging current at the point V_{Hx}. Region 2 is therefore divided into two sub-regions by V_{Hx}. Small resolution of each sub-region will increase the difficulty in regulating the bus voltage. Therefore, V_{Hx} is proportionally selected to avoid small resolution of bus voltage regulation in both sub-regions according to the maximum battery charging capacity and PV maximum power as

$$\frac{V_{Hx} - V_{H1}}{V_{H2} - V_{H1}} = \frac{\sum_{j=1}^{n} P_{bj}^{\max}}{\sum_{i=1}^{m} P_{pvi}^{\max}} \tag{3-5}$$

where $P_{bj}^{\max}$ and $P_{pvi}^{\max}$ are maximum power of j^{th} BESS and i^{th} PV system, respectively.

In Sub-region A ($V_{H1} < V_{dc} \leq V_{Hx}$), battery converters regulate bus voltage using droop control, allowing BESS modules to share the entire surplus power in proportion to

their capacities. Droop coefficients can therefore be designed as

$$m_{bj} = \frac{V_{Hx} - V_{H1}}{I_{bj}^{max}} \tag{3-6}$$

where I_{bj}^{max} is maximum charging current of j^{th} BESS converter. BESSs voltage regulation capacity is the summation of individual ES capacity. The equivalent combined droop characteristic is shown by trajectory *c*-*b* in Figure 3.2.

In Sub-region B ($V_{Hx}<V_{dc}\leq V_{H2}$), all BESSs operate in maximum power charging mode and PV converters regulate the bus voltage with droop control following trajectory *b*-*a* shown in Figure 3.2. The droop curve of each PV converter starts from V_{Hx} and ends at V_{H2}. The relative droop characteristics of PV converter is expressed as

$$V_{pvi}^{ref} = V_{Hx} - m_{pvi} I_{pvi}^{o} \tag{3-7}$$

where V_{pvi}^{ref}, I_{pvi}^{o} and m_{pvi} are the reference voltage, bus-side current and droop coefficient of the i^{th} PV module, respectively.

Charging capability of a BESS varies with its SoC. Proper charging scheme is recommended for charging batteries with fast rate and high safety. The commonly used charging approaches include constant-current and constant voltage charging (CC-CV) [64], intermittent charging [65] and interrupted charge control (ICC) [66]. The effectiveness of those charging techniques for standalone PV systems are investigated and compared in [67]. Among those methods, the CC-CV method have been proven to have a fast charging rate and able to keep the eventual SoC of battery as high as 100% in both no load and variable load profile conditions compared with intermittent charging and ICC.

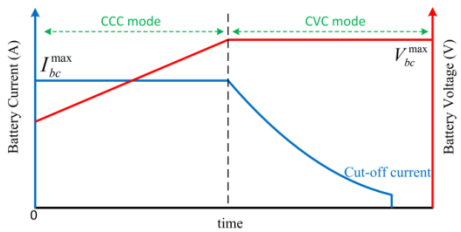

Figure 3.4. BESS charging scheme.

The detailed implementation of CC-CV charging is shown in Figure 3.4. The constant-current charging (CCC) with $I_{bc}^{\max}$ being the reference charging current is chosen at low SoC (typically below 70% - 80%), while for battery with high SoC, constant-voltage charging (CVC) is used where $V_{bc}^{\max}$ is set as the reference battery voltage. Transition time from CCC to CVC is generally determined by the terminal voltage of the battery. The BESS with terminal voltage higher than their respective $V_{bc}^{\max}$ will not be allowed to participate in regulating the DC bus voltage in Sub-region A to avoid gasification and overheating caused by excessive charging current at the end of the charging process. Instead, it will be charged in CVC mode, acting as a power terminal in the whole Region 2.

3) Region 3: $V_{L2} \leq V_{dc} < V_{L1}$

Low bus voltage is the indicator for deficiency in generated power. In this region, PV converters operate in MPPT mode and BESSs are in BM mode through discharging to compensate for the power shortage. By combining the BESS discharging droop characteristics as expressed in (3-4) with the overall load profile, the system droop curve in Region 3 is shown as trajectory *d-g* in Figure 3.2. BESSs reach the maximum discharge rate at point *g* in Figure 3.2 at V_{L2}. To prevent the bus voltage from collapsing, NRS comes online, maintaining the bus voltage at V_{L2}. The capacity of PV panels and batteries should be designed carefully so that they can fulfill the normal operation requirement of the loads most of the time and NRS will only be occasionally activated for unpredicted peak demand.

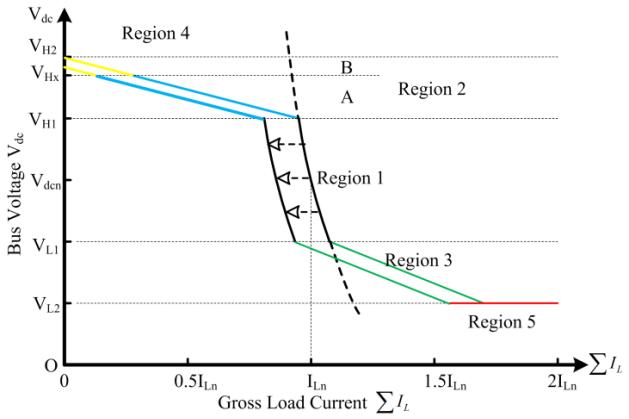

(a)

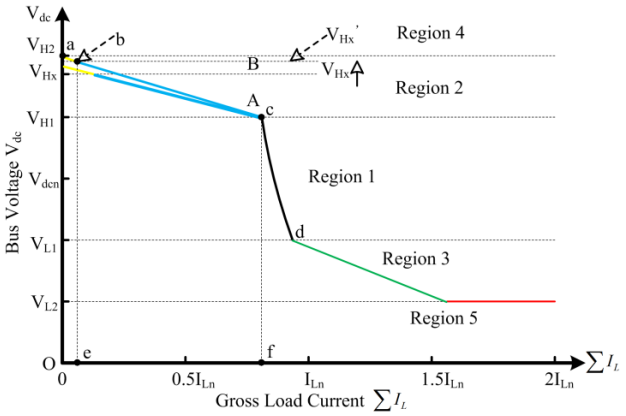

(b)

Figure 3.5. Illustration of impact of PV generations reduction on DC bus characteristics: (a). the drawback of HLI control; (b). the improvement in HLII control.

Due to the lack of communication link in HLI, optimal operation fashion can hardly be achieved. Firstly, the system I-V curve should be determined by the real-time BESS charging/discharging capabilities and PV maximum power outputs. Determination of droop coefficients is not optimal solution. For example, in case of reduced power generation from PV modules as shown in Figure 3.5(a), I-V curve will shift leftwards and the total PV droop curve will intersect with the voltage axis below V_{H2}. The extreme case is when both voltage regulation zones for PV modules and BESSs are reduced if PV generations reduced below battery charging capability. This results in degradation of power sharing accuracy among multiple PV modules or BESSs.

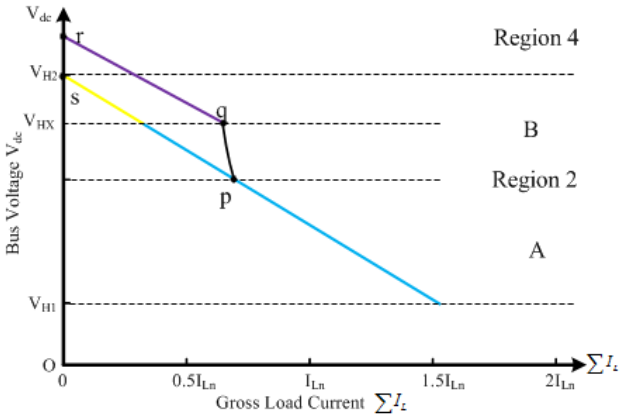

(a)

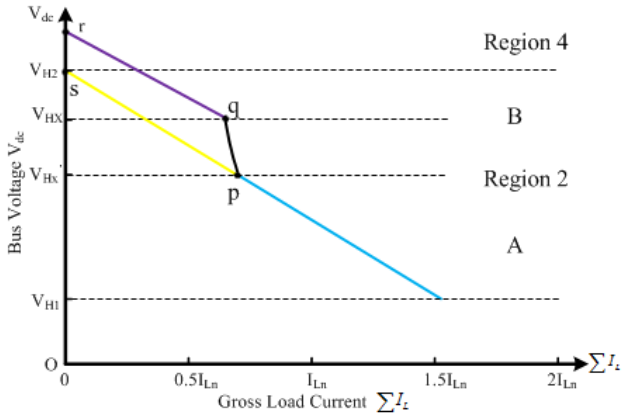

(b)

Figure 3.6. Impact of BESS charging capability reduction: (a). the drawback of HLI control; (b). the improvement in HLII control.

Secondly, the charging capability of BESS varies with SoC and terminal voltage. The entire charging capability of BESSs in Sub-region A may be reduced due to several factors. For instance, some of BESSs with relatively high SoC cannot regulate the bus voltage according to the predetermined droop equation since the voltage for triggering CVC is reached. The BESSs in this situation are operating in CVC mode and storing lower power with respect to the expected stored power in BM mode. Furthermore, the droop coefficient in Sub-region A is calculated based on the maximum BESSs charging capacity, which however, might be reduced with the BESS terminal voltage reduction. In case of charging capacity reduction, the system droop curve in Sub-region A will end at point *p* as shown in Figure 3.6 (a) where all BESS elements reach their maximum charging capacity. The system droop curve then lies along trajectory *p*-*q*. PV modules are activated to operate in BM mode at *q*. In this case, the system droop curve in Sub-region B will start at *q* with the predefined droop coefficient. This may lead bus voltage to exceed the maximum value V_{H2} if the entire load becomes quite light as explicated by trajectory *q*-*r* in Figure 3.6 (b).

Thirdly, to prolong the batteries lifetime, it is profitable to prioritize batteries with different SoCs. Batteries with lower SoC should be scheduled to charge first or fast in the charging stage to prevent sulphation in extreme low SoC, and vice versa. This process requires information exchange and coordination control among BESS converters. The above problems, inherently existing in HLI control, can be compensated by HLII control as follows.

3.3.2. Hierarchical level II (HLII) control

The aforementioned limitations in HLI control can be improved through real-time information exchange among converters in HLII control. Communication link generally brings full observability over DC grid including real-time bus voltage, power flow and operation status of converters. System optimal operation in terms of reliability and cost can therefore be achieved through coordination control of system elements. Although the effectiveness of the system operation depends heavily on the communication quality in HLII, the system reliability would not be degraded due to HLI as back up. Once failure happens in the communication links, all elements including PV modules and battery storages can retain the system reliability under HLI control at the cost of losing global optimal fashion.

The control strategy for Region 1 in HLII is the same as the one in HLI. The PV modules operate in MPPT mode and BESSs are idled. The main objective of HLII control is to solve the power sharing problems among PV modules and BESSs considering their instant capacities variations.

1) Charging/Discharging Control in Regions 2 and 3

Since BESSs need to regulate bus voltage through charging/discharging in Regions 2 and 3, the coordination control among BESSs modules is required. Different charging/discharging control schemes can be implemented based on special requirements of BESSs. In this chapter, the control objective is to balance SoCs of different BESSs through proportional charging/discharging. This objective is achieved by tuning charging/discharging droop coefficients based on real-time SoCs measurements and exchanging. An index ξ_j, which is the ratio of SoC_j of j^{th} BESS to the average SoC of all BESSs batteries is defined as

$$\xi_j = \frac{SoC_j}{\frac{1}{n}\sum_{j=1}^{n} SoC_j} \tag{3-8}$$

where n is the number of BESSs. Largerξ_j means the BESS with higher SoC. The ξ_j is used to adjust the droop coefficient of j^{th} BESS converter as

$$m_{bj}^{'} = \begin{cases} \xi_j m_{bj}, & i_{bj} < 0 \\ m_{bj} / \xi_j, & i_{bj} > 0 \end{cases} \tag{3-9}$$

where m_{bj} is the droop coefficient of j^{th} BESS converter in HLI control as expressed in (3.6), $m_{bj}^{'}$ is the modified droop coefficient of j^{th} BESS converter. The effect of modified droop coefficient on charging/discharging rate is illustrated in Table 3.2.

Table 3.2. Illustration of SoC-based droop coefficient.

	$i_{bj} < 0$ (charging)	$i_{bj} > 0$ (discharging)
$\xi_j < 1$	$m_{bj}^{'} < m_{bj}$	$m_{bj}^{'} > m_{bj}$
$\xi_j > 1$	$m_{bj}^{'} > m_{bj}$	$m_{bj}^{'} < m_{bj}$

During charging stage ($i_{bj} < 0$), the BESS whose SoC is higher than the average SoC of all BESSs ($\xi_j > 1$), is expected to have a lower charging rate. Therefore positive droop coefficient should be increased from the original ($m_{bj}^{'} > m_{bj}$). This is guaranteed by equation (3-9) because of $\xi_j > 1$. Otherwise, a smaller droop coefficient ($m_{bj}^{'} < m_{bj}$) is required for the BESSs with lower SoC. Conversely, during discharging stage ($i_{bj} > 0$), a smaller droop coefficient ($m_{bj}^{'} < m_{bj}$) promises larger discharging power for those BESSs with the SoC above the system average SoC ($\xi_j > 1$), whereas a relative larger droop coefficient ($m_{bj}^{'} > m_{bj}$) promises relative small discharging power for the BESS with the SoC below the system average SoC ($\xi_j < 1$).

2) Balancing Voltage Regulation Zones for BESSs and PV Modules

To overcome the problems in HLI control in Region 2, the voltage regulation zones of BESS and PV converters are assigned proportionally to their instant capacities. As mentioned in Figure. 3.5(a), the voltage regulation zone of PV converters will be limited in Sub-region B due to the reduced generation in PV modules. Under HLII control, the combined system droop is expected to start from V_{H1} and end at V_{H2} as demonstrated in Figure 3.2 regardless of the variations in PV generations to fully

utilize the voltage regulation zone. Therefore, the power sharing accuracy can be enhanced. This can be realized by shifting the threshold value V_{Hx} upward to V_{Hx}' as shown in Figure 3.5(b). V_{Hx}' is determined by interpolation of the DC bus voltage proportionally to real-time PV maximum power and battery charging capacity. The ending point in Sub-region B then moves to point *b*, also meeting the criterion (3.5), whilst the voltage regulation zone of PV converters can thus occupy the band completely between V_{Hx}' and V_{H2} as shown by trajectory *a-b* in Figure 3.5(b).

The shortcoming of HLI as demonstrated in Figure 3.6(a) can be overcome as well by HLII control as shown in Figure 3.6(b). This prevents the system droop curve from the tendency to lie on the trajectories *p-q* and *q-r*, which may exceed the maximum boundary of DC bus voltage. Instead, the system droop curve will move along trajectory *p-s*.

3.3.3. Hierarchical level III (HLIII) control

Over- or under-voltage occurs due to sudden loss of loads or PV modules during normal system operation. This will damage the system elements and cause malfunction in control system. To prevent abnormal system operation, HLIII control is designed to maintain the bus voltage within an allowable band once abnormal system conditions occur.

1) Region 4: $Vdc>V_{H2}$

When the bus voltage reaches V_{H2}, the ballast is activated to absorb the power and maintain the voltage within V_{H2}.

2) Region 5: $V_{dc}<V_{L2}$

Voltage drop is caused by power deficiency. If all available sources including the NRS cannot supply the total load, bus voltage will dip below V_{L2}. In this case, a load shedding scheme is employed to cut part of the non-critical load in order to maintain the bus voltage within limit. Loads can be prioritized according to their importance and can be shut down sequentially during load shedding. Prioritization could be realized through EMS.

In summary, reliable and economical operation of a DC microgrid is guaranteed by the proposed hierarchical control scheme. During the normal operation, the DC microgrid operates under HLII control, where maximum energy from PV modules is harvested and the BESSs are coordinately utilized according to their instant SoCs and capacities. Once a failure occurs in the communication links, the grid is automatically transferred into HLI control, where each power module will operate based on the thresholds to maintain basic operations. The emergency conditions are managed by the HLIII control.

3.4. Modeling of System Elements

3.4.1. Modeling of PV arrays

The PV arrays, which convert light into electricity, can be represented as a single diode model as shown in Figure 3.7(a).

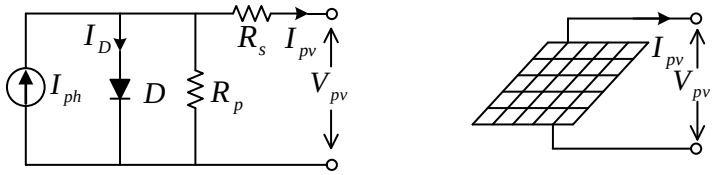

(a) (b)

Figure 3.7. PV modeling: (a). equivalent circuit of a solar cell, (b). symbol of PV arrays.

The relationship between the output current and voltage for n_s series and n_p parallel connected PV arrays can be expressed as the following three equations [68]:

$$I_{pv} = n_p I_{ph} - n_p I_{sat}[\exp((q/AkT)(V_{pv}/n_s + IR_s)) - 1] \quad (3\text{-}10)$$

$$I_{ph} = (I_{sso} + k_i(T - T_r)) \cdot S/1000 \quad (3\text{-}11)$$

$$I_{sat} = I_{rr}(T/T_r)^3 \times \exp((qE_{gap}/kA) \cdot (1/T_r - 1/T)) \quad (3\text{-}12)$$

where I_{pv} and V_{pv} are the output current and voltage of the PV arrays, respectively, n_s and n_p are the number of cells connected in series and parallel, respectively. S is the solar irradiation level and T is the temperature of cells.

Based on the solar cell model, I-V and P-V characteristics of PV arrays under a

specific solar irradiation level and temperature are obtained as shown in Figure 3.8. The output current and voltage of PV arrays at certain load condition vary with solar irradiation and temperature.

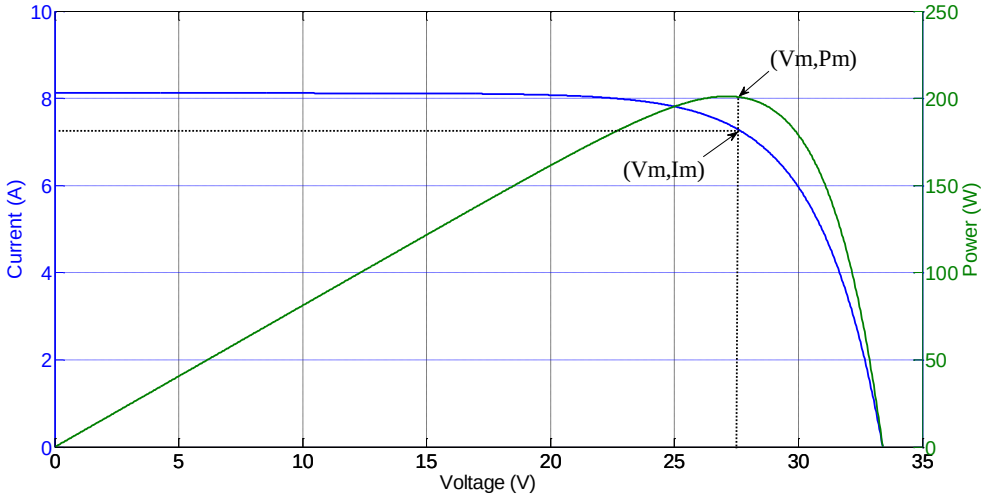

Figure 3.8. I-V and P-V characteristics of PV arrays.

3.4.2. Modeling of batteries

The battery model is modeled as a controlled voltage source in series with a constant resistance as shown in Figure 3.9. Its output voltage depends not only on the current but also on the battery SoC, which is a nonlinear function of the current and time as expressed as follows [69]:

$$V_b = E_o - R_b \cdot i_b - K\frac{Q}{Q - \int i_b dt} + A \cdot \exp(-B\int i_b dt) \tag{3-13}$$

$$SOC = 100(1 - \frac{\int i_b dt}{Q}) \tag{3-14}$$

where, R_b is the internal resistance of the battery, E_0 is the open circuit potential, i_b is the charging/discharging current of battery, K is the polarization voltage, Q is the battery capacity, A is the exponential voltage, and B is the exponential capacity.

3.4.3. Modeling of non-renewable source (NRS)

An ideal DC source as shown in Figure 3.10 is used to represent NRS, serving as the

back-up power supply with the lowest priority in supplying loads.

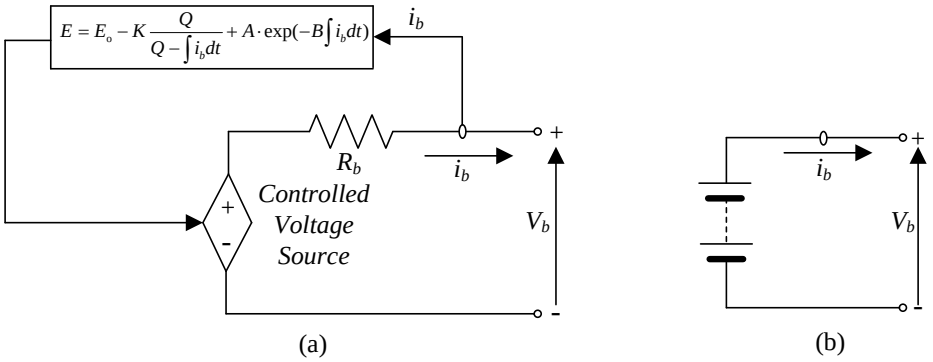

Figure 3.9. (a). Non-Linear battery model, (b). symbol of battery tanks.

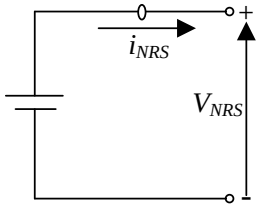

Figure 3.10. Symbol of NRS.

3.5. Control Structures of Source/Storage Converters

To implement the proposed hierarchical control scheme, each source/storage converter is controlled to perform in different modes of operation. The mode selection is determined by the mode selection signal which is determined by the hierarchical control strategy. In HLI control, each power module only senses the local bus voltage to determine the relevant operation mode. Once HLII control is enabled, each unit will acquire the information of the other units in the central control system to adjust itself to operate in the optimal fashion. If over- or under- voltage occurs, the HLIII control will have higher priority to schedule each source, storage and load converter operating in a reasonable mode. The mode switching signals M_{pv}, M_b and M_{NRS} for PV, BESS and NRS are shown in Table 3.3, which are determined by system operation conditions.

To maintain power balance in the DC bus and reliable operation, each PV or battery converter is well-scheduled by the proposed hierarchical control strategy, operating with different control structures coordinately. To illustrate each level of hierarchical

control clearly, different control structures, which are employed for proper control of PV/storage converters at different modes, are described in detail below.

Table 3.3. Mode Selection for PV, BESS and NRS Converters.

	1	2	3	4
M_{PV}	MPPT	Idle	BM	—
M_b	BM	Idle	CCC	CVC
M_{NRS}	BM	Idle	—	—

3.5.1. Control of modular PV DC/DC converters

The PV converter is a DC/DC booster as shown in Figure 3.15 and it can operate in MPPT, BM or idle mode according to the hierarchical control scheme elaborated above. The control structure of MPPT and BM are described in the following sub-section.

1) MPPT control (M_{PV} = 1)

As described in Section 3.4.1, the output current and voltage of PV arrays vary with the environmental and loading conditions. In a specific environmental condition, the PV arrays have a sole maximum power point (MPP) which satisfies:

$$\frac{dP_{PV}}{dV_{PV}}\Big|_{I_{PV}=I_m, V_{PV}=V_m} = 0 \tag{3-15}$$

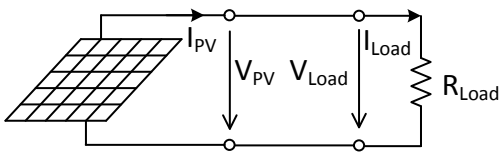

Figure 3.11. Equivalent circuit of the operation of PV arrays.

The MPP in a specific environmental condition is therefore solely dependent on the loading condition. Figure 3.11 is the equivalent circuit of the operation of PV arrays. The relevant I-V characteristics of both PV and loads are drawn in Figure 3.12. The intersection point of two I-V curves is the system operation point. Note that the PV

arrays will not operate in MPP if the corresponding loading condition is mismatched. To extract the maximum available power from PV arrays, the load of the PV system must be adjusted accordingly so that the load I-V curve intersects the PV I-V curve at the MPP. To achieve this feature, power electronic interfaces are employed to interconnect PV arrays and loads as shown in Figure 3.13 where a DC/DC converter is programmed to regulate the loading condition based on various MPPT algorithms.

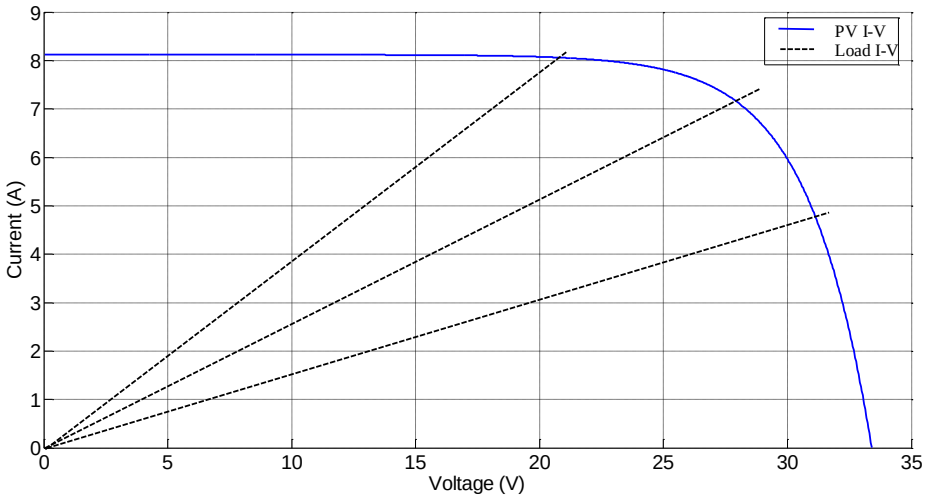

Figure 3.12. Illustration of different operation points for PV arrays.

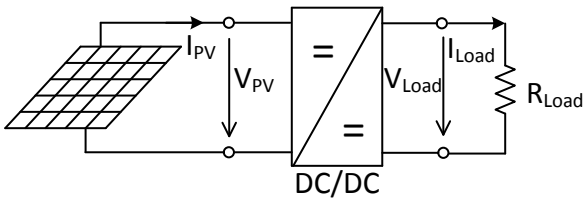

Figure 3.13. Common PV system with the feature of MPPT.

To realize maximum utilization of solar energy, MPPT techniques are critical for obtaining maximum power from PV arrays under any given environmental condition. Basic MPPT algorithms such as constant voltage (CV), perturb and observe (P&O), incremental conductance (INC) have been widely used in various PV applications [70], while advanced MPPT variants have been investigated and proposed in many publications [71-73]. Since the emphasis of this research work is the development of a coordination control among power modules in the system level, development of new MPPT algorithms for individual power converter will not be considered. Among the mature MPPT techniques, The CV method offers stable performance but suffers from

inaccurate maximum power tracking under different environmental conditions. The INC method offers good performance under rapidly changing environmental conditions. However, four sensors are required to implement the algorithm. Moreover, the duration of MPPT process depends on the sensors conversion time. During tracking time, the PV output is less than its maximum power, which indicates that longer conversion time will cause larger amount of power loss. The execution speed of P&O method is relatively higher as only two sensors are required. It gives the benefit of the reduction of hardware implementation and cost. The P&O method is adopted due to the advantage of simple arithmetic and easy implementation. For the P&O algorithm, the perturbation objective can either be PV voltage or current, however, this would be accompanied with complex implementation. To reduce the complexity, the duty ratio of interface converter is usually directly perturbed.

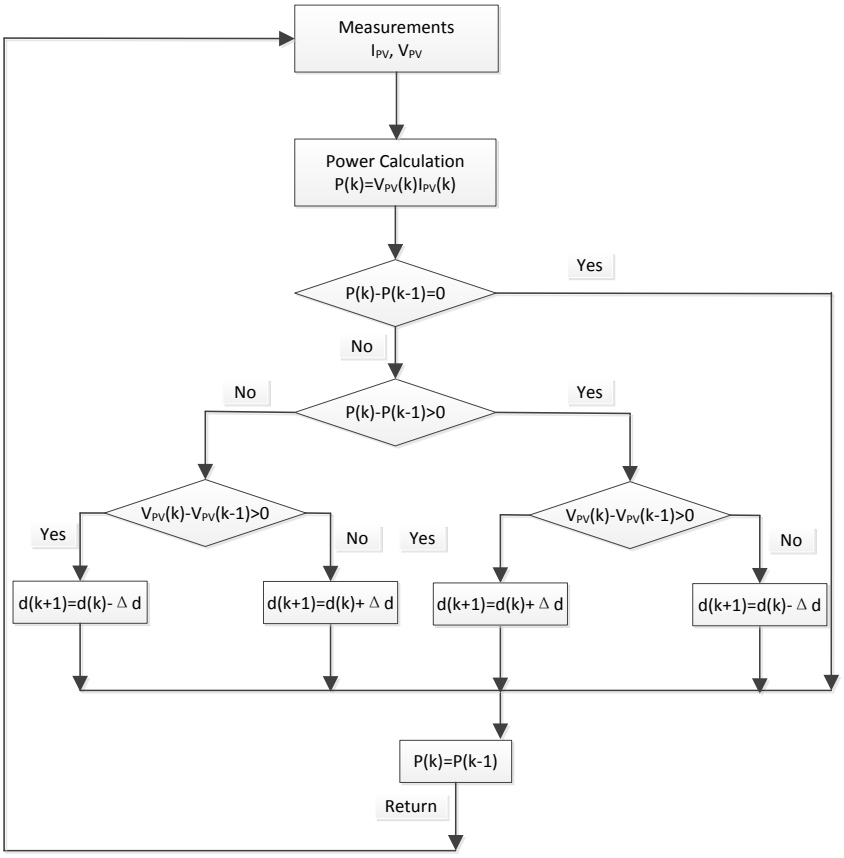

Figure 3.14. Flowchart of P & O algorithm.

The principle of P&O algorithm is first reviewed as: 1). when the duty ratio is increased by a perturbation step, if the output power of PV array increases, the duty ration should be increased further. Otherwise, the duty ratio should be decreased; 2)

when the duty ratio is decreased by a perturbation step, if the output power of PV array increases, the duty ration should be decreased further. Otherwise, the duty ratio should be increased. Based on the above description, the P&O algorithm can be expressed as

$$d_{k+1} = d_k + |\Delta d_k| \, sign\left[(\Delta d_k)(P_k - P_{k-1})\right] \tag{3-16}$$

where $\Delta d_k = d_k - d_{k-1}$ is the step size for the perturbing duty ratio; $P_k = V_{PV}(k) I_{PV}(k)$ is the PV output power at k^{th} interval. The relevant flowchart of the P&O algorithm is illustrated in Figure 3.14.

2) BM control (M_{PV} = 3)

The objective of BM control of PV modules is to regulate the DC bus voltage by maintaining the power balance in the overall system and to ensure proportional power outputs from PV modules.

The droop control method in BM mode is employed for proportional power outputs among multiple PV modules as expressed in (3-7). The I-V droop control generally senses the output current of PV converter and calculates the voltage reference which is fed into the inner current-regulated and outer voltage-controlled loops to generate the required duty ratio d_{BM}. For controller implementation, the proportional-integral (PI) controller is used for both current and voltage regulators as shown in Figure 3.15.

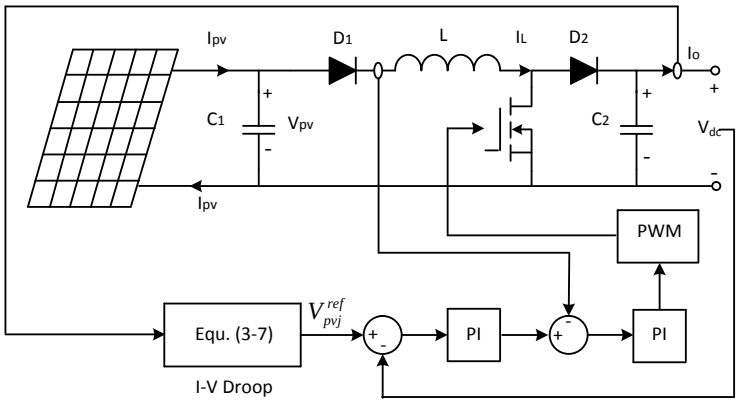

Figure 3.15. BM control for PV modules.

The control structure of MPPT and BM modes for PV modules have been described

above. The PV modules can also operate in idle mode in the case of serious shaded condition or maintenance duration. The combine the control structures and their associated mode selection signals as well as the overall control diagram of PV modules are drawn in Figure 3.16.

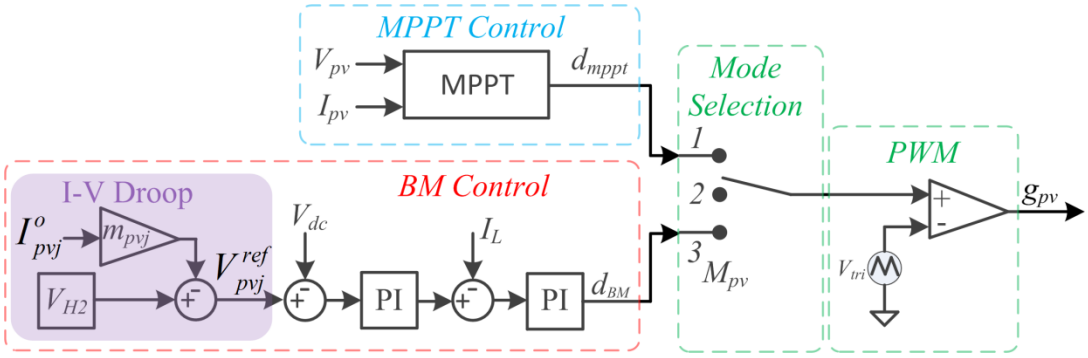

Figure 3.16. Mode selection and control diagram of PV modules.

3.5.2. Control of bidirectional DC/DC battery converters

The interface of the battery is a bidirectional buck/boost converter as shown in Figure 3. 17. The battery is connected to the universal half-bridge through an inductor L in the low voltage terminal. A filter capacitance C_O in the high voltage terminal is connected to the DC bus via the electrical cable. The bidirectional buck/boost converter contains an individual buck and a boost converter, allowing the battery to freely discharge or charge according to the specific control structure.

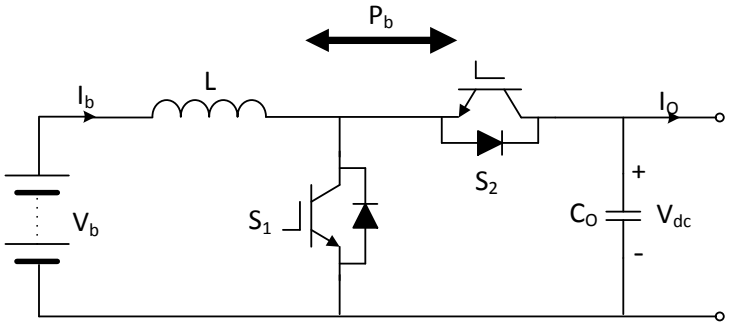

Figure 3.17. Bidirectional DC/DC battery converter.

The operating principle of the battery converter is demonstrated in Figure 3.18. During discharging, the buck/boost converter operates in booster mode, managing the battery to release power to the DC grid. The power flow thereby is from the battery to the grid. During charging, the buck/boost converter operates in buck mode, allowing the battery

to store power from the high voltage terminal. The power flow in this scenario is from the grid to the battery.

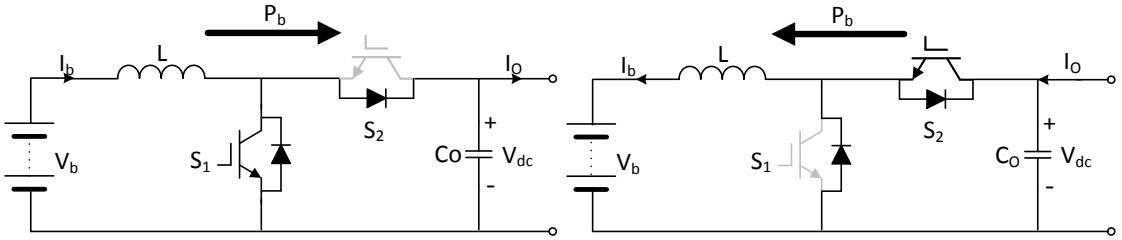

(a) (b)

Figure 3.18. Battery converter in charge/discharge state: (a). boost converter in discharge state; (b). buck converter in charge state.

The independent and complementary modulation schemes for the power switches in a universal half-bridge are usually adopted. For the independent modulation scheme, the workless power switch is consistently off while the other one operate in an on/off state to conduct the charging/discharging process. For the complementary modulation scheme, the state of the workless switch is consistently in the inverted state of the operating one. The latter is selected in this research work because of its easy implementation using a modular PWM generator.

With proper control schemes, the battery converter can operate in BM, CCC, CVC and idle modes. Details of each control mode are elaborated below.

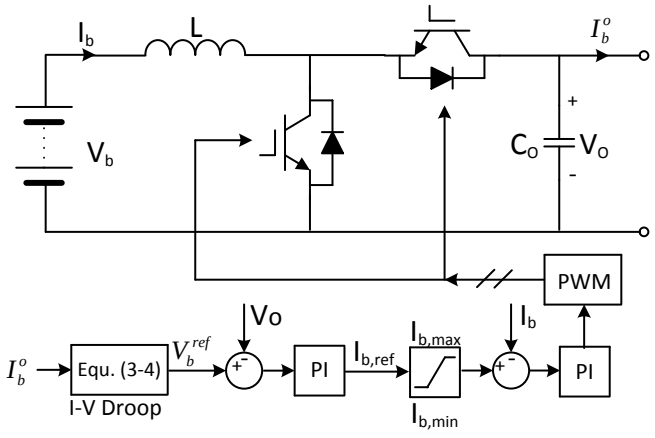

Figure 3.19. BM control for BESS.

1) BM control

The control objective of BM control for BESS is to regulate the DC bus voltage through maintaining power balance in the overall system and proportionally absorb/release the surplus/stored power from/to the DC grid. The control block diagram of BM control is drawn in Figure 3.19. It comprises of a fast inner PI current controller and a slower outer PI voltage controller. The outer PI controller regulates the output voltage of the converter through tracking the reference voltage, which is determined by the V-I droop equation expressed in (3-4). The duty ratio d_{BM} is subsequently obtained. The current upper and lower limits (I_b^{max} , I_b^{min}) are also included in current control loop to avoid over-current charge/discharge.

2) CCC and CVC during charging stage

In CCC mode, the control objective is to maintain the maximum charging current. The required duty ratio d_{CCC} for operation is generated by a PI current regulator as shown in Figure 3.20(a). In CVC mode, the control structure as shown in Figure 3.20(b) is the same as the voltage controller in BM mode except that the control variable is the terminal voltage of battery rather than the bus voltage in BM mode. The required duty ratio d_{CVC} for the battery converter in CVC is similarly generated. The BESS can also operate in idle mode in Region 1 or in case of over-current charging or under-voltage discharging. The control diagram of the multi-mode battery converter can be drawn with the mode selection signals as shown in Figure 3.21.

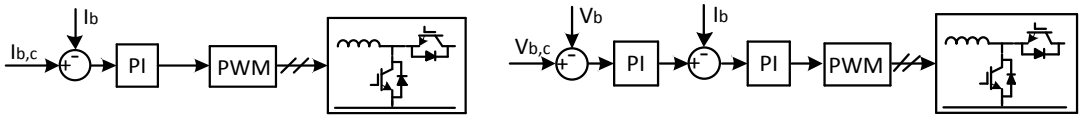

(a) (b)

Figure 3.20. Block diagram of CC and CV controls during BESS charging stage.

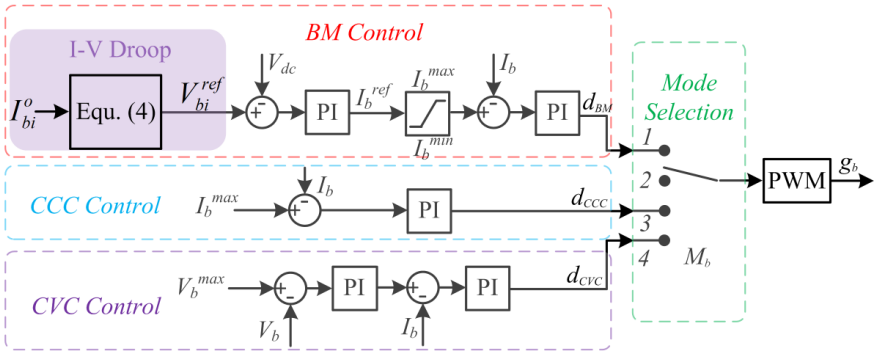

Figure 3.21. Mode selection and control diagram of BESS units.

3.5.3. Control of non-renewable source (NRS) converters

The NRS is interfaced to the DC bus through a DC/DC boost converter and it operates in the idle mode in most situations. It is only activated online in the case of all PVs and BESSs cannot meet the total load demand. The control diagram is shown in Figure 3.22. V_{L2} is the voltage reference of voltage controller. I_L is the current flowing on the inductor of the converter. d_{BM} is the required duty ratio. M_{NRS} is the mode selection signal of NRS converter.

The control structure in BM mode is the same as the one for the other modules operating in BM mode except that the reference voltage is fixed rather than the ones determined by the external I–V droop control loop. Similarly, the mode selection signal can be scheduled to determine the appropriate operation mode.

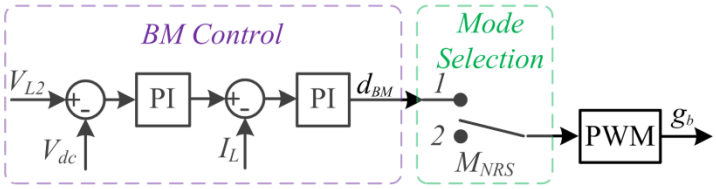

Figure 3.22. Mode selection and control diagram of NRS units.

3.6. Hardware Implementation for Verifications

3.6.1. Prototype of a lab-scale DC microgrid

To verify the proposed hierarchical control scheme, experimental tests based on a scaled-down DC grid have been carried out in WERL. As shown in Figure 3.23, the DC grid consists of two parallel PV modules, a BESS and a backup DC source as NRS.

The hardware set up of the DC grid with sources, converters, central control system and loads are shown on the top of Figure 3.24. The individual components are shown at the bottom. Three-channel modular PV converters, controlled by Silicon Labs C8051F120 microcontroller, have been developed as shown on the left bottom side of Figure 3.24. The maximum power rating of each channel is 2.5 kW. Two channels are configured as PV converters and the remaining one is used as NRS converter. A bidirectional buck-boost converter as shown in the middle bottom is developed as the BESS converter. A PV simulator with two output channels is used to emulate two PV panels. A 16×12V lead-acid battery bank with 200V nominal operating voltage serves as the BESS as shown on the right bottom side of Figure 3.24.

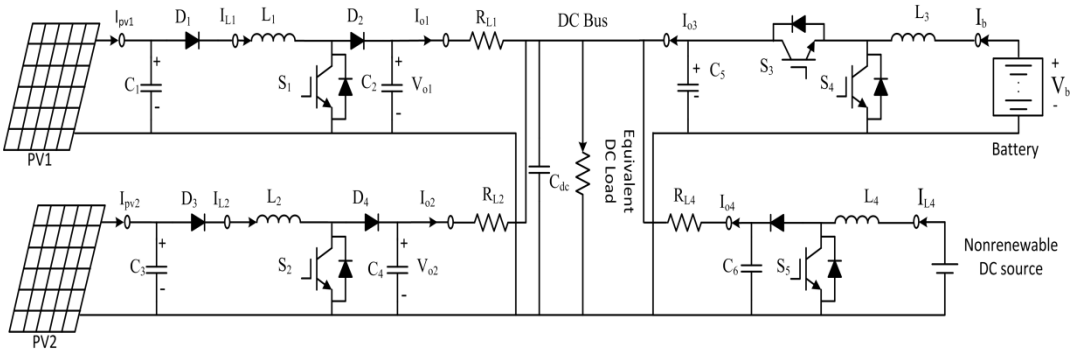

Figure 3.23. Configuration of a scale-down DC grid.

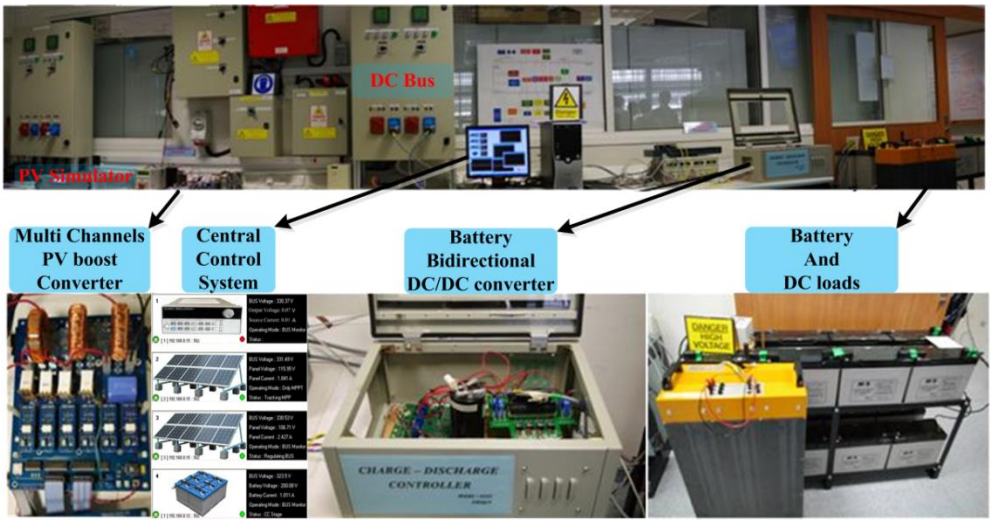

Figure 3.24. Lab scale implementations for experimental testing.

A central control system and a DC grid graphic user interface are developed as shown in the middle bottom of Figure 3.24. The DC grid interface serves as a central monitor and

controller for DC grid operations. It manages multiple PV modules, battery banks and the backup DC source by means of acquiring their operation data including voltage, current and operation status through Modbus communication. Settings of reference bus voltage and converters operation modes are also allowed.

3.6.2. Experimental results

Four case studies are presented in this section in order to illustrate four mode transfer behaviors. Case 1 shows the results when the system operation zone changes from Region 1 to Region 3. In Case 2, mode transfer between Region 2 and Region 3 is tested. Case 3 shows mode transfer results when the system operation zone changes from Sub-region A to B in Region 2. Case 4 illustrates the control mode changing from HLII to HLI once malfunction is detected in the communication links.

1) Case 1

Figure 3.25 shows the mode transfer results when the DC bus voltage changes from Region 1 to Region 3. C1 is the DC bus voltage. C2 and C4 show the gross output current and power of PV modules, respectively. C3 and C5 show the current and power of the battery converter, respectively.

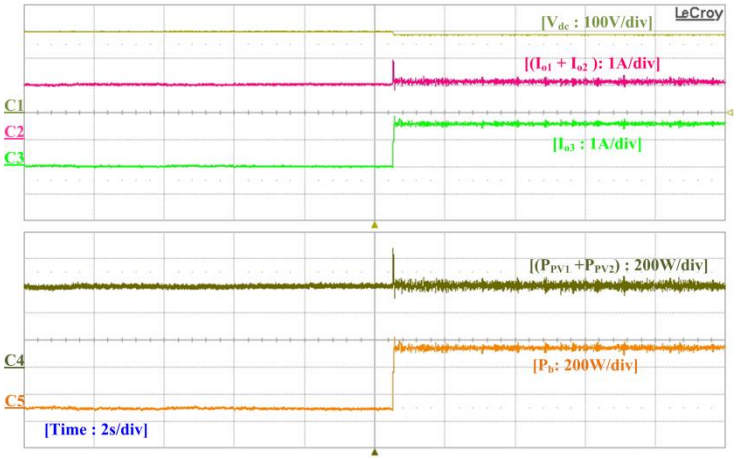

Figure 3.25. Current and power outputs of PV modules, BESS and bus voltage during mode transfer from Region 1 to Region 3.

As shown in Figure 3.25, two modular PV systems initially (before t = 10.5s) operate in Region 1 at their maximum power points (MPPT mode) of 200W and 400W to meet the 600W load demand. The bus voltage is around the nominal value 300V in Region 1

during this period. BESS operates in idle mode with zero output current (as shown in C3). At t = 10.5s, the load increases from 600W to 1100W and power generation deficiency occurs instantly. The equivalent bus capacitor temporarily supplements the power deficiency by releasing its power. This causes the bus voltage to drop below the threshold value, 285V (as shown in C1), which activates the battery converter to operate from idle mode to BM mode. BESS is then maintaining the bus voltage at about 280V through discharging approximate 500W (to see C5) to load. During the transient state, negative dv/dt in the equivalent bus capacitor leads to surge current injection into the output current of PV converters. Combination of the surge current and the maximum current from PV modules are reflected in the transient state as shown in C2. The surge currents are also reflected on the output power of PV converters as shown in C4.

2) Case 2

Figure 3.26 shows the results when the DC bus voltage changes from Region 2 to Region 3. C1 is the DC bus voltage. C2 and C5 show the current and power of battery converter, respectively.

In this case, the total maximum power of modular PV systems is approximate 900W. Equivalent DC load includes a fix load with 500W and a variable load with 600W. As shown in Figure 3.26, the DC bus voltage is initially maintained at around 320V by battery converter before t = 6s. Both PV modules in this period are operating in MPPT mode, providing power to the fixed load (500W) and battery charging (400W). At t = 6s, the variable load becomes online and the entire load increases from 500W to 1100W, causing the DC bus voltage to drop below the threshold value V_{L1}=285V. At this moment, the battery converter in reverse regulates the DC bus voltage at around 282V by supplying approximately 220W of surplus power to the entire load demand.

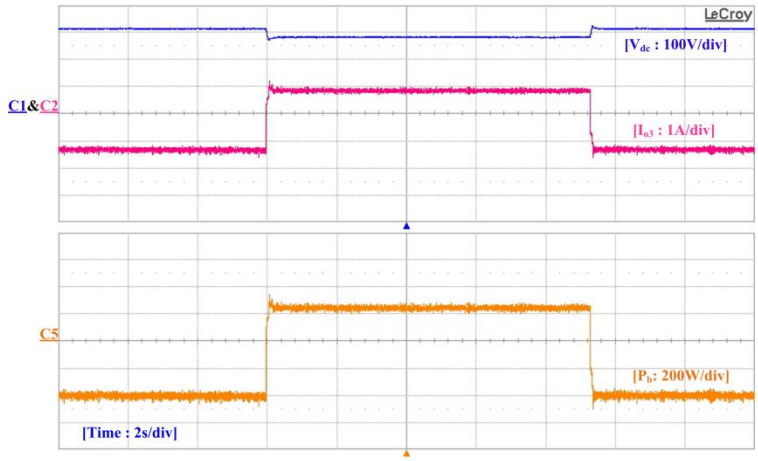

Figure 3.26. Current and power outputs of BESS and bus voltage during mode transfer between Region 2 and Region 3.

3) Case 3

Figure 3.27 shows the results when the battery converter changes from BM mode to CCC mode. C1 is the dc bus voltage. C2 and C4 show gross output current and power of PV modules, respectively. C3 and C5 show the current and power of battery converter, respectively.

In this case, the total maximum power from two modular PV systems is configured at 1200W. The fixed load is set at 200W while the variable load is set at 600W. The maximum allowable charging current for the battery is set at 4A. Therefore, the maximum charging power that BESS can absorb is about 4A×200V=800W. The experimental results are shown in Figure 3.27. Two PV modules are operating in MPPT mode, generating approximate 1200W power before t = 5s. Both the fixed and variable loads, whose total amount of power is about 800W, are online during this period. The BESS therefore absorbs nearly 400W power to maintain the DC bus voltage at around 320V. At t = 5s, the variable load goes offline. This causes the charging current to increase and eventually reaches the maximum charging current. Operation mode of BESS changes from BM to CCC mode. The threshold current is set to be 10% higher than 4A to prevent malfunction. System power surplus induces voltage increase over V_{Hx} which enables the PV modules changing from MPPT to BM to rebalance system power. In steady state, the PV modules are maintaining the DC bus voltage at around 327V and BESS operates as a power terminal with charging power of 850W.

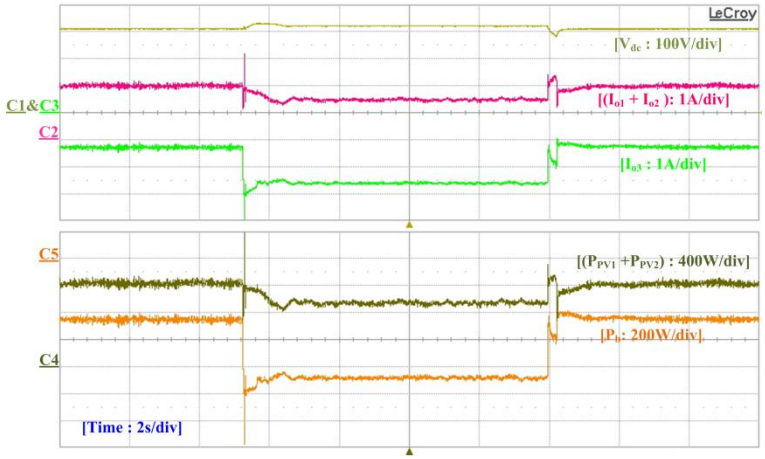

Figure 3.27. Transient performances of battery converter from BM mode to CCC mode.

The parallel modular PV systems consequently monitor the bus voltage by generating about 450W. A variable load is turned on at t=14s. At this moment, the BM controlled PV converters attempt to maintain the system power balance through increasing their output powers to the maximum value. Power supply deficiency then results in bus voltage drop. The bus voltage continues dropping to below V_{Hx}, which enables the mode change of BESS and PV modules simultaneously. Subsequently, PV modules operate at MPPT mode, whilst BESS operates at BM mode in Sub-region A.

4) Case 4

Figure 3.28 shows the results when the DC microgrid is switched from HLII to HLI control once malfunction is detected in communication links. The experimental data is measured by a DC meter with data acquisition frequency of 10 Hz and stored in the database of the central management system for further analysis.

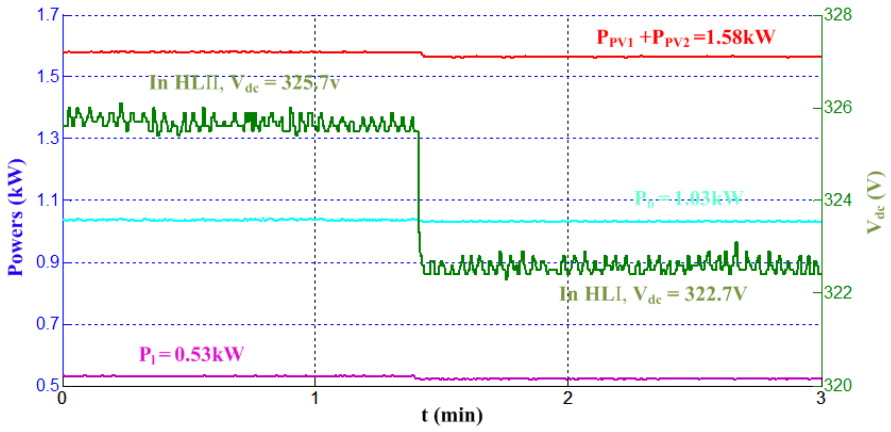

Figure 3.28. Experimental illustration when dc microgrid is controlled from HLII to HLI

during communication failure.

In Figure 3.28, he installed maximum power of PV modules is around 3kW, the maximum charging power of the storage is about 1.03kW, and the load is now configured at 0.53kW. In HLII, the instant maximum power of PV modules is set at 2kW. According to equation (3-5) by replacing the maximum values with instantaneous powers, the V_{Hx} is calculated at about 322.5V. The storage is operating at maximum current charging mode, while PV modules are operating at BM (off-MPPT) mode, monitoring the DC bus voltage at around 325.7V through generating approximately 1.58kW power to feed the load and storage at around 0.53kW and 1.03kW, respectively. A mode transfer switch is enabled at 1.4 minutes to mimic the communication failure, the system control then changes from HLII to HLI**.** The threshold value V_{Hx} in HLI is calculated using the rated capacities of all modules, which forces bus voltage to be controlled at 322.7V. The system finally reaches at a new operating point. As a consequence, the higher resolution of voltage distribution has been proved by HLII and enhanced system redundancy is achieved by HLI.

3.7. Conclusions

This chapter introduces a hierarchical control strategy for reliable and effective operations of a standalone DC microgrid. The features of the proposed hierarchical controlled DC microgrid can be summarized as: 1) maximal usage of renewable energy and reliability enhancement is achieved by HLI control; 2) real-time voltage regulation capability for power modules and prioritizations for charging/discharging of the BESS with different SoCs are considered in HLII control; 3) emergency conditions are managed by the HLIII control. Nevertheless, the reliable operation of this DC system relies heavily on the accurate measurement of the DC bus voltage, which involves DC voltage sensors with high accuracy. This would undoubtedly increase the system cost. The inaccuracy and malfunction in voltage sensor may lead to inappropriate operation of relevant modules, this situation needs to be avoided. With the proposed control method, a discrete characteristic of the DC bus voltage is described in Figure 4.2. Finally, the feasibility and effectiveness of the presented coordination control strategies for reliable and effective operation of standalone DC grids have been verified experimentally in the laboratory prototype.

Chapter 4 Global Power Sharing (GPS) Control for Autonomous Operation of Hybrid AC-DC microgrids

4.1. Introduction

Reliable operations of DC microgrids under hierarchical control scheme have been stated in previous chapter. Coupling the DC microgrid into the existing AC infrastructure with the associated power electronics interfaces forms the scenario — hybrid AC-DC microgrid. Such a complex system generally employs local controller for basic operations of power modules in the low layer and high layer energy management system (EMS) with mass information exchange for overall system optimization. What if the communication network fails or the realization of communication is difficult for widely dispersed DG systems in rural and remote areas? Is there an effective control strategy to maintain reliable operations of hybrid system without any communication links to avoid system outage?

The droop control method has shown the effectiveness on managing parallel operations of widely dispersed DG systems with the advantages of independent control without communication links and reliability improvement of overall system. So far, most of the references on droop control applied to DG have concentrated on AC grids [74-77], which is understandable based on the dominant role that AC distribution has long served in the traditional grid. Although not easily spotted, droop control applied to DC microgrids has also been proposed more than a decade back，but its popularity has not grown much since then, until quite recently when a few references have explicitly discussed about some operating issues of DC grids, other than their droop control. This interest might grow further due to the proliferation of popular green sources like photovoltaic (PV) and fuel cells, and energy storages like batteries and ultra-capacitors, which are all DC by nature. The challenge of hybrid microgrids then is to design a coordination droop control for the DC sources, AC sources and interfacing converter, so that power flow is always appropriately managed throughout the whole hybrid microgrid, regardless of whether the load change is detected in the DC, AC or both sub-grids. This effort of wireless power tuning on DGs and interlinking converter has not yet been attempted.

This chapter introduces a global power sharing (GPS) control strategy for the active power sharing of an autonomous hybrid AC-DC microgrid. The system structure of the hybrid AC-DC microgrid is demonstrated in Section 4.2. In Section 4.3, rudimentary droop control for DGs in both sub-grids is reviewed. Based on power sharing in individual AC or DC sub-grid, the principle of GPS in autonomous islanding mode, which ensures that all the DGs located in the AC and DC sub-grids will share the entire loads in proportion to their ratings, is described in detail in Section 4.4. Based on the analysis in Section 4.4, the proposed concepts are finally tested in both simulation and experiment for the four scenarios that the hybrid microgrid will operate in. With effectiveness verifications from both simulation and experiment results, the concept of hybrid AC-DC microgrid are likely to benefit renewable or nonconventional distributed generations (DGs), where both AC and DC sources are present.

4.2. System Configuration

Figure 4.1 shows an example hybrid microgrid, formed by tying a DC and an AC sub-grid together through a simple, while yet efficient, interfacing converter. The detailed system components of the example hybrid microgrid are shown in Figure 4.2. In the DC sub-grid, two paralleled DC sources with accompanied DC-DC boost converters (DG1 and DG2), line impedances and local loads are drawn, while in the AC sub-grid, two DC sources tied to two separate DC-AC inverters are drawn to represent two paralleled DG systems (DG3 and DG4) with their own line impedances and local AC loads. The two sub-grids are then tied together by the intermediate six-switch interfacing converter, whose main function is to provide bidirectional energy transfer between the two sub-grids, depending on the prevailing supply-demand conditions found within each sub-grid. As per existing AC microgrids, the hybrid microgrid drawn in Figure 4.1 can also be tied to the AC utility mains through an intelligent transfer switch. This switch will stay on under normal grid-connected mode of operation, and will break immediately to form an autonomous island upon the occurrence of a mains fault. For the former, control of the AC sub-grid is no different from previous AC microgrid control, where each AC micro-source is programmed to operate at its nominal or maximum power level with the mains voltage explicitly sensed for unity power factor tuning. This power command, upon divided by the sensed voltage amplitude, then gives rise to the corresponding current command for tracking by the micro-source, which now

behaves like a controlled current source.

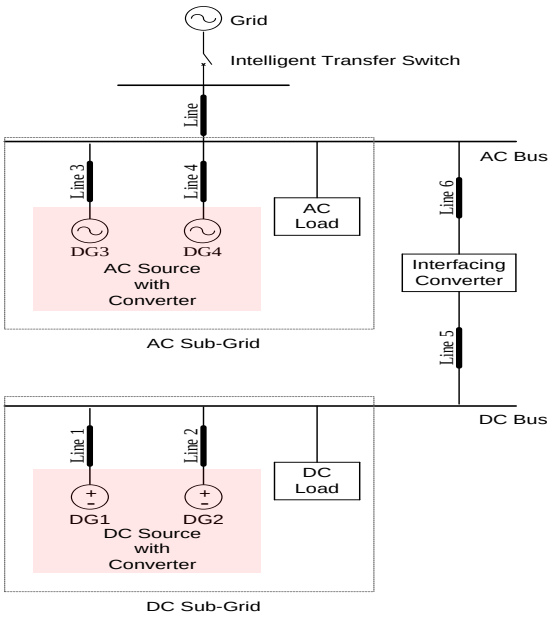

Figure 4.1. Layout of an example hybrid AC-DC microgrid.

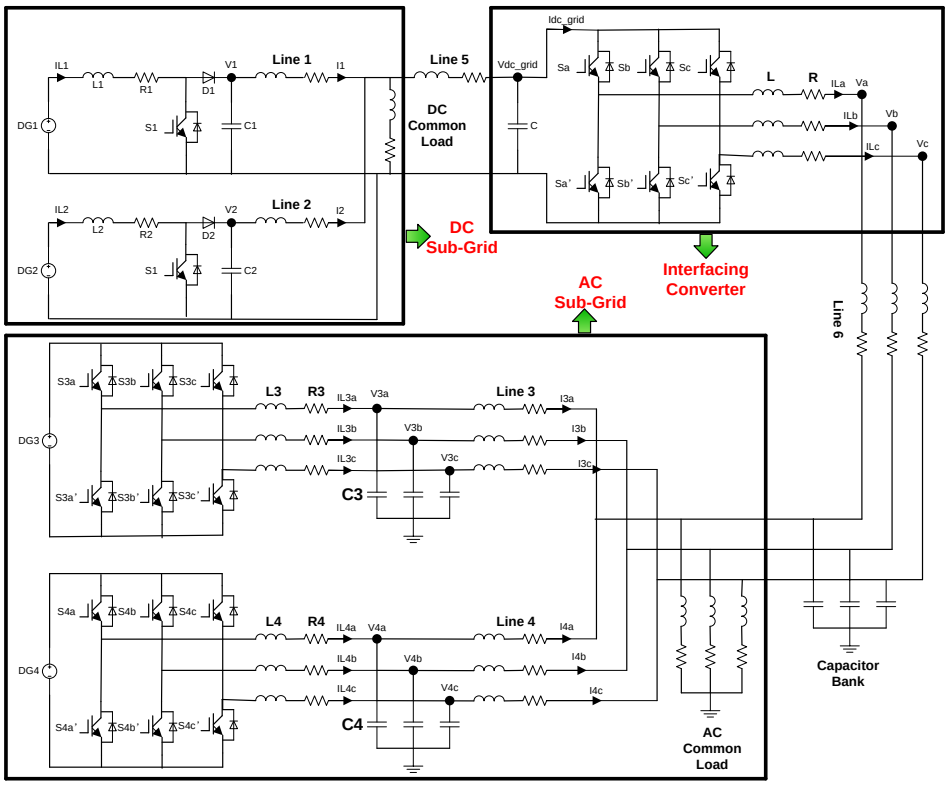

Figure 4.2. The example hybrid AC-DC microgrid with detailed system components.

Control of the DC sub-grid in the grid-connected mode is similarly achieved by setting each DC micro-source to operate at its maximum power point, while controlling the

interfacing converter to regulate its DC-link voltage using the set of firm three-phase voltages imposed by the mains. This style of control is no different from a typical solar generation system, where a DC-DC boost converter for MPPT is connected to a DC-AC inverter for grid interfacing. Because of that, control of the hybrid microgrid under grid-connected mode is not expected to be very different, and is therefore not further considered. Rather, the challenge is to investigate the power management control when the hybrid microgrid is configured to operate in the autonomous islanding mode, whose details are elaborated as follows.

4.3. Power Sharing in Individual AC or DC Microgrid

As stated in the introduction section, droop control method is usually applied to the parallel operation of widely dispersed DG systems. By applying this method, each DG module can be able to operate independently without line communication through sensing only the local voltage and current for output power calculation. Thus, the droop control is also named independent, autonomous, or wireless control [15]. In this section, the basic principle of preliminary droop control as well as its improved variants is firstly reviewed and deduced from the theory related to the power flow in the conventional AC system as follows.

4.3.1. Review of rudimentary droop control

Figure 3.8 shows the equivalent circuit of a voltage controlled PWM inverter connected to a point of common coupling (PCC) through the line impedance *Z*. The complex power drawn to the bus can be expressed as

$$S = P + jQ \tag{3-17}$$

where P and Q are the active and reactive power, respectively, which are given by

$$P = \frac{EV}{Z}cos(\theta - \delta) - \frac{V^2}{Z}cos\theta \tag{3-18}$$

$$Q = \frac{EV}{Z}sin(\theta - \delta) - \frac{V^2}{Z}sin\theta \tag{3-19}$$

where E and V are the amplitudes of the inverter output voltage and common bus voltage, δ is power angle, and Z and θ are the magnitude and the phase of the equivalent of output line impedance.

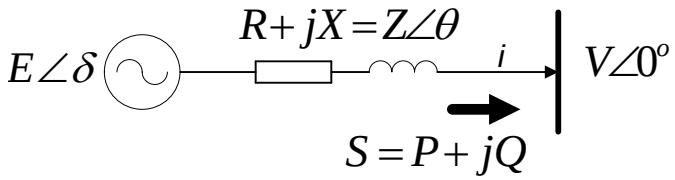

Figure 4.3. Equivalent circuit of a voltage controlled PWM inverter connected to a common AC bus.

A conventional assumption is to consider that Z is mainly inductive (θ=90°) due to the inductive output impedance of inverter, which is often justified by the large filter-inductor value. In this situation, the following well-known expressions of the active and reactive power can be derived from (4-2) and (4-3), and further simplified by considering a small phase difference δ between the inverter output voltage E and the common AC bus voltage V ($\sin\delta = \delta$ and $\cos\delta = 1$) [15]:

$$P = \frac{EV}{X}\sin\delta \approx \frac{EV}{X}\delta \tag{3-20}$$

$$Q = \frac{EV\cos\delta - V^2}{X} \approx \frac{V}{X}(E - V) \tag{3-21}$$

From the above equations, it can be seen that the active power P is primarily dependent on the power angle δ, while the reactive power Q is mainly influenced by the amplitude difference E-V. Consequently, most wireless load sharing controllers introduce artificial droops (also named virtual inertia) into the output voltage reference. Thus, P-ω and Q-V droop schemes are often adopted. The rudimentary form to implement the droop control law can be expressed as follows

$$\omega = \omega^* + m(P - P^*) \tag{3-22}$$

$$E = E^* + n(Q - Q^*) \tag{3-23}$$

where ω^* and E^* are the output-voltage frequency and amplitude at no load, and m and n are the droop frequency and amplitude coefficients. P^* and Q^* are the active and

reactive power reference, which are commonly set to zero ($P^* = 0$ and $Q^* = 0$) when the parallel inverters work in islanding mode of operation. The droop expressions in (4-6) and (4-7) become

$$\omega = \omega^* + mP \tag{3-24}$$

$$E = E^* + nQ \tag{3-25}$$

Note that although (4-4) shows a relationship between δ and P, (4-6) uses the frequency ω instead of δ. This is because the units do not know the initial phase value of the other units; however, the initial angular frequency at no load can easily be fixed as ω*. Moreover, the angular frequency ω in (4-8) can be always replaced by the frequency f.

Using this method, it is well known that if the droop coefficients are increased, then good power sharing is achieved. However, to keep the voltage variations within acceptable bounds would then requires m and n to be less gradual. Therefore, the best tradeoff between load sharing accuracy and voltage regulation would require a careful study of system before tuning m and n. For instance, the acceptable frequency and amplitude deviations are mostly at 2% and 5%, respectively. Accordingly, m and n are usually tuned by the following equations

$$m = \Delta\omega / P_{nom} \tag{3-26}$$

$$n = \Delta E / 2Q_{nom} \tag{3-27}$$

where $\Delta\omega$ and Δe are the maximum allowed frequency and voltage deviations, and P_{nom} and Q_{nom} are nominal P and Q provided by the DG system, respectively. To ensure proper load sharing according to inverter rating, the droop coefficients have to be adjusted according to the following relationships [74]

$$m_1 S_1 = m_2 S_2 = m_3 S_3 = \cdots = m_n S_n \tag{3-28}$$

$$n_1 S_1 = n_2 S_2 = n_3 S_3 = \cdots = n_n S_n \tag{3-29}$$

where S_i is the apparent power of the inverter i.

The inverter output impedance is usually assumed to be inductive, which is often justified by the high inductive components of the line impedance and the large inductance of the output filter. However, this is not always true, since the closed-loop output impedance also depends on the control strategy, and the line impedance is predominantly resistive for low voltage levels. Thus, (4-4) and (4-5) can be recalculated by considering a general output impedance of each inverter $Z\angle\theta$. By expanding (4-2) and (4-3), the active and reactive powers injected to the bus by every unit can be expressed as [78]

$$P = (\frac{EV}{Z}cos\delta - \frac{V^2}{Z})\ \cos\theta + \frac{EV}{Z}sin\delta sin\theta \tag{3-30}$$

$$Q = (\frac{EV}{Z}cos\delta - \frac{V^2}{Z})\ sin\theta - \frac{EV}{Z}sin\delta cos\theta \tag{3-31}$$

Observing from (4-14) and (4-15), the following relationship can be obtained in (4-16) and (4-17). Similarly, the relationship deduced from (4-14) and (4-15) can be simplified by considering a small phase difference δ between the inverter output voltage E and the common AC bus voltage V ($\sin\delta = \delta$and $\cos\delta = 1$):

$$Psin\theta - Qcos\theta = \frac{EV}{Z}sin\delta \approx \frac{EV}{Z}\delta \tag{3-32}$$

$$Pcos\theta + Qsin\theta = \frac{EV}{Z}sin\delta \approx \frac{EV}{Z}\delta \tag{3-33}$$

Consequently, the general form of droop control method can be expressed as

$$\omega = \omega^* + m(Psin\theta - Qcos\theta) \tag{3-34}$$

$$E = E^* + n(Pcos\theta + Qsin\theta) \tag{3-35}$$

The general droop control expressions (4-18) and (4-19) indicate that the output impedance angle θ determines specified droop control low, as shown in Table 4.1.

Table 4.1. Output impedance impacts over power flow controllability.

Output impedance	$Z=jX$ (inductive: $\theta=90°$)	$Z=R$ (resistive: $\theta=0°$)
Active Power (P)	$P=\frac{EV}{X}sin\,\delta\approx\frac{EV}{X}\delta$	$P=\frac{EV\,cos\,\delta-V^2}{R}\approx\frac{V}{R}(E-V)$
Reactive Power (Q)	$Q=\frac{EV\,cos\,\delta-V^2}{X}\approx\frac{V}{X}(E-V)$	$Q=\frac{EV}{R}sin\,\delta\approx-\frac{EV}{R}\delta$
Frequency Droop (ω)	$\omega=\omega^*-mP$	$\omega=\omega^*+mQ$
Amplitude Droop (E)	$E=E^*-nQ$	$E=E^*-nP$
m	$\Delta\omega/P_{nom}$	$\Delta\omega/2Q_{nom}$
n	$\Delta E/2Q_{nom}$	$\Delta E/P_{nom}$

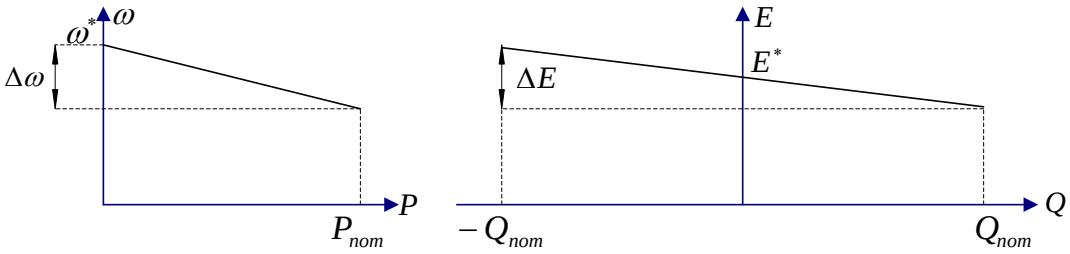

(a)

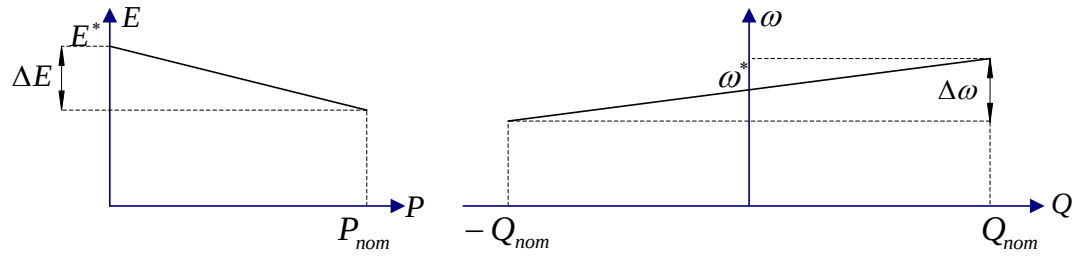

(b)

Figure 4.4. Droop control functions for (a) inductive output impedance and (b) resistive output impedance.

It can be seen from Table 4.1 that the control lows for different line impedance ($Z=jX$ and $Z=R$) are quite different. Table 4.1 specifically demonstrates that a control scheme based on P-ω and Q-V droops should be used for inductive impedance, while for resistive impedance the reverse P-V and Q-ω droops are suitable. Thus, the line impedance has a considerable effect on the power-sharing accuracy of the P/Q droop method. For this reason, it is important to design the output impedance properly in order to improve complete decoupling between active and reactive power and consequently avoid the impact of line impedance on the power sharing [77]. Table 4.1 also shows that

the controller gains *m* and *n* are chosen as a function of the nominal values of *P* and *Q*, and the acceptable maximum deviations in frequency $\delta\omega$ and amplitude δE. Accordingly, Figure 4.4(a) and (b) show the droop characteristics for pure inductive output impedance and resistive output impedance, respectively.

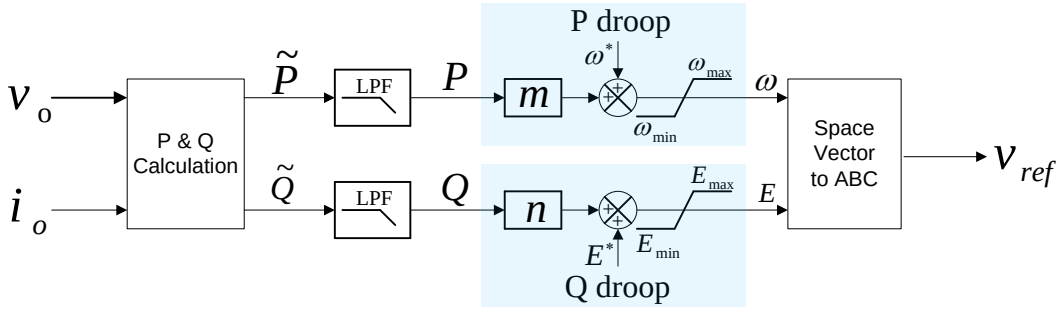

Figure 4.5. Block diagram of the rudimentary droop control method.

Based on the above description on the rudimentary droop control method, the block diagram of the basic droop method for power sharing among DGs in AC grid is drawn in Figure 4.5. The output voltage and current are initially measured for calculating the output active *P* and reactive power *Q*, which would be then filtered by low-pass filters in order to obtain the average active and reactive power. The average powers are then fed into the droop controllers with deducing the reference ω and voltage magnitude *E* of the source inverters. Finally, the reference ω and voltage magnitude *E* are synthesized to reference three-phase voltage which perform as the reference value of the voltage source inverter (VSI) based DGs.

4.3.2. Review of improved variants of droop control

Although the possibility of operation with no communications signals between parallel DG units is a very attractive feature, the conventional droop method described in last section has several inherent disadvantages [75, 79]: 1) the load-sharing accuracy is strongly affected by the output impedance and the line impedance unbalances; 2) the harmonic power in case of supplying nonlinear load is poorly compensated; and 3) an inherent tradeoff exists between the load-sharing accuracy and the output voltage regulation. To overcome the pre-mentioned drawbacks, some improved control solutions based on rudimentary droop technique have been investigated. This sub-section will briefly introduced the existing improved droop techniques.

1) Droop control with virtual output impedance

It is known that the inverter output impedance has a considerable effect on the load-sharing accuracy of the *P/Q* droop method. A possible solution to the line impedance problem consists of adding an inductor in series with the inverter output [76] in order to fix the output impedance. However, this inductor is heavy and bulky, increasing the size and the cost of equipment. Alternatively or complementary to the use of local signal communications, it is often used as a fast control loop, called virtual output impedance, which adopt the control solution to fix the output impedance of the inverter.

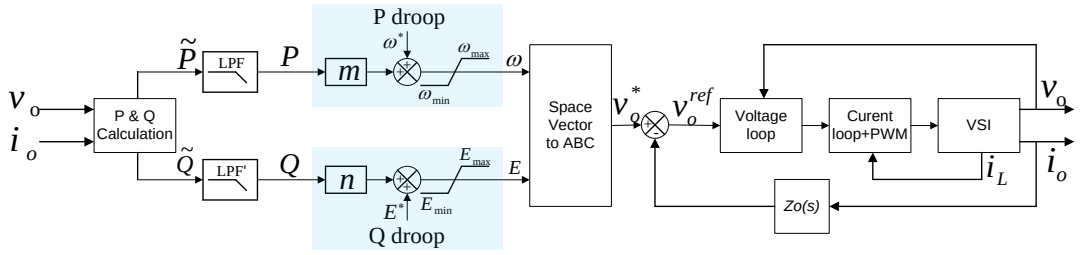

Figure 4.6. Block diagram of the closed-loop VSI with the virtual output impedance path.

In theory, this virtual impedance should be larger than the combined values of the output impedance of the VSI plus the maximum power line impedance. In [77], the virtual output impedance is expressed as

$$v_o^{ref} = v_o^* - i_o Z_o(s) \tag{3-36}$$

where $Z_o(s)$ is the transfer function of the virtual output impedance, v_o^* is the voltage reference calculated by the *P/Q* sharing loop, and v_o^{ref} is the voltage reference provided to the inner voltage control loops. According to (4-20), Figure 4.6 shows the block diagram of a droop controller with the virtual output impedance loop. The value of the output impedance must be selected following a similar way as the *m* and *n* coefficients, according to the nominal apparent power S_x of each VSI unit.

$$Z_{o1}S_1 = Z_{o2}S_2 = \cdots = Z_{on}S_n \tag{3-37}$$

By introducing this virtual impedance to the original control loop, the output impedance has become a control variable of the DG system.

2) **Droop control with power derivative and integral terms**

The conventional droop method has several intrinsic problems related to its limited transient response, since the system dynamics depends on the power-calculation filter characteristics, the droop coefficients, and the output impedance. These parameters are determined by the line-frequency, the maximum allowed frequency and amplitude deviations, and the nominal output power. Thus, by using conventional droop method, the inverter dynamics cannot be independently controlled. To overcome the dynamics of the system, the following improved droop control schemes with the power derivative and integral terms is proposed [80],

$$\phi = -m\int_{-\infty}^{t} P d\tau - m_P P - m_d \frac{dP}{dt} \tag{3-38}$$

$$E = E^* - nQ - n_d \frac{dQ}{dt} \tag{3-39}$$

where n_d is the derivative coefficient of the reactive power Q; m, m_p, and m_d are the integral, proportional, and derivative coefficients of the active power P. If $\omega = d\emptyset/dt$ is taken into account, the steady-state *P/Q* droops coincide exactly with those obtained with the basic droop method as expressed in (4-6) and (4-7). According to (4-22) and (4-23), the block diagram of droop control with power derivative and integral terms is shown in Figure 4.7. This proposed control scheme modifies the control expressions, acting on the transient response, and, at the same time, keeping the static droop characteristic. Also, it minimizes the transient circulating current among the units and further improves the dynamic performance of the whole system.

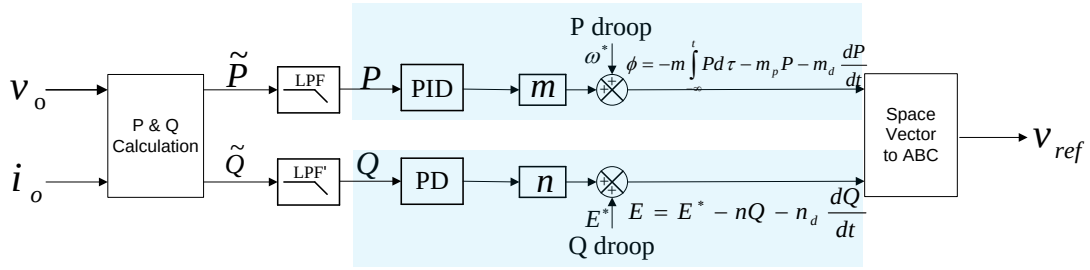

Figure 4.7. Block diagram of improved droop control with power derivative and integral terms for enhancing system transient stability.

3) Droop control with harmonic current sharing

One of the disadvantages of the conventional droop control method is its poor load-sharing when supplying nonlinear load. Commonly, the current total harmonic distortion (THD) can be up to 150%, i.e., the sum of the harmonic current root mean square (RMS) values can be up to 1.5 times the fundamental harmonic component. Hence, the parallel DG modules must be able to share these harmonics. If the paralleled modules cannot ensure sharing of these harmonics, then the system will be severely degraded in the presence of nonlinear loads. This provides the motivation for sharing the current distortion components induced by nonlinear loads as well as the fundamental components associated with both linear and nonlinear loads.

In [75], the distorted power is obtained by subtracting the output active power *P*, and reactive power *Q* from the apparent power *S* as the following equation

$$D = \sqrt{S^2 - P^2 - Q^2} \tag{3-40}$$

where D is the distorted power (VA). The distorted power is due to the combination of voltage and current components of different frequencies. It should be noticed that there is no active power in these harmonic terms, but reactive power only.

Unlike the fundamental reactive power, the flow of the distortion power cannot be influenced by adjusting the fundamental component of the inverter voltage alone. One method of solving this problem is to adjust the gain of the voltage loop as a function of the distortion power as shown in Figure 4.8.

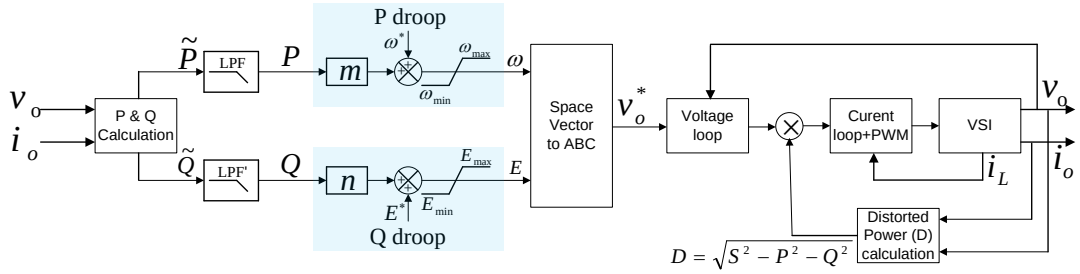

Figure 4.8. Block diagram of droop control with distorted power sharing.

By reducing the gain (and bandwidth) of the voltage loop in the presence of distortion components, the output impedance in the high-frequency range is increased, and the harmonic power sharing is automatically done.

4.3.3. Power sharing in AC microgrids

The rudimentary droop control and its advanced variants have been reviewed in previous sub-sections. For the rudimentary droop control, it generally uses two droop control equations for deducing its source converter reference frequency *f* and voltage amplitude *E* from the measured active *P* and reactive power *Q*, respectively. Assuming that the line impendence of each DG unit in the AC microgrid is pure inductive, the basic droop functions for *u* DG units can be expressed as (4-25) and (4-26) for illustrative purposes, and drawn in Figure 4.9 for showing the drooping gradients *m* and *n*.

$$f = f^* + m_x P_{ac\_x} \tag{3-41}$$

$$E_x = E^* + n_x Q_{ac}, \text{ for } x = 1, \ldots, u. \tag{3-42}$$

where subscript *x* represents the DG index in AC microgrid, f^* and E^* are the reference frequency and voltage amplitude at no load condition, respectively. The reference frequency is selected as the system maximum allowable frequency f_{max}, while the reference amplitude is preferably selected as the nominal operation voltage as shown in Figure 4.9. P_{ac_x} and Q_{ac_x} are the calculated active and reactive power of x^{th} DG unit, respectively. And m_x and n_x are the negative droop coefficients, representing the negatively tilting gradients as shown in Figure 4.9. The negative droop coefficients can be designed according to (4-10) and (4-11) as

$$m_x = \frac{f_{min} - f_{max}}{P_{ac\_x}^{nom}} \tag{3-43}$$

$$n_x = \frac{E_{min} - E_{max}}{2Q_{ac\_x}^{nom}} \tag{3-44}$$

where f_{min}, f_{max}, E_{min}, and E_{max} are minimum and maximum allowable frequency and voltage amplitude, respectively. $P_{ac\_x}^{nom}$ and $Q_{ac\_x}^{nom}$ are the nominal active and reactive power for x^{th} DG unit, respectively.

Considering that the intention of this research work is the development of a control scheme for GPS based on coordination design on basic droop equations of both sub-grids, reactive power sharing is henceforth not taken into account. Therefore, combining (4-25) and (4-27) results in

$$\frac{P_{ac\_1}}{P_{ac\_1}^{nom}} = \frac{P_{ac\_2}}{P_{ac\_2}^{nom}} = \cdots = \frac{P_{ac\_u}}{P_{ac\_u}^{nom}} \tag{3-45}$$

It is indicated in (4-29) that u DG units in AC sub-grid will rightfully share the load demand in proportion to their nominal powers.

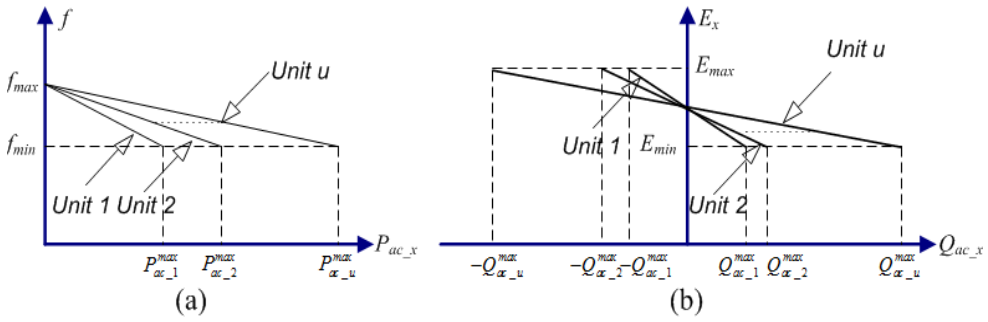

Figure 4.9. Droop characteristics for DGs in AC sub-grid.

Quite obviously, the control objective of sharing power proportionally among the AC DGs will cause their reference terminal voltages to vary with the grid demanded active and reactive power. Keeping the voltage variations within acceptable bounds will then requires the gradients m and n to be less gradual, but that will compromise the load sharing accuracy. The best tradeoff will therefore require a careful study of the system,

before tuning *m* and *n* accordingly [81]. As mentioned in last section, an alternative solution for improving system transient stability is to modify the basic equations of (4-25) and (4-26) in the way described in [80]. This however is not attempted here, since the intention is to show that the overall proposed GPS for the hybrid microgrid works fine even for the simplest droop control case, and is therefore not technically dependent on any existing advanced features.

Combining the values determined from (4-25) and (4-26) gives rise to the demanded voltage reference $V_{3\_abc}^{ref}$ as explicitly indicated at the top of Figure 4.10. The constructed voltage reference is then fed to the dual-loop voltage regulator drawn at the bottom of Figure 4.10, where an inner proportional current loop and an outer proportional-resonant (PR) voltage loop are drawn. Sizing of control parameters for this regulator is important, since it affects the tracking accuracy and output impedance.

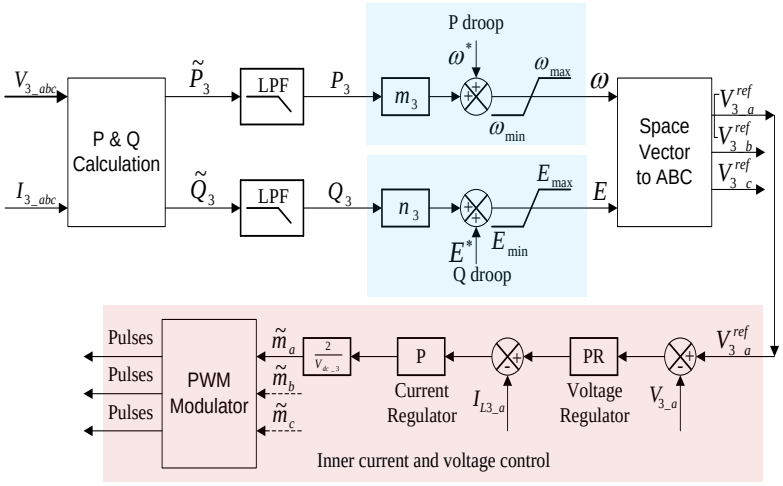

Figure 4.10. Control scheme for AC micro-sources DG3 and DG4.

4.3.4. Power sharing in DC microgrids

Unlike the AC sub-grid, the DC sub-grid is much simpler in the sense that it does not have reactive power, and the only voltage quantity available for control is its amplitude. With zero phase and resistive (non-reactive) DC lines, it is clear that active power is no longer dependent on the frequency, but solely varies with the voltage difference $V_{dc\_y} - V_{dc}$, where V_{dc_y} is the terminal voltage of y^{th} DG unit in DC sub-grid and V_{dc} is the DC bus voltage. Because of that and as briefly mentioned in [82], active power *P* sharing

among the DC DGs can hence be provided by drooping their DC source voltages V_{dc_y} according to (4-30).

$$V_{\mathrm{d}\,c\,y\_} = V_{d\,c}^{*} + d_{y} P_{d}, \quad \text{for } y = 1, \ldots, v. \tag{3-46}$$

where subscript y represents the DG index in the DC sub-grid, V_{dc}^{*} is the reference frequency and configured at the maximum allowable voltage. V_{dc_y} is the terminal voltage of y^{th} DG unit and d_y is the negative droop coefficient and is given by

$$d_{y} = \frac{V_{dc}^{min} - V_{dc}^{max}}{P_{dc\_y}^{nom}} \tag{3-47}$$

where V_{dc}^{min} and V_{dc}^{max} are the minimum and maximum allowable voltages in the DC sub-grid, respectively. $P_{dc\_y}^{max}$ is the nominal output power for y^{th} DG unit.

Unlike an AC system whose frequency is unique throughout the system at steady state, the terminal voltage of each DG unit in DC microgrid is slightly different due to the voltage drop across the cable as demonstrated in Figure 4.11(a). This will lead to the power sharing inaccuracy among DG modules [62]. To solve this inherent problem in DC system, a modified droop equation is developed as

$$V_{\mathrm{dc}\_y} = V_{dc}^{*} + d_{y} P_{dc\_y} + i_{dc\_y} Z_{dc\_y} \tag{3-48}$$

where i_{dc_y} and Z_{dc_y} are the output current and resistive cable impedance of y^{th} DG unit, thus, $i_{dc\_y}\, Z_{dc\_y}$ is voltage drop on y^{th} cable. Rearranging (4-32) follows that

$$V_{\mathrm{dc}\_y} - i_{dc\_y} Z_{dc\_y} - V_{dc}^{*} = d_{y} P_{dc\_y} \Rightarrow V_{\mathrm{dc}} - V_{dc}^{*} = d_{y} P_{dc\_y} \tag{3-49}$$

In (4-33), V_{dc} is the unique DC-bus voltage, performing like the role of frequency in AC system. The modified droop characteristic is shown in Figure 4.11(b). By modifying the basic droop expression into (4-33), the accurate power sharing can be established as

$$\frac{P_{dc\_1}}{P_{dc\_1}^{nom}} = \frac{P_{dc\_2}}{P_{dc\_2}^{nom}} = \cdots = \frac{P_{dc\_v}}{P_{dc\_v}^{nom}} \tag{3-50}$$

It is indicated from (4-34) that *v* DG units in DC microgrid will rightfully share the load demand in proportion to their nominal powers.

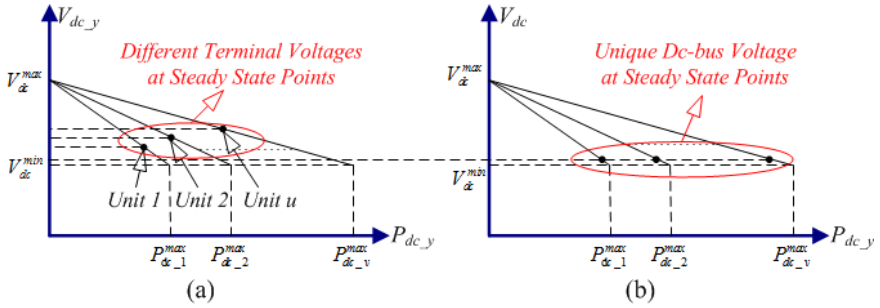

Figure 4.11. Droop characteristics of DGs in DC sub-grid: (a) basic droop; (b) modified droop.

To preliminarily illustrate the improvement in power sharing accuracy, the modified droop equation is applied to the control of DG units in a two-source DC microgrid as shown in Figure 4.12. Details of the system parameters are given in Table 4.2.

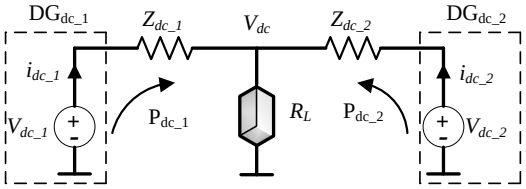

Figure 4.12. Equivalent circuit of a two-source DC microgrid.

The simulation results are provided in Figure 4.13 to compare the power sharing accuracy under the basic and modified droop control methods. In state 1, the basic droop equation (4-30) is used for power sharing control of two DG units. The output power of two DG units are P_{dc_1}=3545W and P_{dc_2}=4250W, respectively. The ratio P_{dc_1}/P_{dc_2} is numerically quite different to the ratio $P_{dc\_1}^{nom}/P_{dc\_2}^{nom} = 2/3$, which implies that the power sharing among two DG modules is not accurately proportional to their ratings due to the voltage drop on the cable. The modified droop control as expressed in (4-33) is enabled at t=1s, the system then operates in state 2. With modified droop control, the output power of two DG units change to P_{dc_1}=3202W and P_{dc_2}=4803W, respectively. The

ratio $P_{dc\_1}/\ P_{dc\_2}$ becomes quite close to the ratio $P_{dc\_1}^{nom}/P_{dc\_2}^{nom}=2/3$, which elucidates that two DG units can accurately share the DC load in proportion to their ratings by considering the cable voltage drop in the droop characteristics.

Table 4.2. Parameters of two-source DC Microgrid.

Parameters	Value (units)
Nominal Voltage: V_{dc}^{n}	700V
V_{dc}^{max}	720V
V_{dc}^{min}	680V
Z_{dc_1}	1Ω
Z_{dc_2}	2Ω
Load Resistor: R_L	60Ω
$P_{dc\_1}^{max}$	4000W
$P_{dc\_2}^{max}$	6000W

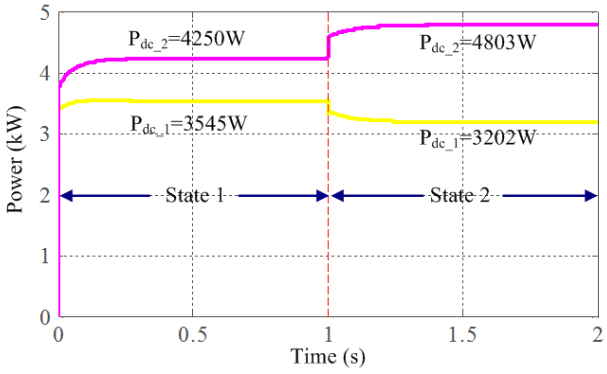

Figure 4.13. Simulation verifications of modified droop characteristics for DG units in a two-source DC microgrid.

The control block realization of (4-33) is shown at the top of Figure 4.14, and as per the AC sub-grid, coefficient *d* should be tuned appropriately since a steeper slope will lead to better power sharing, but wider voltage variations, which might not be acceptable by international specified standards. The voltage reference V_1^{ref} computed by (4-33) for each DC micro-source is then fed to its voltage regulator drawn at the bottom of Figure 4.14. The voltage regulator consists of an outer PI voltage controller and an inner proportional current controller, which forces the output voltage of DG to track the calculated reference voltage.

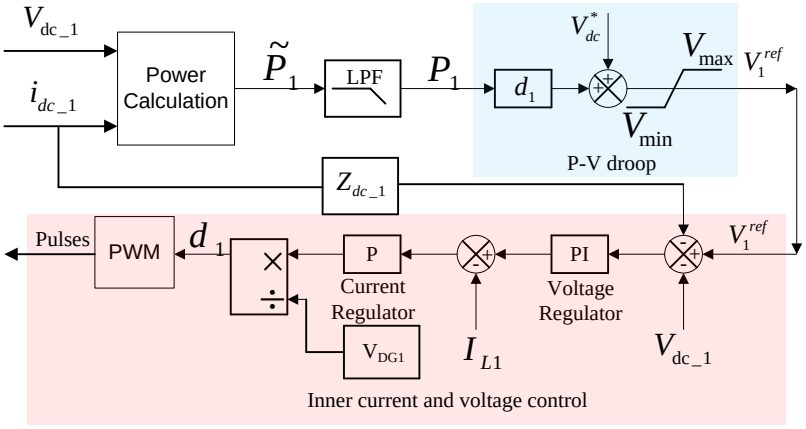

Figure 4.14. Control scheme for DGs in DC sub-grid.

4.4. Global Power Sharing throughout a Hybrid AC/DC Microgrid

4.4.1. Principle of global power sharing

Control schemes described in the earlier two sub-sections will allow the DGs to share their local loads in the respective sub-grids. Upon knowing power sharing in individual AC or DC sub-grid, the follow-up requirement is to explore a reasonable rule of power exchange between two sub-grids. With this in mind, the GPS is subsequently proposed to realize power sharing throughout both sub-grids, regardless of whether the DGs are placed in the AC or DC sub-grid. Advantages of such wider scope of power sharing are summarized as follows [83-85]:

a) Any single point of failure due to overstress in certain source can be avoided;
b) Sources with slower response to load transients are expected to have smaller variations, thus resulting in short transient period;
c) Design of the capacity of each sub-grid will no longer be constrained by their respective local load profiles. Rather, their capacities can be chosen according to the entire load profiles since DGs in one network can be viewed as a back-up reserve for the another;
d) All elements are managed in a decentralized manner without information exchange. This provides an emergency operation scheme during communication failures for complex system with mass communications.

The above advantages cannot be achieved by just relying on droop controlled DGs in individual AC or DC sub-grid. The point becomes to the development of proper control scheme on power tuning for the interlinking converter (IC).

(a) The IC has to manage bidirectional active power flow between two sub-grids, where positive and negative polarities stand for forward DC-AC and reverse AC-DC power flow, respectively. This scenario is different from DGs with unidirectional power outputs.
(b) At any instant, the IC has to perform two roles. It performs as the supply end to one sub-grid who absorbs the power from IC, and appear as the demand end to the other sub-grid who releases the power to IC.
(c) The two sets of droop equations with different y-axis dimensions need to be derived before arriving at the final active power command to be transferred to the IC for GPS realization.

The aforementioned complexities can be managed by a normalization process. By using the normalization method, the principle of GPS is interpreted by means of mathematical and graphical methods as follows.

In AC sub-grid, summation of all sub-equations in (4-25) while ignoring the power losses due to switching actions and transmission lines follows the combined AC droop characteristics as

$$f = f^* + M\sum_{x=1}^{u} P_{ac\_x} \tag{3-51}$$

$$M = 1\Big/\sum_{x=1}^{u}\frac{1}{m_x} \tag{3-52}$$

where $\sum_{x=1}^{u} P_{ac\_x}$ is the gross active power generated from all u DG units in AC sub-grid. M is the negatively droop coefficient of combine droop characteristics in AC sub-grid as shown in Figure 4.15.

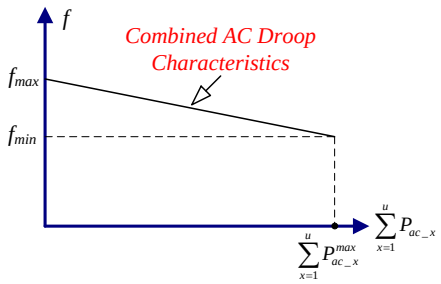

Figure 4.15. Combined AC droop characteristics.

On the DC side, summation of all sub-equations in (4-33) follows the combined DC droop characteristics as

$$V_{dc} = V_{dc}^{*} + D\sum_{y=1}^{v} P_{dc\_y} \tag{3-53}$$

$$D = 1 \Big/ \sum_{y=1}^{v} \frac{1}{d_y} \tag{3-54}$$

where $\sum_{y=1}^{v} P_{dc\_y}$ is the gross active power generated from all v DG units in DC sub-grid. D is the negatively droop coefficient of the combined droop characteristics in DC sub-grid as shown in Figure 4.16.

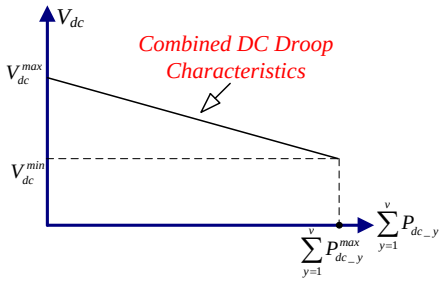

Figure 4.16. Combined DC droop characteristics.

Upon obtaining the combined droop expression of each sub-grid, a normalization method is used to merge the two variables f and V_{dc} in (4-35) and (4-37) with different dimensions as

$$(\gamma)'=\begin{cases}\dfrac{\gamma-\gamma_n}{\gamma_{max}-\gamma_n}, & for \quad \gamma>\gamma_n \\ \dfrac{\gamma_n-\gamma}{\gamma_{min}-\gamma_n}, & for \quad \gamma<\gamma_n\end{cases} \tag{3-55}$$

where γ represents the variable f or V_{dc}, $(\gamma)'$ denotes the normalized variable. γ_n is variable's nominal value, and γ_{max}, γ_{min} are the variable's maximum and minimum values, respectively. Assuming that γ_{max} and γ_{min} are symmetric compared to γ_n, (4-39) can therefore be written as

$$(\gamma)'=\frac{\gamma-0.5(\gamma_{max}+\gamma_{min})}{0.5(\gamma_{max}-\gamma_{min})} \tag{3-56}$$

Equation (4-40) indicates that the normalized value $(\gamma)'$ varies between -1 and 1. Substituting the relevant normalized variable into (4-35) and (4-37) follows that

$$(f)'=1+\frac{M}{0.5(f_{max}-f_{min})}\sum_{x=1}^{u}P_{ac\_x} \tag{3-57}$$

$$(V_{dc})'=1+\frac{D}{0.5(V_{dc}^{max}-V_{dc}^{min})}\sum_{y=1}^{v}P_{dc\_y} \tag{3-58}$$

(4-41) and (4-42) are the normalized combined droop characteristics of AC and DC sub-grids, respectively. Recalling the definitions of m_x and d_y in (4-27) and (4-31), (4-41) and (4-42) can be transformed to (4-43) and (4-44), respectively, as follows

$$(f)'=1-\frac{1}{0.5\sum_{x=1}^{u}P_{ac\_x}^{nom}}\sum_{x=1}^{u}P_{ac\_x} \tag{3-59}$$

$$(V_{dc})'=1-\frac{1}{0.5\sum_{y=1}^{v}P_{dc\_y}^{nom}}\sum_{y=1}^{v}P_{dc\_y} \tag{3-60}$$

where $\sum_{x=1}^{u}P_{ac\_x}^{nom}$, $\sum_{y=1}^{v}P_{dc\_y}^{nom}$ are summations of the nominal powers of u and v DG units, respectively. According to (4-43) and (4-44), the normalized droop characteristics of AC and DC buses are drawn in Figure 4.17(a) and (b), respectively.

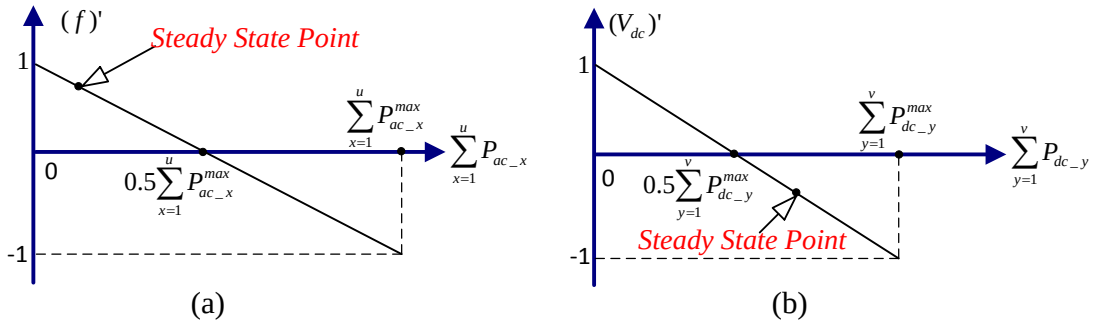

Figure 4.17. Combined normalized droop droop characteristics of (a). AC sub-grid; (b). DC sub-grid.

With the normalization process, the combined droop characteristics of two sub-grids have same dimensions on x and y axis. Therefore, they can be placed in the same frame of reference with common vertical and horizontal axis as shown in Figure 4.18.

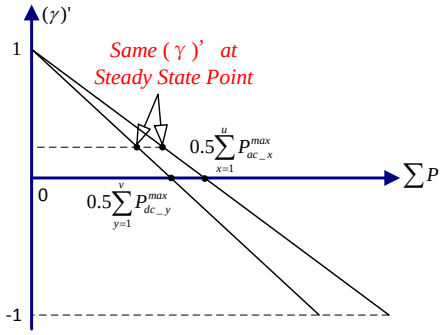

Figure 4.18. Global power sharing realization.

Realization of GPS can then be inferred from power sharing in each sub-grid, whose f / V_{dc} are inherently unique to ensure proportional power sharing among DGs. The attempt is to establish the same role in hybrid AC/DC system. With this intention, $(f)'$ and $(V_{dc})'$ are hereby intentionally equalized by a PI controller as,

$$P_{IC} = \left[(V_{dc})' - (f)'\right]\left(k_p + \frac{k_i}{s}\right) \tag{3-61}$$

where P_{IC} is the power flow in the IC as shown in Figure 4.1, positive and negative polarities of P_{IC} stand for forward DC-AC and reverse AC-DC power flow. k_p, k_i are positive controller gains. The responsibility of the PI controller is to eliminate the steady-state error between $(f)'$ and $(V_{dc})'$. By enforcing $(f)'$ = $(V_{dc})'$ as drawn in

Figure 18, it can be deduced from (4-43) and (4-44) that

$$\frac{\sum_{x=1}^{u} P_{ac\_x}}{\sum_{x=1}^{u} P_{ac\_x}^{nom}} = \frac{\sum_{y=1}^{v} P_{dc\_y}}{\sum_{y=1}^{v} P_{dc\_y}^{nom}} \tag{3-62}$$

Combining (4-29), (4-34) and (4-46) follows that

$$\frac{P_{ac\_1}}{P_{ac\_1}^{nom}} = \frac{P_{ac\_2}}{P_{ac\_2}^{nom}} = \cdots = \frac{P_{ac\_u}}{P_{ac\_u}^{nom}} = \frac{\sum_{x=1}^{u} P_{ac\_x}}{\sum_{x=1}^{u} P_{ac\_x}^{nom}} = \frac{\sum_{y=1}^{v} P_{dc\_y}}{\sum_{y=1}^{v} P_{dc\_y}^{nom}} = \frac{P_{dc\_1}}{P_{dc\_1}^{nom}} = \frac{P_{dc\_2}}{P_{dc\_2}^{nom}} = \cdots = \frac{P_{dc\_v}}{P_{dc\_v}^{nom}} \tag{3-63}$$

It is implied from (4-47) that, by exchanging the amount of power P_{IC} between two sub-grids, all DGs either in AC or DC sub-grid can share the entire load in proportion to their nominal powers throughout the hybrid AC/DC system. The whole process of GPS is also demonstrated in Figure 4.19.

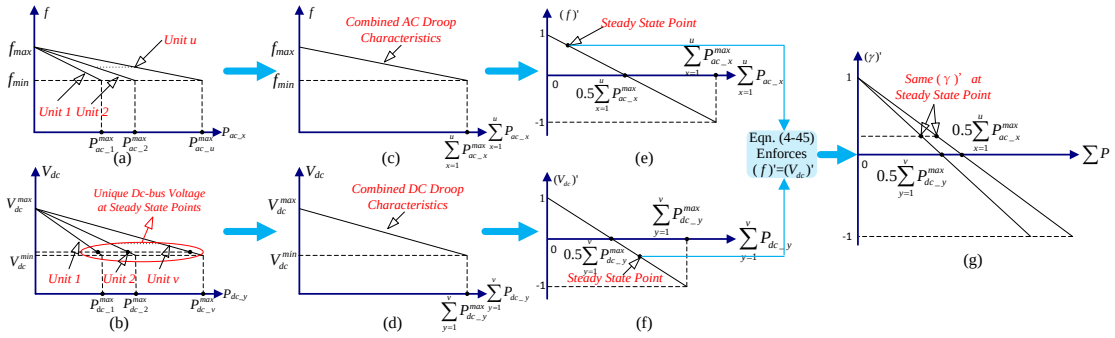

Figure 4.19. Illustration of GPS principle: (a) & (b) individual droop characteristics; (c) & (d) combined droop characteristics; (e) & (f) normalized combined droop characteristics; (g) GPS realization.

To show how Figure 4.19 helps the IC to provide proper power tuning principle, four cases can be tested, depending on the polarities of $(V_{dc})'$ and $(f)'$. The following documents the four cases.

(a) $(V_{dc})' \gg (f)'$: According to Figure 4.19(e) and (f), this relative scenario means those DGs in the AC sub-grid producing more power to meet its higher load demand than those operating in the DC sub-grid with a comparably lower load demand. Excess power therefore exists in the DC sub-grid, which can be transferred to the AC sub-grid by the interfacing converter to meet its higher demand. The actual amount of transferred power P_{IC} is determined by (4-45), whose positive value matches to power flowing from the DC to AC side.

(b) $(V_{dc})' \ll (f)'$: On the contrast, when the variable $(f)'$ is much larger than $(V_{dc})'$, which means those DGs in the DC sub-grid producing more power to meet its higher load demand than those operating in the AC sub-grid according to Figure 4.19(e) and (f). Thus, excess power exists in the AC sub-grid, which can be transferred to the DC sub-grid by the interfacing converter to meet its higher demand. In this loading condition, the polarity of P_{IC} becomes negetive which indicates the power flow on the interfacing converter is from AC to DC side.

(c) $(V_{dc})' \approx (f)'>0$: This scenario means that both the DC and AC sub-grids have additional power capacities for the interfacing converter to absorb. Therefore, the correct response expected from the interface should either be no or only tiny amount of power flow, depending on how close $(f)'$ and $(V_{dc})'$ are. This outcome is again correctly determined by (4-45), whose value is small and polarity depends on the relative size of $(f)'$ and $(V_{dc})'$.

(d) $(V_{dc})' \approx (f)'<0$: This scenario means that both the DC and AC sub-grids are overloaded and eager to absorb power from the interfacing converter. Therefore, the correct response expected from the interface should either be no or only tiny amount of power flow, depending on the difference between $(f)'$ and $(V_{dc})'$. Similarly, this outcome is again correctly determined by (4-45), whose value is small and polarity depends on the relative size of $(f)'$ and $(V_{dc})'$.

The principle of GPS has been explained in detail above. Based on GPS control, the relevant control implementation applied to the IC is established in the following sub-section.

4.4.2. Control structure of interlinking converter

According to the above illustration of GPS mechanism, the control objective of the IC is to track the power command determined by GPS principle. The relevant control implementation is shown in Figure 4.20, where measurements are marked in red color. The AC and DC bus voltages are first sensed. The former is fed into a phase lock loop (PLL) for capturing the system frequency, which is then normalized by (4-40). The same process is applied to V_{dc} in order to obtain $(V_{dc})'$. The normalized AC side frequency $(f)'$ and DC side voltage $(V_{dc})'$ are subsequently used to determine the active power command P_{IC}^{*} by (4-45).

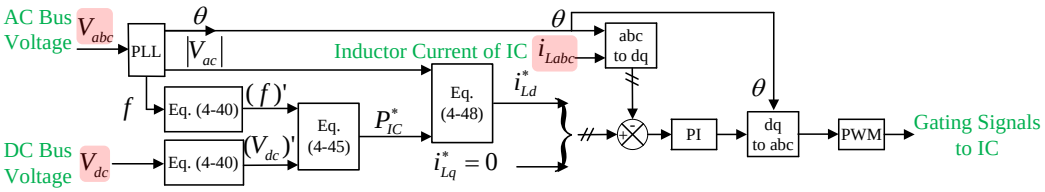

Figure 4.20. Control block diagram of interfacing converter.

The reactive power command is set as Q_2^{*}=0 since the IC is configured to deal with zero reactive power exchanged between itself and AC sub-grid in this research work. By determining the active and reactive power command, the complex current command for tracking by the IC can therefore be calculated as

$$I_{Ldq}^{*}=I_{Ld}^{*}+jI_{Lq}^{*}=\frac{2}{3}\frac{(P_{IC}^{*}+jQ_{IC}^{*})}{|V_{ac}|} \tag{3-64}$$

The tracking of the calculated complex current command here is enforced by two PI controllers in the synchronous frame as shown in Figure 4.20.

The tuning of the PI gains for the two fast inner current regulators can be done in MATLAB after setting the desired closed-loop bandwidth to be a fifth of the switching frequency or lower. The next step is to design the GPS controller which is also a PI regulator. Its proportional gain can be determined by first defining an acceptable error band ε_B for the two normalized variables. For error greater than ε_B during the initial

transient, the IC is designed to transfer its maximum active power $P_{IC,max}$ between the sub-grids to rapidly bring down the transient error. The proportional gain acting on the initial transient error can then be tuned as $k_p=2P_{IC,max} / \varepsilon_{B,}$ where the factor of 2 is for accounting bidirectional active power transfer. The transient error eventually approaches to zero because of the integral term of GPS controller. Its corresponding integral gain is set as $k_i=1000$ to make it slower than the inner current regulator. Moreover, a saturator is often placed after this GPS controller to limit the power flow on the IC. GPS operation mode is hereby realized by stable and accurate tracking.

4.5. Simulation Results

For preliminary verification, the proposed GPS control for active power sharing throughout entire hybrid AC/DC microgrid has been simulated with the autonomous hybrid microgrid drawn in Figure 4.21. The power sharing among parallel DGs in any single microgrid is not tested since the emphasis of this research work is to verify the proposed GPS control scheme. Instead, parallel DG units dispersed in AC or DC microgrid are represented by an equivalent DG unit with the combined droop characteristics as expressed in (4-35) and (4-37), respectively.

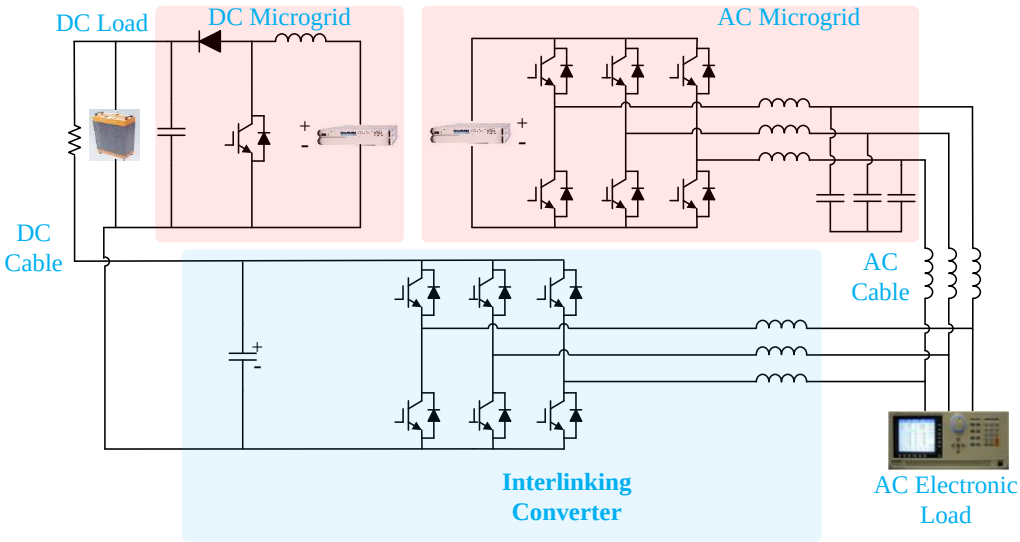

Figure 4.21. Test bed of hybrid AC/DC microgrid for global power sharing verifications in both simulation and experiment.

Table 4.3. System parameters for both simulation and experiment.

Unit	Parameters	Simulation	Experiment
AC Sub-grid	f	50±1Hz	50±1Hz
	$\lvert V_{ac}\rvert$	310±10V	80±10V
	$P_{ac\_1}^{nom}$	5kW	1kW
	$Q_{ac\_1}^{nom}$	3kVAr	1kVAr
DC Sub-grid	V_{dc}	700±20V	300±15V
	$P_{dc\_1}^{nom}$	6kW	1.2kW
GPS PI Controller	k_i	20000	20000
	k_p	1000	1000

System parameters for both simulation and experiment are listed in Table 4.3. For simulation executions, the ratings of AC source is 5kW over a frequency range of (49Hz, 51Hz), and 3kVAr over an AC voltage range of (300V, 320V). The corresponding values for the DC microgrid are 6kW over a DC voltage range of (680V, 720V). Connecting them is a six-switch half-bridge DC-AC converter serving as the IC. It is rated at 6kW and 3kVAr in total, allowing full active power exchange between two sub-grids and reactive power exchange between AC sub-grid and the IC. Four scenarios with respect to different loading conditions in both sub-grids are tested and the simulation results are as shown in Figure 4.22. Four scenarios are organized as follows.

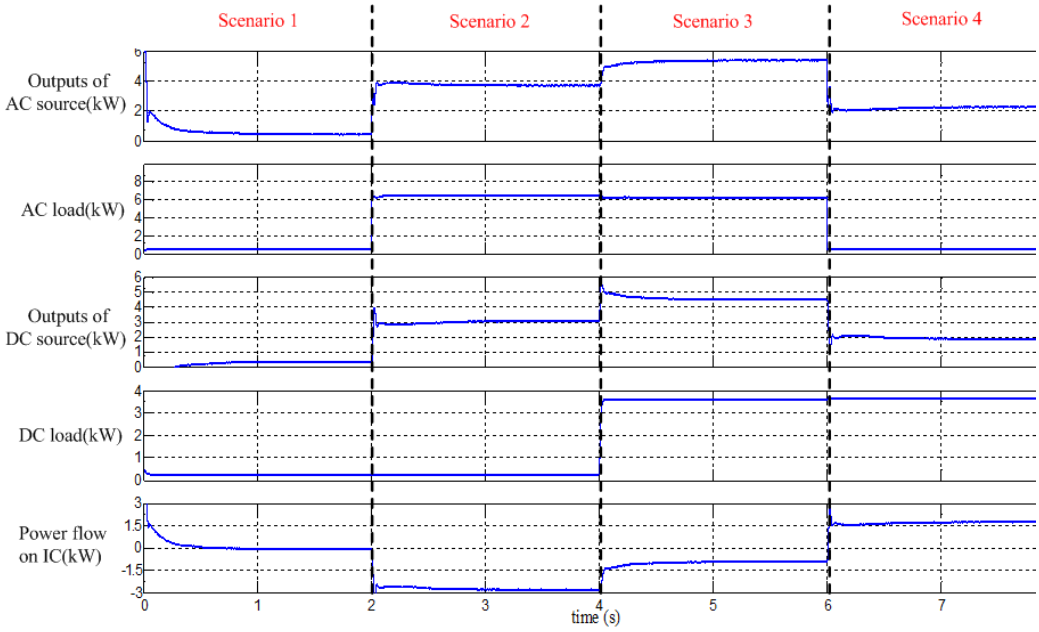

Figure 4.22. Simulation results of the GPS controlled hybrid microgrid.

1) Scenario 1: light load in both sub-grids

The first event is related to light loading conditions in both sub-grids before t=2s. The load in AC and DC sides are read as 0.27kW and 0.52kW, respectively, which can be separately observed from the 2nd and 4th plots of Figure 4.22. The output power of DG in AC sub-grid is read as 0.35kW as drawn in the 1st plot of Figure 4.22, while source output from DC side is about 0.46kW as plotted in the 3rd plot of Figure 4.22. For the power generated from AC source, 0.27kW/0.35kW is consumed by the local AC load, while the rest 0.08kW is enforced to be transferred to DC sub-grid through the interlinking converter under GPS control. This is reflected by the power flow in the interlinking converter, whose power flowing is read as -0.07kW from the 5th plot of Figure 4.22. The negative sign indicates that the direction of power flow is from AC to DC sub-grid. The slight difference between the power exchanged from AC source to DC sub-grid and the power flow in the interlinking converter is due to the losses due to the switching action and transmission line. Although a small amount of power is exchanged between two sub-grids, the effectiveness of global power sharing can still be verified by the ratio from AC to DC output (0.35kW/0.46kW), which is approximate proportional to their associated nominal values (5kW/6kW).

2) Scenario 2: light load in AC sub-grid and heavy load in DC sub-grid

The DC load step changes to 6.48kW at t=2s. The consumed power by the DC load becomes extremely heavy and exceeds the rating of the DC source. In this instance, the DC sub-grid will collapse if no power is pumped from AC sub-grid. This situation will not happen in the GPS-controlled hybrid system as 2.8kW surplus power is pumped from the AC sub-grid, supplying the overloaded DC load. By doing so, the AC source is now generating 3.05kW, 0.27kW/3.05kW is consumed by local AC load and the rest is transferred to the DC sub-grid. The output of DC source is about 3.7kW, which means overloading operation for DC source is automatically avoided by GPS control. Again, the accuracy of global power sharing can be verified by the ratio from AC to DC output (3.05kW/3.7kW), which is quite close to the ration of their associated nominal values (5kW/6kW).

3) Scenario 3: heavy load in both sub-grids

The AC load subsequently changes from 0.27kW to 3.6kW at t=4s. The loads in both sub-grids become extremely heavy. It can be observed from Figure 4.22 that about

0.9kW power is transferred from AC sub-grid, supplying the overloaded DC load in order to avoid collapse in the DC sub-grid. By doing so, the AC source is now generating 4.5kW, 3.6kW/4.5kW is consumed by the local AC load and the rest amount is transferred to the DC sub-grid. The output of the DC source is increased to 5.4kW, which results in a further voltage drop in DC bus. The further voltage drop in DC bus cause a slight change in the DC load, which can be read as 6.3kW. Again, the accuracy of global power sharing can be verified by the ratio from AC to DC output (4.5kW/5.4kW), which is quite close to the ration of their associated nominal values (5kW/6kW).

Table 4.4. Power flows of system components for different scenarios in simulation.

Scenarios	System Components	Power Flows (kW)
1 Light DC load & Light AC load	DC load	0.52
	AC load	0.27
	DC source	0.46
	AC source	0.35
	Interfacing converter	-0.07
2 Heavy DC load & Light AC load	DC load	6.48
	AC load	0.27
	DC source	3.7
	AC source	3.05
	Interfacing converter	-2.8
3 Heavy DC load & Heavy AC load	DC load	6.3
	AC load	3.6
	DC source	5.4
	AC source	4.5
	Interfacing converter	-0.9
4 Light DC load & Heavy AC load	DC load	0.5
	AC load	3.62
	DC source	2.25
	AC source	1.87
	Interfacing converter	1.74

4) Scenario 4: heavy load in AC sub-grid and light load in DC sub-grid

A step-down change finally happens in the DC load, whose value can be read as changed from 6.3kW to 0.5kW at t=6s. The output of the DC source is now 2.25kW, 0.5kW/2.25kW is consumed by the local DC load and the rest is transferred to the AC sub-grid. Note that the direction of power flow in the interlinking converter is reversed. This can be indicated from the reversed sign of power flow. Referring to the AC load,

1.87kW/3,62kW is supplied by local AC source, while the rest is supplied by the power transferred from DC side. Again, the accuracy of global power sharing can be verified by the ratio from AC to DC output (1.87kW/2.25kW), which is quite close to the ration of their associated nominal values (5kW/6kW).

Given that the vague readability of the power values in Figure 4.22, the relevant power values in different scenarios are listed in Table 4.4 for transparency in simulation results.

4.6. Experiment Verifications

For verifying the practicality of the proposed scheme, a scaled-down hybrid system based on the layout in Figure 4.21 is built in the laboratory. As understood from the above simulated plots, a large amount of waveforms is needed to be captured, which in practice might not be possible because of the limited channels of digital scopes. Therefore, the calculated output power of VSI and AC system frequency are plotted in DSpace/Controldesk. The other variables for observation are captured in two sets of oscilloscopes.

For experiment implementation, the AC sub-grid is rated at 1kW over a frequency range of (49Hz, 51Hz). The corresponding values for the DC microgrid are 1.2kW over a DC voltage range of (285V, 315V). Two transient events in terms of different directions of power flow on IC are carried out as follows.

1) Power flow from AC to DC sub-grid

Initial state (before t=1s)：

The loads in AC and DC sub-grids are initially set as 280W and 400W as shown in Figure 4.33(c)-C5 and Figure 4.33(d)-C6, respectively, while sources in AC and DC sub-grids are generating approximate 300W and 410W as shown in Figure 4.33(a) and Figure 4.33(d)-C5, respectively. The AC side frequency can be read as 50.3Hz from Figure 4.33(b) and DC bus voltage is read about 305V from Figure 4.33(d)-C4. Since the normalized AC side frequency and DC bus voltage are quite close, a very small amount of power is flowing through the interlinking converter according to the GPS

control algorithm. This can be reflected by the plot in Figure 4.33(d)-C3, where nearly zero 1-phase current of interlinking converter are captured.

Final state (after t=1s):

A step-up change happens in DC load at around t=1s, the power consumed by DC load increases to 1000W. This sudden increase causes severe voltage drop in the DC bus voltage (to see Figure 4.33(d)-C4) since the output power of DC source immediately follow-up the DC load change. In the meantime, the difference between normalized AC side frequency and DC bus voltage becomes larger due to the severe voltage drop in DC bus voltage. This automatically results in a higher power transferred from the AC to DC sub-grid. The power exchanged between the two sub-grids is therefore increased to about 300W (to see in Figure 4.33(d)-C7). After the transient, AC source outputs about 600W (to see in Figure 4.33(a)), 280W/600W is consumed by the local AC load and the rest is transferred to the DC sub-grid, supplying DC load. GPS is also verified from the ratio of the outputs of AC and DC sources (600W/700W), which is quite close to the ratio under their nominal values (1000W/1200W).

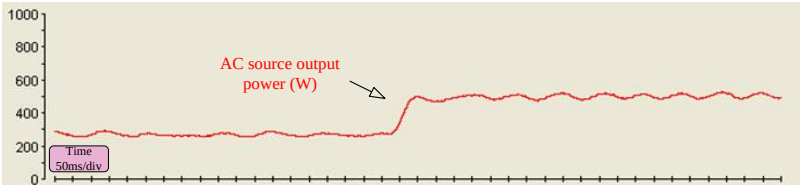

(a)

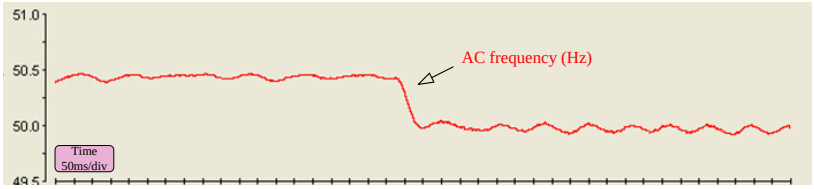

(b)

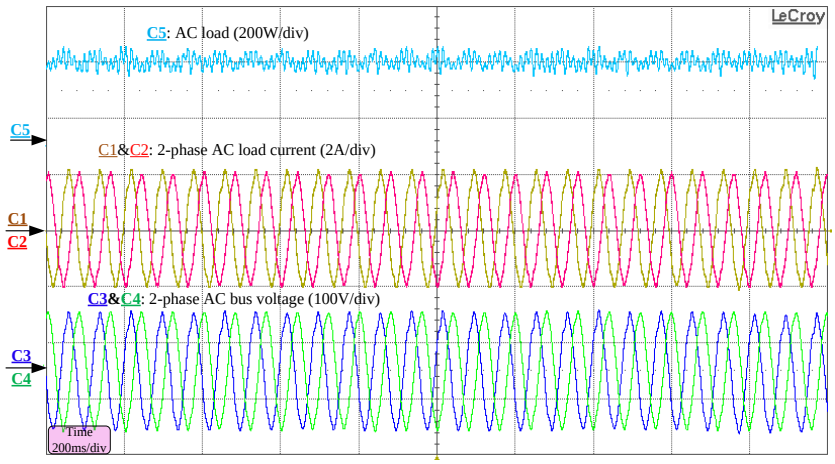

(c)

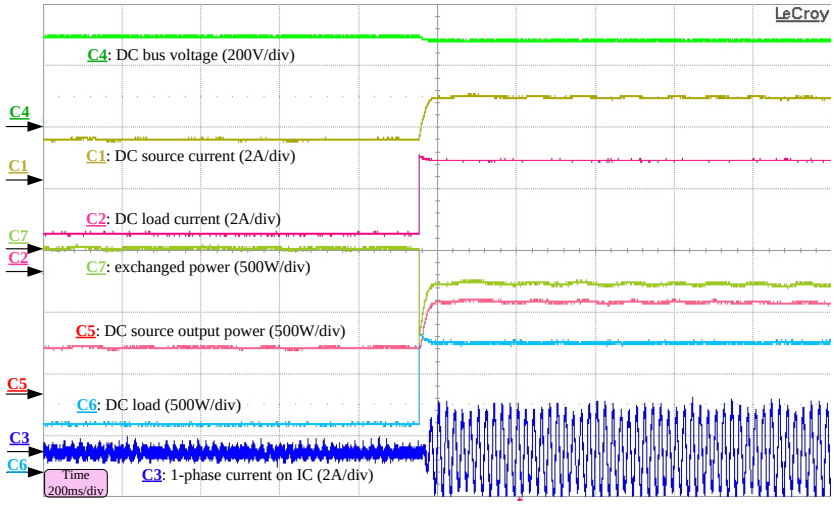

(d)

Figure 4.23. Experimental AC and DC waveforms in transient event 1: (a) output power of AC source; (b) AC system frequency; (c) AC load; (d) DC source output, DC load and power flow on interlinking converter.

2) Power flow from AC to DC sub-grid

Initial state (before t=1s)：

In this case, the loads in the AC and DC sub-grids are initially configured as 350W and 120W as shown in Figure 4.34(c)-C5 and Figure 4.34(d)-C6, respectively, while the sources in AC and DC sub-grids are generating approximately 220W and 280W as shown in Figure 4.33(a) and Figure 4.33(d)-C5, respectively. The AC side frequency can be read as 50.65Hz from Figure 4.33(b) and the DC bus voltage is read about 312V from Figure 4.33(d)-C4. Since the normalized AC side frequency is slightly less

than normalized DC bus, a very small amount of power (150W) is flowing from the DC to AC sub-grid according to the GPS control algorithm. This can be reflected by the plot in Figure 4.33(d)-C7, whose positive sign denotes forward DC-AC power flow. Although a small amount of power is generated from sources in both sub-grids, the effectiveness of GPS can also be verified from the ratio of the outputs of AC and DC sources (220W/280W), which is quite close to the ratio under their nominal values (1000W/1200W). Note that the errors between those two ratios are mainly due to the power losses due to the switching actions and transmission line.

Final state (after t=1s):

At around t=1s, a step-up change happens in the AC load, the power consumed by the AC load increases to 800W as explicated in Figure 4.33(c)-C5. This sudden increase causes a further frequency drop in AC system (to see Figure 4.33(b)) since the output power of AC source immediately follow-up with the AC load increase. In the meantime, the difference between the normalized AC side frequency and DC bus voltage become even larger due to the further voltage drop in the AC system frequency. This would automatically results in a higher power transferred from the DC to AC sub-grid. The power exchanged between the two sub-grids is therefore increased to about 360W (to see in Figure 4.33(d)-C7).

After the transient, the AC source output can be read as 450W (to see in Figure 4.33(a)), while the output of DC source is 500W. For this amount of power from DC source, 120W/500W is consumed by the local DC load and the rest is transferred to the AC sub-grid, supplying AC load. After the transients, the effectiveness of GPS is alsocollectively verified by the ratio of the outputs of AC and DC sources (450W/500W), which is quite close to the ratio under their nominal values (1000W/1200W).

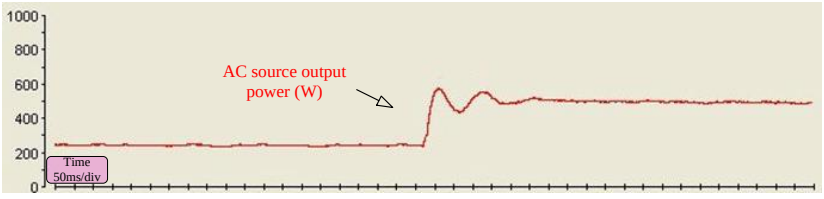

(a)

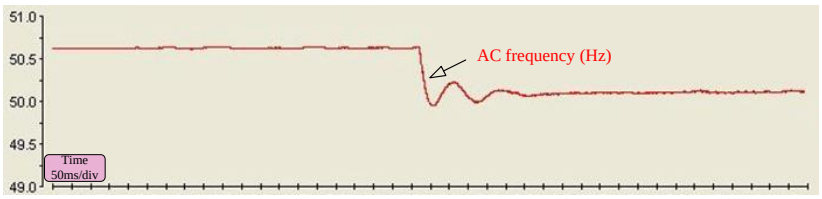

(b)

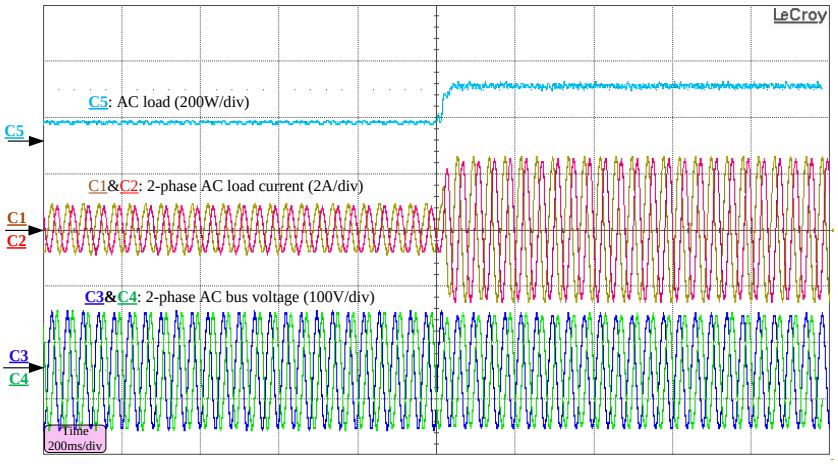

(c)

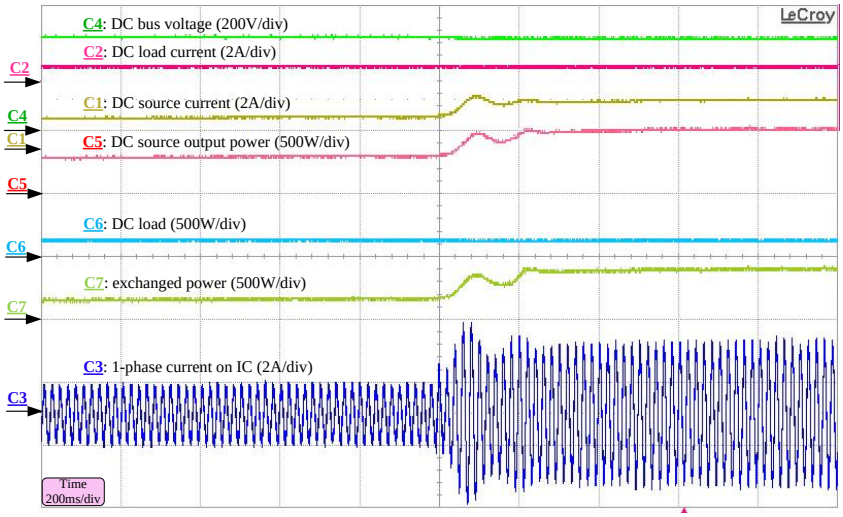

(d)

Figure 4.24. Experimental AC and DC waveforms in transient event 2: (a) output power of AC source; (b) AC system frequency; (c) AC load; (d) DC source output, DC load and power flow on interlinking converter.

For completeness experimental illustrations, the power flows in different states for two cases are listed in Table 4.5. The experiment results shows that, through normalization AC frequency and DC bus voltage, the proposed GPS control scheme can automatically manage the power balance within each sub-grid as well as the power exchange between two sub-grids.

Table 4.5. Power flows of system components for different scenarios in experiment.

Scenarios	Initial state		Final state	
	System Components	Power Flows (W)	System Components	Power Flows (W)
Power flow direction on IC: AC microgrid ↓ DC microgrid	DC load	400	DC load	1000
	AC load	280	AC load	280
	DC source	410	DC source	700
	AC source	300	AC source	600
	Interfacing converter	0	Interfacing converter	-300
Power flow direction on IC: DC microgrid ↓ AC microgrid	DC load	120	DC load	120
	AC load	350	AC load	800
	DC source	280	DC source	500
	AC source	220	AC source	450
	Interfacing converter	150	Interfacing converter	360

4.7. Conclusions

This chapter presents a GPS control for power distributed in an autonomous hybrid AC/DC microgrid. Droop control and its improved variants for DGs in individual AC or DC sub-grid have been reviewed first. The power sharing among DGs in single microgrid is then established. A normalization technique is adopted to normalize information on both sides of the IC before an appropriate power flow command is well tuned. With the normalization method, the principle of GPS is subsequently interpreted by means of mathematical and graphical methods. Different operation scenarios have been preliminarily verified in simulations and eventually tested in experimental results in order to verify the effectiveness of proposed control scheme. The rule of GPS provides an effective fully decentralized control scheme for reliable autonomous operation of the hybrid system.

Chapter 5 Distributed Control for Autonomous Operation of Hybrid AC/DC/DS Microgrids

5.1. Introduction

Global power sharing (GPS) for autonomous operation of hybrid AC/DC microgrids has been introduced in the last chapter without considering the operations of distributed storages (DSs). In fact, the hybrid microgrid can hardly be fully autonomous without DSs for energy buffering, power balancing and fault riding-through if the impacts of variable random loads at the demand end and intermittent renewable sources at the supply end are considered. With the consideration of integrating DSs into hybrid AC/DC system, a three-bus AC/DC/DS hybrid infrastructure is proposed in this chapter. In this layout, DGs and DSs with the same type are placed together in the relevant AC, DC or DS bus in order to avoid the complexity of power management and enforce coincident control scheme to DGs and DSs. For managing the power flow and maintaining reliable operation of such a complex hybrid system, a distributed control including a fully decentralized control for independent DG (or DS) control and a multilevel power exchange control for optimal fashion improvement will be elaborated in the following sections.

5.2. Proposed Hybrid AC/DC/DS Structure

The storages which are configured to behave in different manners for specific microgrid applications have been investigated in many publications [16, 61, 83, 86]. In [16, 61], the storage units are controlled as a voltage source in a DC microgrid, coordinately regulating the DC bus voltage with the renewable and conventional sources. On the other hand, the storages are capable of serving as a current source in an AC microgrid, absorbing/releasing the surplus power from/to the generation supply/load demand in an automated manner [83, 86]. In this sense, different control schemes for DS will undoubtedly increase the complexity of power management in hybrid AC/DC microgrid with storages in spite of DS locations in the AC or DC sub-grid. Therefore, fulfilling the requirement of “plug-and-play” is getting difficult since all DS dispersed in the hybrid AC/DC system are not controlled in a coincident way.

To avoid the complexity of power management and enforce coincident control scheme to DS, a hybrid microgrid scenario with three-bus including the AC, DC, and DS buses is proposed as shown in Figure 5.1. In this layout, the DS units are intensively tied to the DS bus whilst the DGs are connected to associated AC or DC bus according to their electrical properties and geographical locations. In this sense, sources, storages and loads of the same type are placed together to avoid control complexity and minimize the losses in multi-stage power conversions. With such a hybrid system established, the companied challenges are to find applicable interconnections to link up three networks and develop proper control scheme to maintain the power balance within individual network and manage the power exchange amongst three networks.

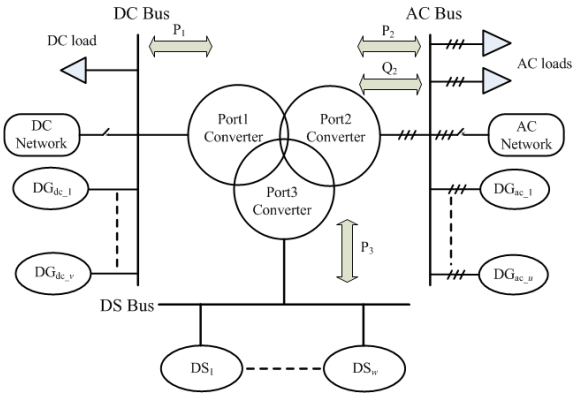

Figure 5.1. Overview of the architecture of hybrid AC/DC/DS microgrid.

For detailed implementation, the overall system configuration of the proposed hybrid AC/DC/DS system is shown in Figure 5.2. It comprises of an AC bus, a DC bus, and a DS bus. As shown in Figure 5.2, *u* and *v* DG units are connected to the AC and DC buses, respectively. The AC and DC buses are interconnected by a two-stage interlinking converter (IC) whose intermediate DC-link is treated as the DS bus. The DS bus is connected by *w* DS units. An intelligent transfer switch is tying the AC network to the grid, allowing the entire system to operate in both grid-connected and islanded modes. In terms of active power dispatch, a DG unit can be categorized as a dispatchable or non-dispatchable unit [87]. Examples of dispatchable DGs include micro-turbines and fuel cells, which are in charge of regulating system voltage and frequency during islanded operations by means of producing controlled active power on demand. On the contrary, non-dispatchable DGs like solar and wind generations whose output are solely dependent on weather conditions usually operate at their maximum power points in

grid-connection mode. In spite of this, the renewable energy-based non-dispachable DGs can be also forced to appear as dispachable units in autonomous situation, in which non-dispachable DGs are capable of regulating the system voltage and keeping supply-demand power balance at the cost of discarding maximum power harness. Considering the emphasis of this research work, a distributed control strategy is developed for dispachable DGs, while non- dispachable DGs can be viewed as the negative load or adjusted to behave like dispachable DGs.

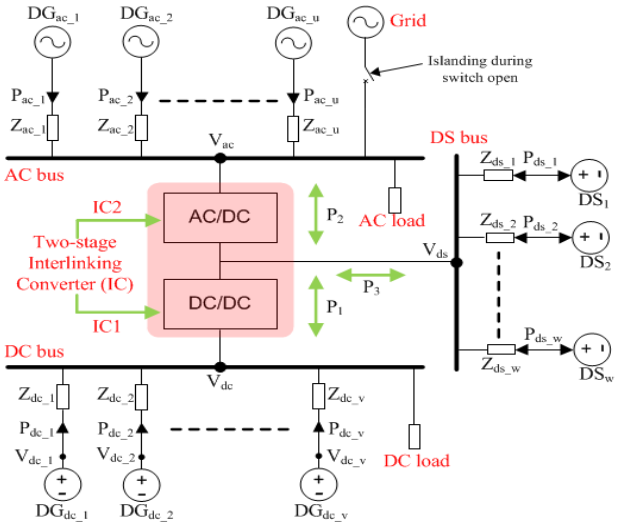

Figure 5.2. System configuration of the proposed hybrid AC/DC/DS microgrid.

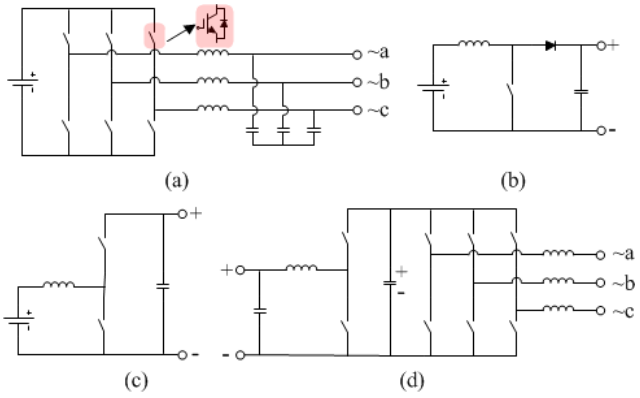

Figure 5.3. Circuit diagrams of: (a) DG unit in AC network; (b) DG unit in DC network; (c) DS unit in DS network; (d) two-stage interlinking converter (IC) interconnecting AC and DC networks.

The specific circuit diagrams of each component within the AC/DC/DS hybrid system are drawn in Figure 5.3, where (a) is a DC/AC inverter forming a DG unit in the AC network, (b) is a DC/DC booster forming a DG unit in the DC network, (c) is a

bidirectional DC/DC converter representing a DS unit in the DS network, and (d) is the two-stage IC, including both bidirectional DC/DC (IC1) and DC/AC converters (IC2). The IC ties three networks together, allowing bidirectional power flow at all buses. The difficulty is then to develop a distributed coordination control for maintaining power balance in each individual network and managing power exchange among three networks. This is realized by the proposed distributed control illustrated in detail as follows.

5.3. Proposed Distributed Control

So far, reliable and economical operations of such a complex three-port AC/DC/DS system usually involve multi-layer supervision system and advanced energy management algorithm, which rely heavily on a high-speed communication path for coordination control of fast-switched converters [88-92]. This may obviously degrade the system redundancy in addition to result in system outage during the malfunction in the communication carrier. Decentralized control promises a solution to enhance the system redundancy since each unit is controlled using local measurements without communication links [93]. From this viewpoint, it provides an alternative way of riding through communication multifunction.

As introduced in previous chapters, the droop control method has been well-prove to implement decentralized control to DGs within microgrid. Authors in [54] propose a three-level hierarchical control, in which, the primary control for power sharing, the secondary control for frequency/voltage recovery, and the tertiary control for power dispatching are applied to individual AC or DC microgrids so as to imitate the primary frequency/voltage regulation, secondary frequency/voltage recovery, and power dispatch control in conventional power system, respectively. However, only the individual network's power balance is decentralized in the primary control by using the droop control method. The fully decentralized control for the entire hybrid system operation, including power balance within individual networks and power exchange amongst AC and DC networks, is not taken into account.

The GPS control described in the last chapter offers a alternative way to realize a fully decentralized controlled hybrid AC/DC system. However, the unconstrained GPS

control is implemented consistently, which results in additional power loss due to the unnecessary power exchange behaviors. Moreover, by modifying the interconnection topology from a single power stage to the dual, the proposed decentralized control in [83] is also extended to include energy storage within the interconnection converters. However, power sharing amongst multiple DSs with regard to relevant storage capacity and state-of-charge (SoC) is still not considered.

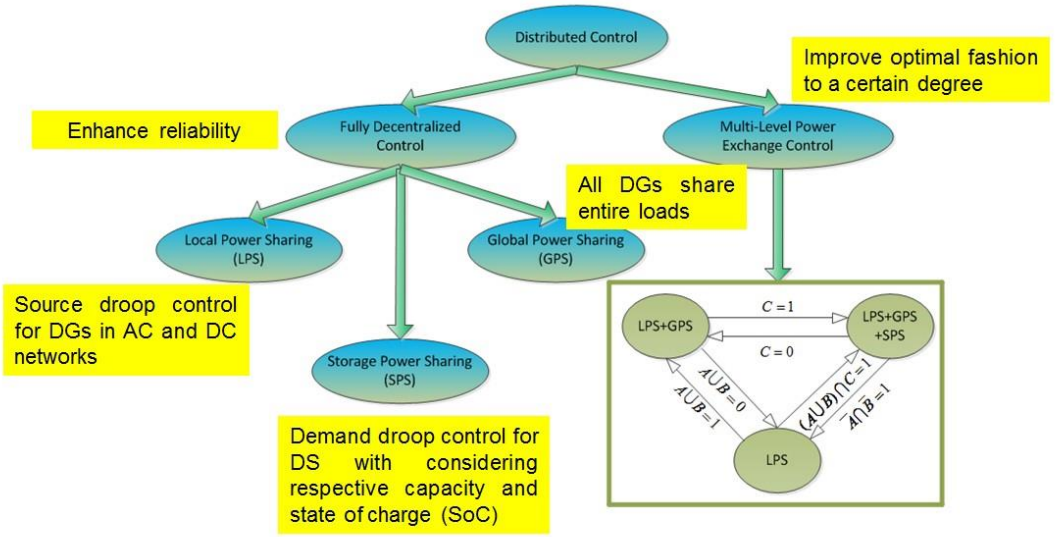

Figure 5.4. Illustration of the proposed distributed control for hybrid AC/DC/DS microgrid.

To cope with the aforementioned problems, a distributed control strategy for autonomous operation of three-bus AC/DC/DS hybrid microgrid is proposed in this chapter for enabling large-scale integration of DGs and DSs into future networks. The proposed distributed control can be illustrated with the help of Figure 5.4. It includes a fully decentralized control and a multi-level power exchange control. For the former, it comprises of: (1) source droop control for local power sharing (LPS) within individual AC or DC network; (2) GPS control for global power sharing throughout entire AC and DC networks; (3) demand droop control for storage power sharing (SPS) among DS units. For the multi-level power exchange control, it is employed to schedule the activation sequences among LPS, GPS and SPS so as to restrain unnecessary GPS behaviors and reduce the usage of DS. Since LPS and GPS for DGs and the interlinking converter (IC) are well explained in Chapter 4, it is not introduced in this chapter. Note

that for two-stage IC in this system, GPS control is implemented on the bidirectional DC/AC converter (IC2 as shown in Figure 5.2), while the bidirectional DC/DC converter (IC1 as shown in Figure 5.2) is responsible for maintaining the intermediate DC-link voltage.

5.4. Storage Power Sharing for DS Units

By realizing LPS and GPS in previous chapter, global supply-demand conditions (GSDC) throughout two sub-networks are linkup. AC and DC networks are expected to operate around the nominal f/V_{dc}. Higher/lower f (or V_{dc}) indicates relatively lower/higher loading condition with respect to entire generation capacities. This would lead to unexpected f/V_{dc} deviations which are inherent accompaniments with LPS. To limit those deviations, the operation criteria of DS units can be clarified by monitoring GSDC as follows:

a) Charging mode: DS units would absorb surplus power from DGs if total loads are light, and $0<(f)'=(V_{dc})'<1$.
b) Discharging mode: DS units would releases power to system if total loads are heavy and $-1<(f)'=(V_{dc})'<0$.

The GSDC is measured by the average loading condition of AC and DC networks as:

$$\zeta=\frac{(f)'+(V_{dc})'}{2} \tag{3-65}$$

Similar to DC voltage and AC frequency, who perform the role for ensure LPS among DGs by source droop control, the index ζ can be inferred to play the same role for ensuring SPS in DS network by demand droop control as:

$$\zeta=b_z P_{ds\_z} \tag{3-66}$$

where bipolar variable P_{ds_z} is absorbed/released power of z^{th} DS unit, its positive value denotes discharge and vice versa. b_z is the negatively droop coefficient of z^{th} DS as

shown in Figure 5.5, and it is designed as

$$b_z = 1 / P_{ds\_z}^{max} \tag{3-67}$$

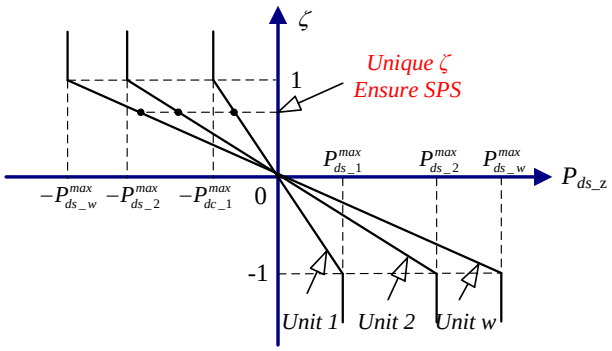

Figure 5.5. Capacity-based demand droop for SPS among DSs in DS network.

Based on the equal ζ, all DSs proportionally absorb/release power based on their capacities,

$$\frac{P_{ds\_1}}{P_{ds\_1}^{max}} = \frac{P_{ds\_2}}{P_{ds\_2}^{max}} = \cdots = \frac{P_{ds\_w}}{P_{ds\_w}^{max}} = \xi \tag{3-68}$$

Upon establishment of demand droop controlled DS units, the differences between source droop control and demand droop control can be summarized as follows:

a) For conventional source droop control, it generally droops the AC system frequency or DC bus voltage by the measured output powers of DGs. The DG therefore essentially performs in voltage controlled mode.
b) For demand droop control, it droops the absorb/release powers of DSs by measured GSDC. In fact, it is the reverse process of source droop control. The demand droop controlled DS therefore can be viewed as a current controlled source.

In practice, storage capacity and charging rate vary with state of charge (SoC) in system operation. Considering this effect in SPS, a SoC-based droop coefficient $(b_z)'$ is

developed as [94]

$$(b_z)'=\begin{cases}\left(\dfrac{SoC_z}{SoC_z^*}\right)^{\lambda} b_z, & for \quad P_{ds\_z}<0\\ \left(\dfrac{SoC_z^*}{SoC_z}\right)^{\lambda} b_z, & for \quad P_{ds\_z}>0\end{cases} \tag{3-69}$$

where SoC_z and SoC_z^* are instant and reference SoC respectively, λ is weight of SoC compared to DS capacity. Larger λ means that SoC have higher weight in dominating power sharing mechanism among DS units. In this thesis, λ is selected as 1. SoC_z^* is defined as

$$SoC_z^* = \frac{(SoC_z^{max} + SoC_z^{min})}{2} \tag{3-70}$$

where SoC_z^{max} and SoC_z^{min} are maximum and minimum SoC limits. It is noted that $(b_z)'=b_z$ when $SoC_z = SoC_z^*$. The $P_{ds\_z}^{max}$ in (5-3) should therefore be corresponding to the rated power $P_{ds\_z}^*$ when $SoC_z = SoC_z^*$. The modified droop equation with respect to storages instant SoC eventually becomes,

$$\zeta = (b_z)'P_{ds\_z} \tag{3-71}$$

The principle of SoC-based demand droop control on managing SPS is described with the help of Figure 5.6 as follows.

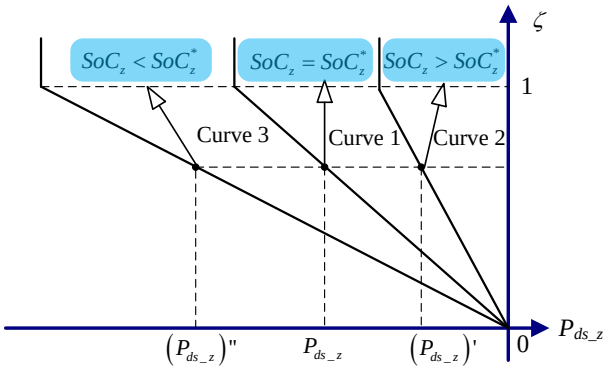

(a)

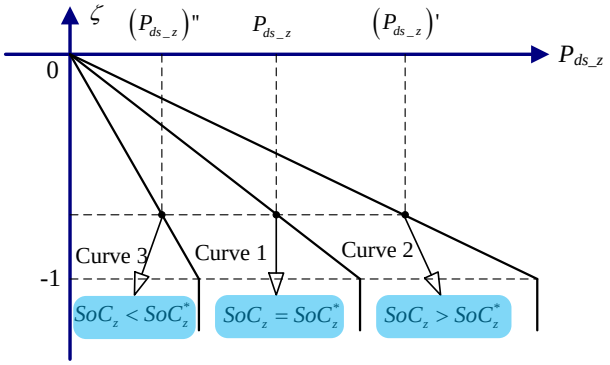

(b)

Figure 5.6. Illustration of SoC-based demand droop control on managing SPS during (a) charging mode; (b) discharging mode.

a) Charging mode ($P_{ds\_z} < 0$)

SoC-based demand droop characteristics of z^{th} DS unit in charging mode is drawn in Figure 5.6(a). Curve 1, 2 and 3 are corresponding to droop curves when $SoC_z = SoC_z^*$, $SoC_z > SoC_z^*$, and $SoC_z < SoC_z^*$. When $SoC_z = SoC_z^*$, z^{th} DS unit would absorb P_{ds_z} to share the total surplus system power with other DS units. If $SoC_z > SoC_z^*$, the unit is controlled to absorb less power by changing the droop curve to trajectory 2 as explicated by $(P_{ds\_z})' < P_{ds\_z}$. On the contrast, this DS unit is expected to absorb more power if $SoC_z < SoC_z^*$. This is reflected on trajectory 3, where z^{th} DS unit is absorbing more power ($(P_{ds\_z})'' > P_{ds\_z}$) then it operates on trajectory 2.

b) Discharging mode ($P_{ds\_z} > 0$)

During discharge, the relevant droop characteristics are drawn in Figure 5.6(b). Curve 1, 2 and 3 are the relevant droop curves when $SoC_z = SoC_z^*$, $SoC_z > SoC_z^*$, and $SoC_z < SoC_z^*$. When $SoC_z = SoC_z^*$, z^{th} DS unit would release P_{ds_z} power to supply loads with other DS units. If $SoC_z > SoC_z^*$, this DS unit is expected to release more power. This can be enforced by changing the droop characteristics to curve 2 as explicated by $(P_{ds\_z})' > P_{ds\_z}$. On the contrast, this DS unit is expected to release less power if $SoC_z < SoC_z^*$. This is reflected on curve 3, where z^{th} DS unit is releasing less power ($(P_{ds\_z})'' < P_{ds\_z}$) then it

operates on curve 2.

By introducing SoC-based demand droop control, power sharing among storages can be realized according to their respective capacity and SoC.

5.5. Multi-level Power Exchange Control

Based on the three power sharing methods — LPS, GPS and SPS, the fully decentralized power management for the hybrid microgrid can be realized. Nevertheless, consistent operation of GPS and SPS under all operating conditions is not economic. On the one hand, unnecessary GPS operation will result in considerable power losses in the IC and cables when both the AC and DC sides are locally balanced. On the other hand, frequent charge/discharge of DSs with load variation under the SPS scheme may lead to obvious degradation of battery life. Therefore, a multi-level power exchange control scheme is proposed to restrain unnecessary GPS and SPS operations.

Under the proposed scheme, the tolerance band of the normalized f/V_{dc} is divided into three regions by two threshold values $|(\gamma)'|_g$ and $|(\gamma)'|_s$ for scheduling and prioritizing the activation sequences of LPS, GPS and SPS (γ denotes f or V_{dc}).

$$\begin{aligned} &Region\,1: \quad 0 < |(\gamma)'| \le |(\gamma)'|_g \\ &Region\,2: \quad |(\gamma)'|_g < |(\gamma)'| \le |(\gamma)'|_s \\ &Region\,3: \quad |(\gamma)'|_s < |(\gamma)'| < 1 \end{aligned} \tag{3-72}$$

a) In Region 1, power is locally balanced in both AC and DC sides under the system limits. The AC frequency and DC voltage are around their nominal values. Only LPS is executed in the AC and DC networks. GPS and SPS operations are not activated.
b) In Region 2, at least one of f or V_{dc} exceeds the threshold value $|(\gamma)'|_g$, which indicates large deviations in AC frequency or DC voltage. GPS is therefore activated to avoid too large deviation in any single network.
c) In Region 3, the frequency and voltage deviations are close to system limitation values, SPS operation is triggered to prevent the system from operating over/under

frequency/voltage.

By clarifying the schedule sequences of LPS, GPS and SPS, the multi-level power exchange control can be demonstrated as shown in Figure 5.7. Details on the logical operation of scheduling GPS and SPS are described below.

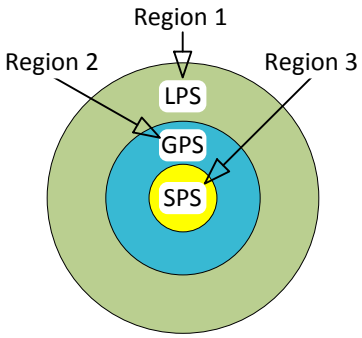

Figure 5.7. Illustration of multi-level power exchange control.

5.5.1. Scheduling of global power sharing (GPS) operation

The GPS should be triggered as long as $|(\gamma)'| > |(\gamma)'|_g$. However, the condition of disabling GPS is not as straightforward as $|(\gamma)'| \le |(\gamma)'|_g$ for some operating conditions, which may lead to malfunction of GPS disabling. For example, power flow under the condition of heavy AC and light DC loads is from DC to AC during LPS+GPS operation mode. In this case, the GPS should have been disabled when the normalized f or V_{dc} satisfy $|(f)'|=|(V_{dc})'| \le |(\gamma)'|_g$. After GPS is disabled, the large deviations $(f)'$ and $(V_{dc})'$ under LPS may lead to $|(\gamma)'| > |(\gamma)'|_g$ and GPS re-triggering. The system becomes unstable due to the switching between LPS mode and LPS+GPS mode.

Therefore $|(\gamma)'| \le |(\gamma)'|_g$ cannot be directly used as the consistent condition for GPS scheduling. A uniform condition is developed to schedule GPS. Based on frequency change Δ_f and voltage change $\Delta_{V_{dc}}$ when the system transfers from LPS to LPS+GPS, two condition events A and B are defined as

$$\text{Event A: } \left|(f+\Delta_f)'\right| > \left|(f)'\right|_g \tag{3-73}$$

$$\text{Event B: } \left|(V_{dc}-\Delta_{V_{dc}})'\right| > \left|(V_{dc})'\right|_g \tag{3-74}$$

where Δ_f and $\Delta_{V_{dc}}$ can be obtained from (4-35) and (4-37).

Before GPS is triggered, Δ_f and $\Delta_{V_{dc}}$ are zero because of no power exchange between two sub-networks (P_1=P_2=0). Events A and B become $\left|(f)'\right| > \left|(f)'\right|_g$ and $\left|(V_{dc})'\right| > \left|(V_{dc})'\right|_g$, which intuitively indicates that GPS will be triggered once $\left|(\gamma)'\right| > \left|(\gamma)'\right|_g$.

During LPS+GPS operation, $(f+\Delta_f)'$ and $(V_{dc}+\Delta_{V_{dc}})'$ are updated online. If both Event A and B become false, GPS operation can be disabled. The original GPS expression in (4-45) can thus be modified as

$$P_2 = \begin{cases} [(f)'-(V_{dc})'](k_p + k_i/s), & A \cup B = 1 \\ 0, & A \cup B = 0 \end{cases} \tag{3-75}$$

where $\cup$ is the logical "OR" operator.

5.5.2. Scheduling of storage power sharing (SPS) operation

Inferred from the scheduling of GPS, the scheduling criteria of SPS can be obtained by modifying (5-7) as

$$P_{ds\_z} = \begin{cases} \dfrac{\zeta}{(b_z)'}, & C = 1 \\ 0, & C = 0 \end{cases} \tag{3-76}$$

where $\left\{\left|0.5\left[(f+\Delta_f)'+(V_{dc}-\Delta_{V_{dc}})'\right]\right| > \left|(\gamma)'\right|_s\right\}$ is labeled as logical Event C. By

summarizing the scheduling principle of GPS and SPS, the logical relationships about mode change among LPS, GPS, and SPS is demonstrated in Figure 5.8.

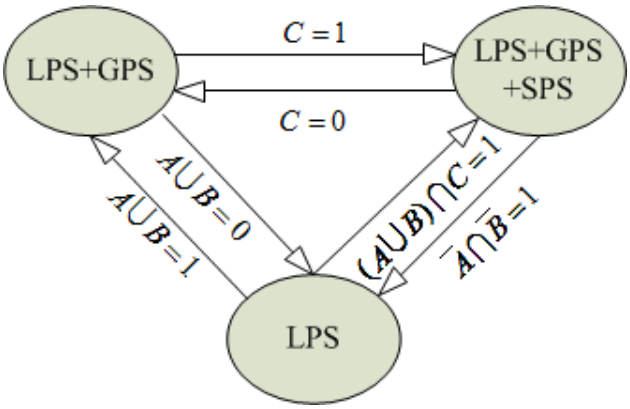

Figure 5.8. Conditions and associated mode switching of LPS, GPS, and SPS.

5.6. Simulation Results

For preliminary verification, Matlab/Simulink simulation is first executed with the proposed distributed control scheme applied to the hybrid AC/DC/DS microgrid prototype as shown in Figure 5.9. Since power sharing method in individual AC or DC network has been well-verified in the literature, LPS among parallel DGs is not considered in simulation and experiment. Therefore, only one DG unit is placed in each network as shown in Figure 5.9 in order to reduce complexity. Relevant system parameters for simulation and experiment verifications are both listed in Table 5.1. Five cases are first simulated as follows and the results are shown in Figure 5.10.

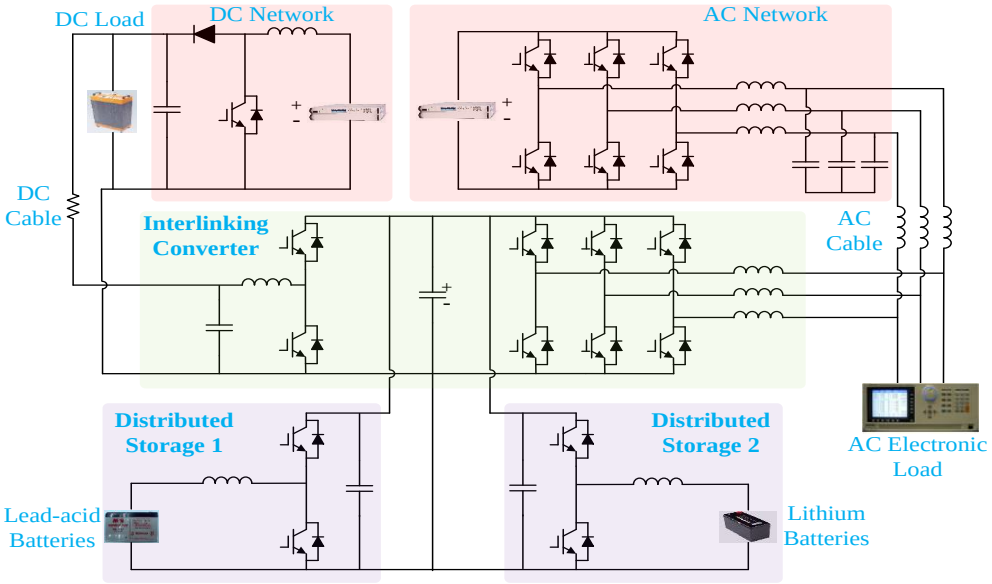

Figure 5.9. Test bed of the proposed hybrid AC/DC/DS system.

Table 5.1. System Parameters for Simulation and Experiment Verifications.

Unit	Parameters	Simulation	Experiment
AC Network	f	50Hz±2%	50Hz±2%
	$\lvert V_{\mathrm{ac}}\rvert$	310±10V	90±10V
	$P_{ac\_1}^{nom}$	6000W	1200W
	$Q_{ac\_1}^{max}$	3000W	1000W
	$\lvert(f)'\rvert_g$	0.2	0.2
	$\lvert(f)'\rvert_s$	0.6	0.8
DC Network	V_{dc}	380±20V	300±15V
	$P_{dc\_1}^{nom}$	5000W	1500W
	$\lvert(V_{\mathrm{dc}})'\rvert_g$	0.2	0.2
	$\lvert(V_{\mathrm{dc}})'\rvert_s$	0.6	0.8
DS Network	V_{ds_1}	300V	200V
	V_{ds_2}	200V	100V
	$P_{ds\_1}^{max}$ & $P_{ds\_1}^{min}$	±3000W	±1000W
	$P_{ds\_2}^{max}$ & $P_{ds\_2}^{min}$	±2000W	±800W
	SoC_1	30%	30%
	SoC_2	70%	70%
	SoC^*	50%	50%
Other	V_m	700V	400V

Case 1: The AC and DC loads are initially set to 2.87kW and 2.40kW respectively. $\lvert(f+\varepsilon_f)'\rvert$ and $\lvert(V_{dc}-\varepsilon_{V_{dc}})'\rvert$ are 0.05 and 0.04 respectively. Therefore Events A and B are not true. There is no power exchange among three networks. DGs in AC and DC

networks are now supplying 2.88kW and 2.43kW to their local loads, respectively.

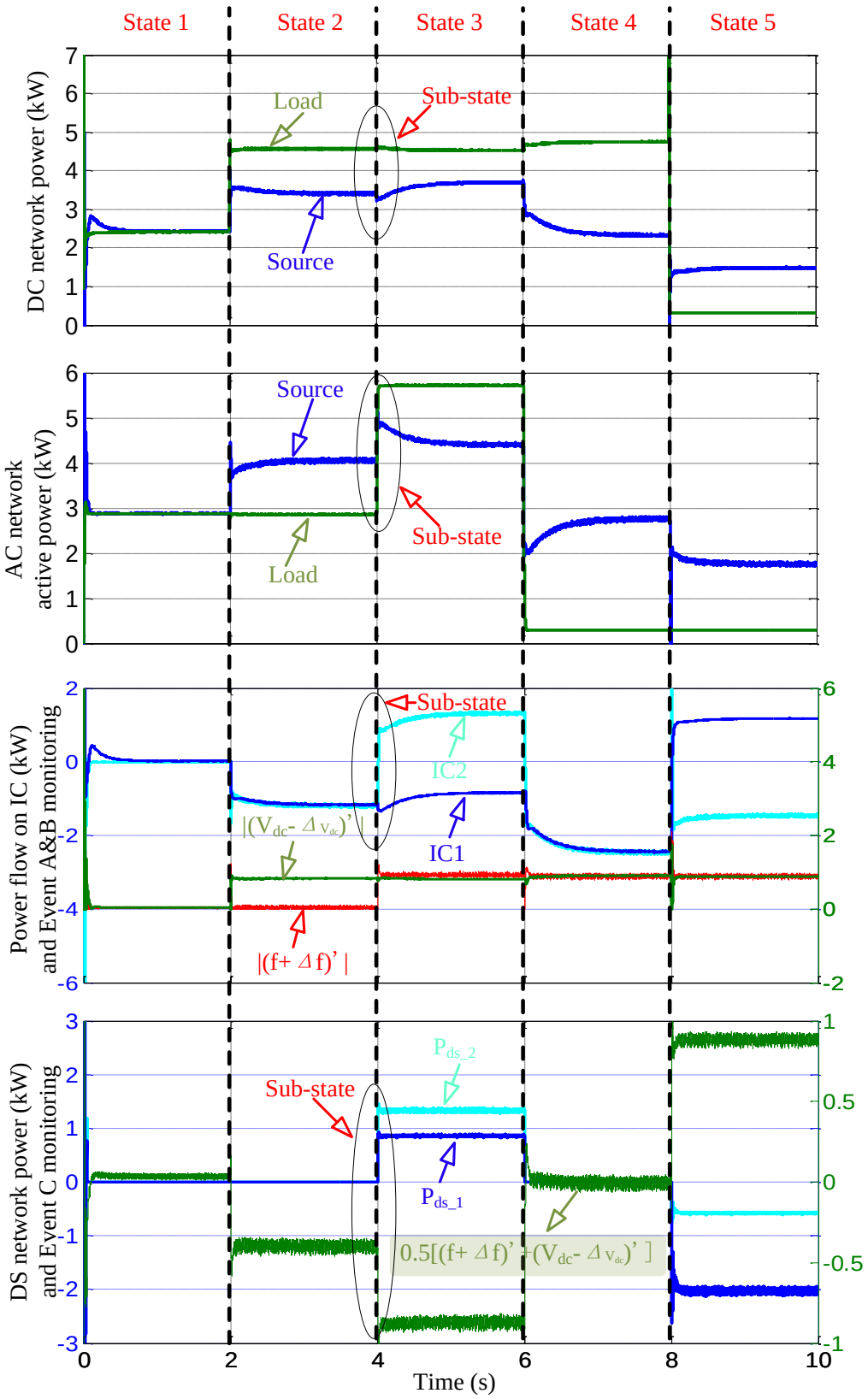

Figure 5.10. Simulated active power flows on source, storage and interlinking converters.

Case 2: When the DC load changes from 2.4kW to 4.57kW at t=2s, $\left|(V_{dc}-\varepsilon_{V_{dc}})'\right|$ is about 0.82. True Event B enables GPS operation. In GPS mode, AC source supplies 4.05kW. For this amount of power, 2.87 kW/4.05kW is for the AC load and the rest is transferred to supply the DC load. The DC source supplies the rest of the DC load which is around 3.41kW. It is obvious that the AC and DC sources can share the entire load in proportion to their ratings {6kW, 5kW}. Since Event C is false, there is no power exchange between DS and others.

Case 3: When the AC load suddenly changes from 2.87kW to 5.72kW at t=4s, both the AC and DC loads are heavy and $0.5\left[(f+\varepsilon_f)'+(V_{dc}-\varepsilon_{V_{dc}})'\right]$ is about -0.9. True Event C activates SPS. DS1 and DS2 generate 0.85kW and 1.33kW respectively. DS1 with a higher capacity generates less power than DS2. The reason is that the SoC of DS1 is lower than that of DS2 at this intant. The effect of SoC-based demand droop control for SPS is verified in this case. 0.85kW of the total power from DS network is transferred to the DC network and1.33kW is transferred to AC network. The AC and DC sources generate 4.40kW and 3.69kW respectively, in proportion to their power ratings.

Case 4: When the AC load changes from 5.72kW to 0.29kW at t=6s, the overall system loading condition is normal. $\left|(f+\varepsilon_f)'\right|$ and $\left|(V_{dc}-\varepsilon_{V_{dc}})'\right|$ are 0.9 and -0.91 respectively. Both Event A and B remain true. The system is in GPS operation mode. AC and DC sources are now generating 2.75kW and 2.33kW respectively, which are proportional to their power ratings. Although $\left|(f+\varepsilon_f)'\right|$ and $\left|(V_{dc}-\varepsilon_{V_{dc}})'\right|$ are beyond their limited thresholds, the entire loading condition is not too heavy or too light. This causes Event C to be false. Therefore, the power exchange on DS bus returns to zero.

Case 5: When the DC load changes from 4.57kW to 0.31kW at t=8s, loads in both sides become light. At this instant, $0.5\left[(f+\varepsilon_f)'+(V_{dc}-\varepsilon_{V_{dc}})'\right]$ reaches to 0.9. True Event C activates SPS again. DS1 and DS2 then absorb 2.05kW and 0.58kW surplus power from the DGs. It is noted that, the ratio of absorbed powers 2.05/0.58 is higher than their ratings ratio 3/2. The reason for this is that the instantaneous SoC of DS1 is lower than that of DS2. It should absorb more power in charging mode. The effect of SoC-based droop characteristics for SPS is also verified in this case. Of the gross stored power from

DGs, 1.18kW is from the DC network via IC1, while 1.47kW is from the AC network via IC2. Proportional power sharing throughout AC and DC network can be inferred from 1.75kW output from the AC source and 1.48kW output from the DC source.

5.7. Experiment Verifications

For verifying the proposed distributed control scheme practically, a scaled-down experimental prototype as shown in Figure 5.9 was built up in the laboratory. Since the number of monitored waveforms was enormous for full observation, some variables were displayed in DSpace/ControlDesk, while others were displayed on oscilloscopes. Relevant experimental parameters are listed in Table 5.1. The AC network is formed by a droop controlled DC-AC inverter, rated at 1200W with a frequency range of 49Hz $\leq f \leq$ 51Hz. The DC network is realized by a droop-controlled booster with a rating of 1500W and a voltage range of 285V $\leq V_{dc} \leq$ 315V. On the DS side, a lead-acid battery bank with a rated voltage of 200V and a lithium battery bank with a rated voltage of 100V are connected to the DS bus via battery converters. Their instantaneous SoC were preset as 30% and 70%, respectively, while the rated stored/released power of two storage elements are $\pm$1000W and $\pm$800W, respectively. Two experimental cases were executed, including (1) transient behavior from LPS to LPS+GPS; (2) transient behavior from LPS+GPS to LPS+GPS+SPS. The respective results are shown in Figure 5.11 and 5.12 as below.

Case 1: **LPS → LPS+GPS**

Figure 5.11 shows the network transients when the system changes the operation mode from LPS to LPS+GPS.

Initial State (before t=1s): The AC load is 600W (C5 in Figure 5.11(c)) and the DC load is about 650W (C6 in Figure 5.11(d)). The outputs of the AC and DC sources are around 600W (Figure 5.11(a)) and 650W (shown in Figure 5.11(d)-C5), respectively. The frequency is around 50Hz (shown in Figure 5.11(b)) and the DC voltage is around 300V (shown in Figure 5.11(d)-C4). Since the AC network frequency and DC bus voltage are around their nominal values, there is no power exchanged between the two networks (shown in Figure 5.11(d)-C7). This is reflected by the zero phase current of IC2 (shown in Figure 5.11(d)-C3).

Final State (after t=1s): When AC load changes from 600W to 130W at t=1s, the frequency increases beyond $|(f)'|_g$ =0.2, which is the threshold value for activating GPS operation. After GPS is enabled, the AC source is generating about 350W. For this amount of power, 130W/350W is supplied to the AC load and the rest 220W is transferred to the DC network, supplying the DC load. On the DC side, the outputs of the DC source decreases to 450W. For the DC load, 450W/650W is supplied by the DC source and 200W/650W is fed from the AC network. The AC and DC sources are now generating 350W and 430W, respectively. 350W/450W shows the approximate proportional power sharing with respect to their nominal powers 1200W/1500W.

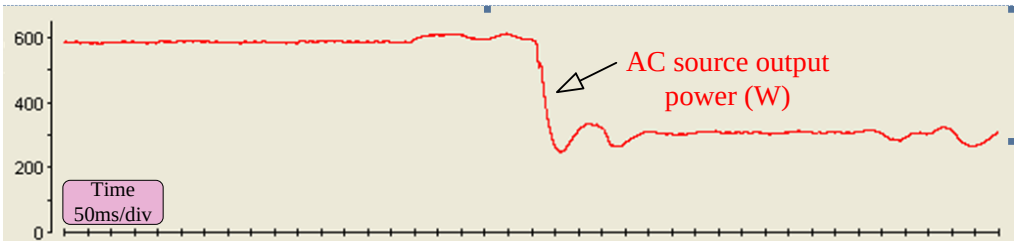

(a)

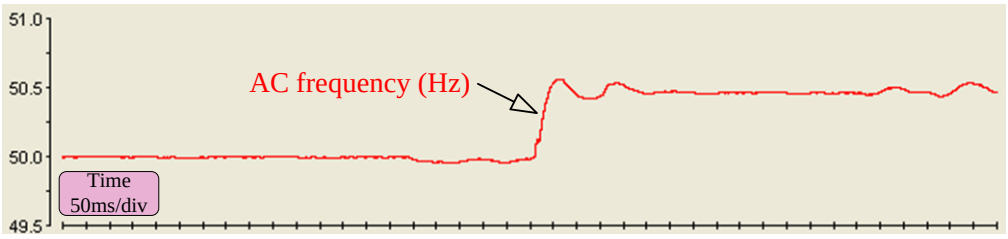

(b)

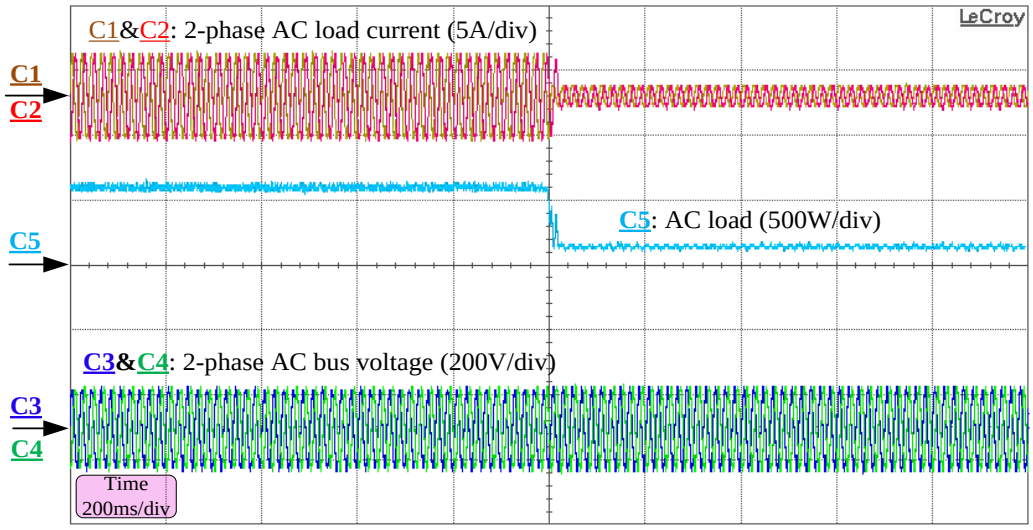

(c)

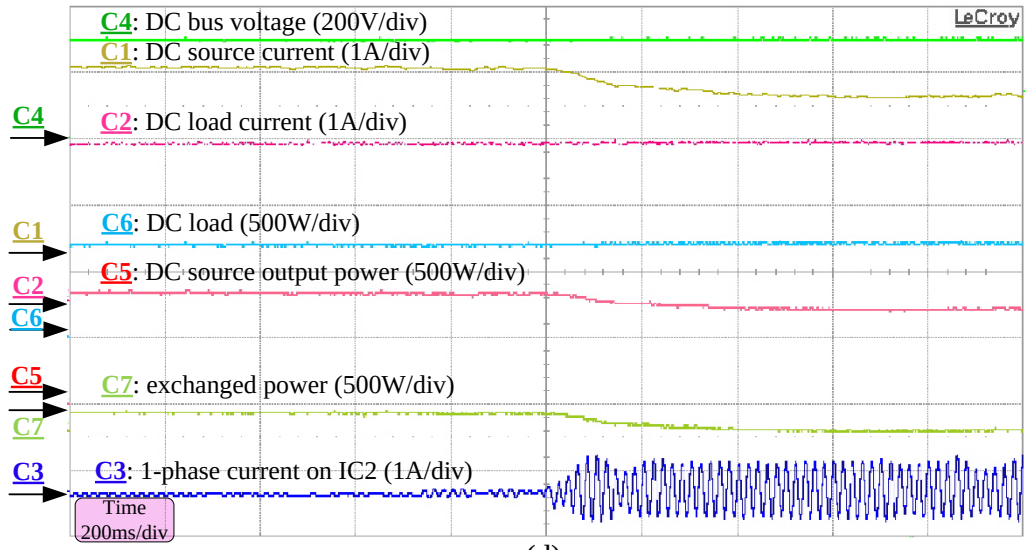

(d)

Figure 5.11. Transients from LPS to LPS+GPS: (a) AC source output power; (b) AC frequency; (c) AC load; (d) profiles of DC network and IC2.

***Case 2:* LPS+GPS →LPS+GPS+SPS**

Figure 5.12 shows the network transients when the system changes the operation mode from LPS+GPS to LPS+GPS+SPS. Since the presence of DS units increases the complexity of variable monitoring, before fully description and explanation on experimental results, the significant variables are hereby labeled as follows: (1) output power of AC source →Figure 5.12(a); (2) AC load →Figure 5.12(c)-C5; (3) AC network frequency →Figure 5.12(b); (4) output power of DC source →Figure 5.12(d)-C5; (5) DC load →Figure 5.12(d)-C6; (6) DC bus voltage →Figure 5.12(d)-C4; (7) power flow on IC1 →Figure 5.12(d)-C3; (8) power flow on IC2 →Figure 5.12(e)-C5; (9) power flow on DS1 →Figure 5.12(f)-C3; (10) power flow on DS2 →Figure 5.12(f)-C5.

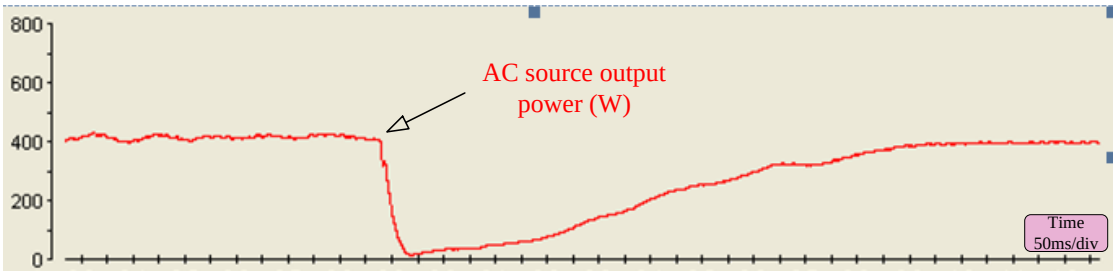

(a)

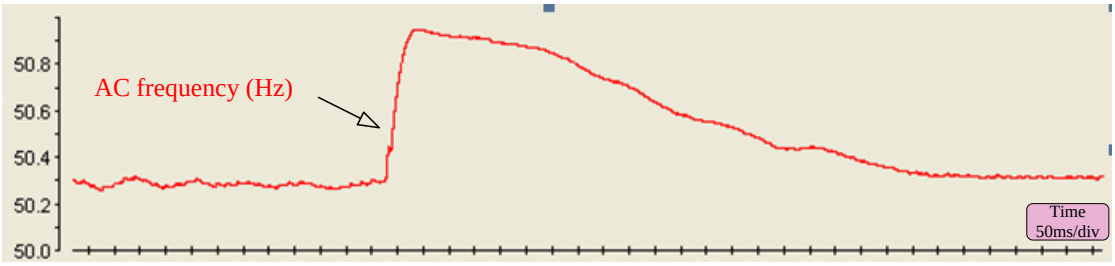
AC frequency (Hz)
50.8
50.6
50.4
50.2
50.0
Time
50ms/div

(b)

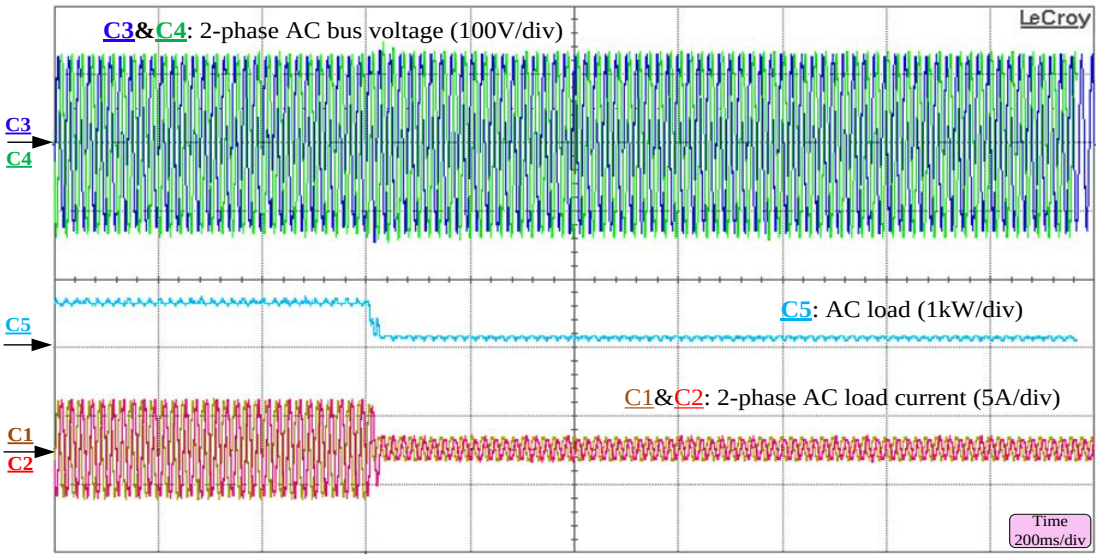
C3&C4: 2-phase AC bus voltage (100V/div)
LeCroy
C3
C4
C5
C5: AC load (1kW/div)
C1&C2: 2-phase AC load current (5A/div)
C1
C2
Time
200ms/div

(c)

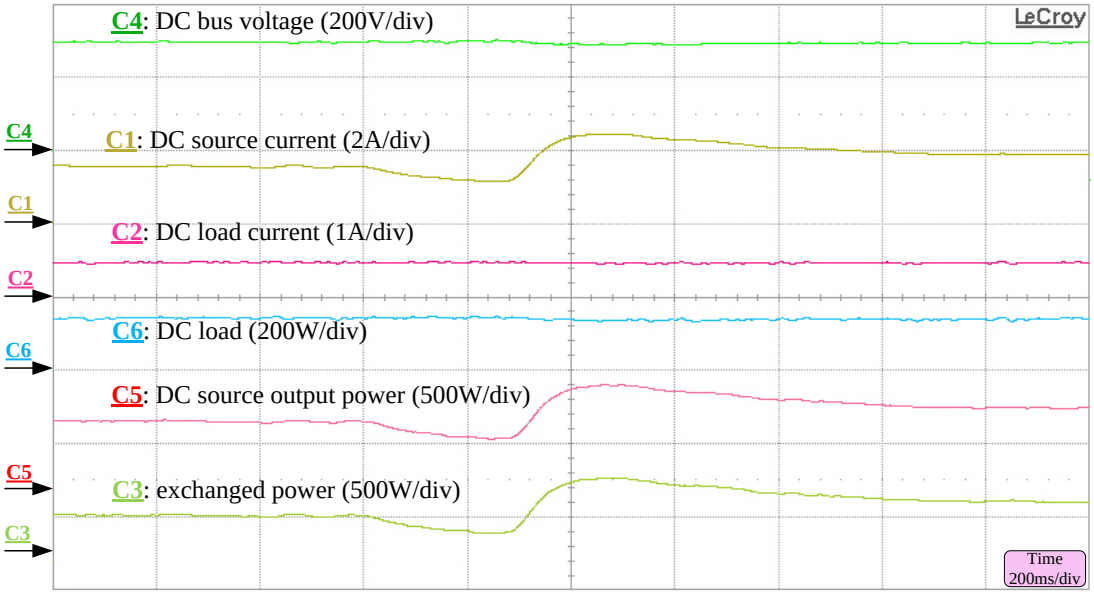
C4: DC bus voltage (200V/div)
LeCroy
C4
C1: DC source current (2A/div)
C1
C2: DC load current (1A/div)
C2
C6: DC load (200W/div)
C6
C5: DC source output power (500W/div)
C5
C3: exchanged power (500W/div)
C3
Time
200ms/div

(d)

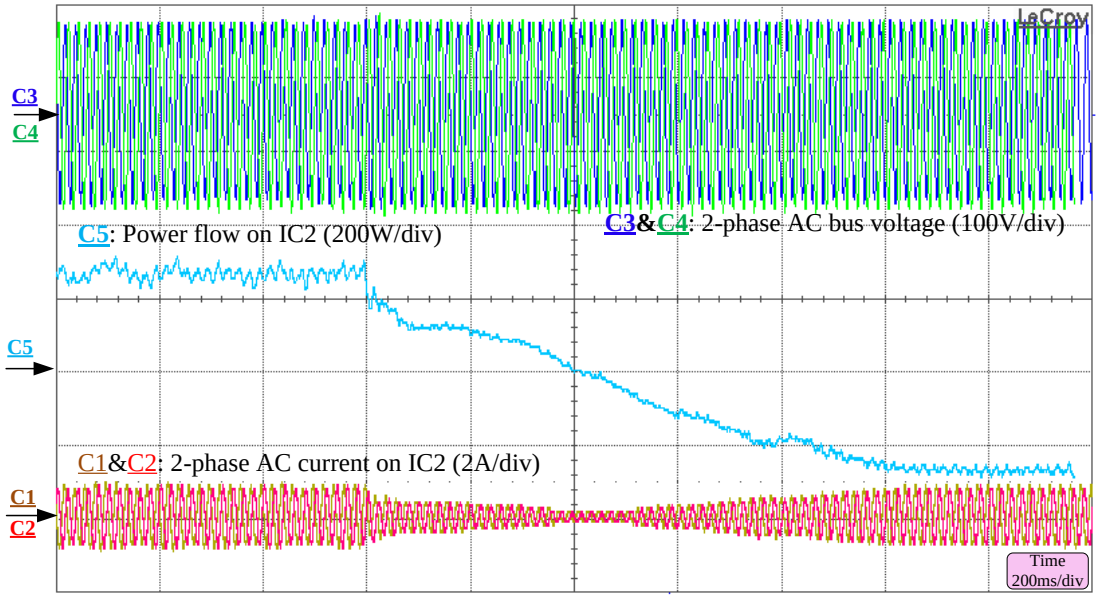

(e)

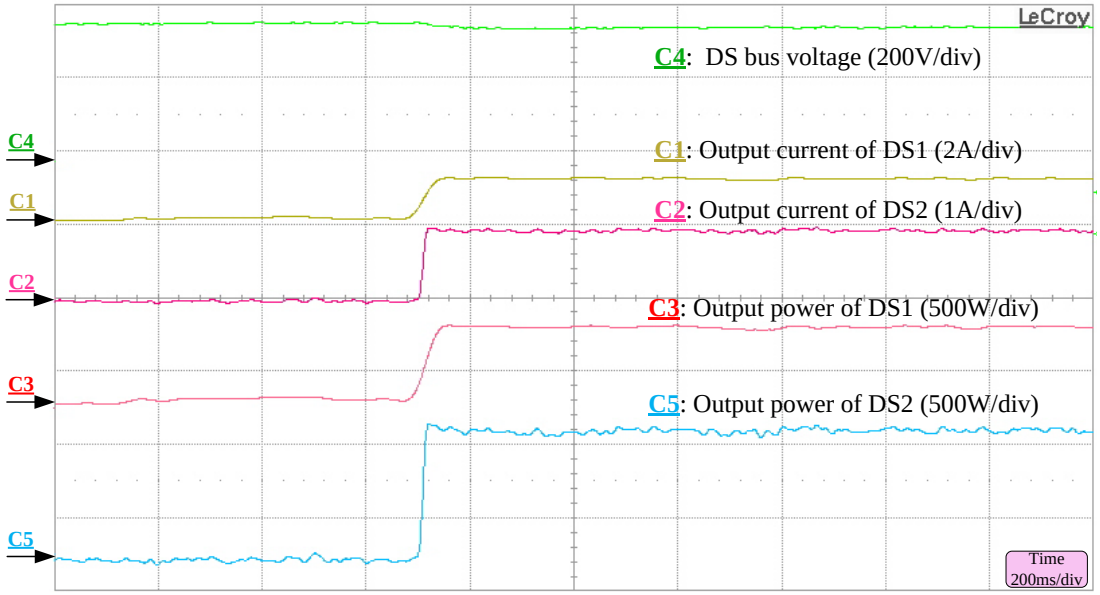

(f)

Figure 5.12. Transients from LPS+GPS to LPS+GPS+SPS: (a) AC source output power; (b) AC bus frequency; (c) AC load; (d) DC network profiles and power flow on IC1; (e) power flow on IC2; (f) power flow on DS1 and DS2.

Initial State (before t=0.6s): The AC and DC loads are set as 700W and 150W, respectively. Since the DC load is too light, GPS operation is activated. The AC and DC sources outputs are 420W and 480W, respectively. Inferred from power flows on IC1 (280W) and IC2 (300W), GPS is maintained by transferring around 300W from the DC

to AC network. The frequency is maintained at around 50.3Hz, which implies that the DC bus voltage is also near the nominal value since $(V_{dc})'$ is enforced to be close to $(f)'$ by GPS control.

Final State (after t=0.6s): The AC load changes from 700W to 150W at t=0.6s. Sudden step-down in AC load results in the frequency increasing beyond $|(f)'|_s$ =0.8 and activates SPS operation. DS1 and DS2 start to absorb around 220W and 350W, respectively. Although the capacity of DS1 is larger than DS2, DS1 absorbs less power than DS2 due to the higher SoC (70%) compared with the SoC of DS2 (30%). Power flow through IC2 changes from 300W to -250W. This implies that the DS network absorbs around 250W from the AC source. Power flow through IC1 changes from 300W to 380W. It should be noted that this amount of power (380W) in this state is fed to DS network. This is different from the situation in initial state, where 300W is transferred to the AC network by GPS control. By feeding 250W and 380W to the DS network, the AC and DC sources are now generating approximately 400W and 530W, respectively, which again verifies GPS among the AC and DC sources. Upon SPS activation, the frequency recovers to 50.33Hz.

The experimental results show that LPS, GPS, SPS and the proposed distributed control can be implemented in practical hybrid AC/DC/DS grids.

5.8. Conclusions

In this chapter, a distributed control strategy for decentralized power management of a hybrid AC/DC/DS system is proposed. LPS in individual network, GPS throughout AC and DC networks, and SPS in DS network are introduced. To avoid unexpected GPS behaviors and reduce the usage of DS, a multi-level power exchange control strategy is developed to schedule the activation sequences among LPS, GPS and SPS. For verification, both simulation and experimental results are provided to show the feasibility of proposed distributed control strategy for autonomous operation of hybrid microgrid system.

Chapter 6 Hybrid AC/DC Active Power Filters (HAPF) for Power Quality Improvement in Hybrid AC/DC Microgrid

6.1. Introduction

The rule of tuning active power flow on the interlinking converter (IC) has been investigated and the global power sharing (GPS) control was proposed to realize GPS throughout entire hybrid AC/DC microgrid in the previous chapters. The further in-depth consideration of power quality issue and alternative solutions in hybrid microgrids are explored in this chapter. In fact, the power quality issue is becoming remarkably important due to the widespread use of semiconductor devices in electric power system. Active power filters (APF) can be an effective way to resolve this issue in the conventional AC system as proposed in the 1980s [95].

Inferred from the concept of APF, the functionality of the IC is broadened to serve as a three-phase three-wire shunt APF, attenuating the harmonic current due to the nonlinear load in the AC sub-grid. By doing so, the harmonic current is injected into the DC side, resulting in voltage ripple in bus voltage due to the ripple power injection if the DC-link capacitance is not large enough. To reduce voltage ripple in DC bus with limited DC-link capacitance, an active DC power filter — DC-link compensator (DLC) is proposed in this chapter for decoupling the harmonic power in the DC-link of the shunt APF. With proper system sizing and design, most of the harmonic power can be cancelled out by the DLC and the electrolytic capacitors used in the conventional shunt APF will be only responsible for filtering very high order or system switching harmonics, and the overall system size can therefore be significantly reduced. The electrolytic capacitors used in the shunt APF system can eventually be replaced by small film capacitors and the final shunt APF system may feature much reduced size and costs, extremely long lifetime and very compact system design.

The organization of this chapter is as follows. The principle of shunt APF is first reviewed and a common problem inherent in the existing shunt APF applications is addressed. To illustrate this common accompanied problem, the minimum requirement of DC-link capacitance for three-phase three-wire shunt APF is then analyzed. In order

to resolve the issues caused by the common shunt APF problem, the concept of DLC and its operation principle are subsequently explained. To verify the effectiveness of the proposed hybrid AC/DC APFs, comprehensive simulation and experimental results are carried out.

6.2. Three-Phase Three-Wire Shunt Active Power Filter (APF) in AC Microgrid

6.2.1. Review of active power filters (APFs)

The concept of APF was first proposed by the authors in [96]. Nowadays, an APF is not a dream but a reality, and its applications are spread all over the world. In principle, the controller of an APF generally determines the compensating current reference in real time, and force the power conditioner to track it accurately. In this sense, an APF can be selective and adaptive, which means that, it can only compensate for the harmonic current from selected nonlinear loads. This section reviews the basic operating principle of APFs which is a necessary process before in-depth illustration of the proposed hybrid AC/DC active power filters system.

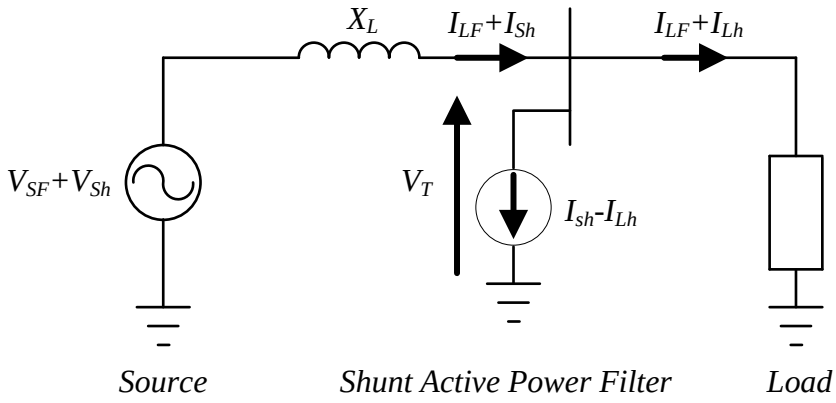

Figure 6.1. Principle of shunt current compensator.

Harmonic currents are primarily generated due to the presence of nonlinear loads and harmonic voltages in the source side. Figure 6.1 draws the basic concept of an APF. A nonlinear load draws a fundamental current component I_{LF} and a harmonic current I_{Lh} from the source. The harmonic current I_{Sh} is induced by the source harmonic voltage V_{Sh}. The APF can compensate both harmonic currents I_{Lh} and $I_{Sh.}$ However, the

principal function of a shunt APF is to compensate of the load harmonic current I_{Lh}. This means that the active filter confines the load harmonic current at the load terminals, hindering its penetration into the power system. For simplicity, the power system is represented only by an equivalent impedance X_L in Figure 6.1. If the load harmonic current I_{Lh} flows through the power system, it produces an additional harmonic voltage drop equal to $X_L\, I_{Lh}$ that further degenerates the load terminal voltage V_T.

The principle of the shunt APF shown in Figure 6.1 is very effective in compensating harmonic currents in loads. However, a shunt active filter that realizes this principle of shunt current compensation should also draw an additional harmonic current I_{Sh} from the source side in order to keep the load terminal voltage sinusoidal and equal to $V_T = V_{SF} – X_L\, I_{LF}$. The harmonic voltage drop appearing across the equivalent impedance becomes equal to the source harmonic voltage if $V_{Sh} = X_L\, I_{Sh}$. In this case, the harmonic voltage components cancel each other, so that the terminal voltage V_T is kept sinusoidal.

If the system impedance X_L is low, the harmonic current I_{Sh} that is drawn by the shunt APF can be very high. This can strongly increase the power rating of the shunt APF, making it impractical. Therefore, if the power system has a high short-circuit capacity, which is the same as saying that it has a low equivalent impedance X_L, or if it has an already significant level of voltage distortion, the active filtering of current I_{Sh} should be left to other filter configurations. For instance, an interesting solution is to install a series active power filter at the load terminals for direct compensation of the harmonic voltage V_{Sh}, instead of the use of a shunt APF to drain the harmonic current I_{Sh} from the power system. Note that the principle of series voltage compensation is the complement of the shunt current compensation. In other words, if the series active filter generates a compensating voltage equal to V_{Sh}, it forces the harmonic current I_{Sh} to become zero. On the other hand, as mentioned above, if the shunt APF draws a compensating current equal to $–I_{Lh}$, it confines the load harmonic current at the load terminals, hindering its penetration into the power system.

According to above description, the shunt APF can be properly controlled to present a selective compensation characteristic. In other words, it is possible to select what

current is to be compensated. That is, it can compensate the source current I_{Sh} and/or the load current I_{Lh}, or even an arbitrarily chosen set of harmonic components. Most applications of shunt APFs are intended to compensate for the load current harmonics produced by a specific load. The shunt APF applied in this chapter is also used for the compensation of load harmonic current.

6.2.2. A Common problem for shunt active power filters (SAPFs)

To date, APF is already a mature technology and has wide adoptions in the power market. Numerous research efforts have been put on this field in order to improve the performance of APF systems, and they are focused on different aspects, e.g. passive/active hybrid configuration to reduce system size and cost [97-100], linear/nonlinear control methods to achieve accurate and fast harmonic compensation [17, 101-104], and various multilevel/cascaded topologies to enable medium voltage high power applications [105-108]etc.

However, a common problem of APF is that very large electrolytic capacitors or even super capacitors have to be installed in the system in order to maintain constant DC bus voltage and provide harmonic compensation, and such capacitors may usually contribute to the major portion of the volume, weight and costs of the whole APF system. The resulting system is unavoidably to be bulky, heavy and costly. Moreover, electrolytic capacitors are known to have relatively larger equivalent series resistance (ESR) compared to other types of capacitors, and high ripple currents, usually exist in APF applications, may flow through the ESR and generate harmful heat that can significantly shorten the working life of such capacitors [109]. Nevertheless, there are very few studies in the literature to discuss the methods for reducing the DC-link capacitance of APFs and the dimensioning of these capacitors are just simply dependent on the system capacity of harmonic compensation. The authors in [110] attempted to adopt a current source type APF to replace the bulky DC-link capacitors. Even though the capacitance can be reduced from 2200μF to 100μF, the designed system required another DC-link inductor that needs to carry huge current (over 100A), which is practically very difficult to implement. Other methods like interleaving more APFs in parallel and using high order LCL-filters with APF have presented in [111, 112] to reduce the size of passive components in the APF system. However, these

methods are more focused on the reduction of AC line filters, which are not dominant elements and usually are much more reliable than those DC-link electrolytic capacitors.

In order to resolve the above-mentioned issues, this chapter presents the concepts of the DC-link compensator, which is essentially an active DC power filter. The proposed DLC system can absorb the harmonic power which is generated by the nonlinear loads in the AC side, leaving only very high order and switching frequency harmonics in the DC-link of the APF. In this case, constant DC bus voltage can be easily achieved with much reduced capacitance and it is even possible to use film capacitors to replace the expensive electrolytic type in the DC-link of APF. Moreover, the DLC itself is constructed with AC capacitors and high frequency MOSFETs can be used instead of IGBTs to further shrink the system size, and there is therefore no bulky passive component required for energy storage or harmonic compensation. Again, small film capacitors are employed in this DLC and the final hybrid AC/DC active filters may feature much reduced weight and costs, extremely long lifetime and very compact system design.

6.2.3. Required DC-link capacitance for SAPFs

As mentioned in the last sub-section, the APF requires relatively constant bus voltage to avoid the over-modulation problem occurring in the converter when compensating high harmonic power in the power system. This can be traditionally achieved through installation of bulky electrolytic capacitors in the DC-link of a conventional APF system or alternatively realized by the proposed DLC system operating coordinately with the conventional APF system. In order to give a comprehensive illustration of the DLC operation principle, the minimum requirements of DC-link capacitance for a typical three-phase three-wire shunt APF system as show in Figure 6.2 is first analyzed in this sub-section.

Assuming that the three-phase supply voltage v_s are balanced and harmonic free,

$$\begin{cases} v_{sa} = \sqrt{2}V_s \sin \omega t \\ v_{sb} = \sqrt{2}V_s \sin(\omega t - 2/3\pi) \\ v_{sc} = \sqrt{2}V_s \sin(\omega t + 2/3\pi) \end{cases} \quad (3\text{-}77)$$

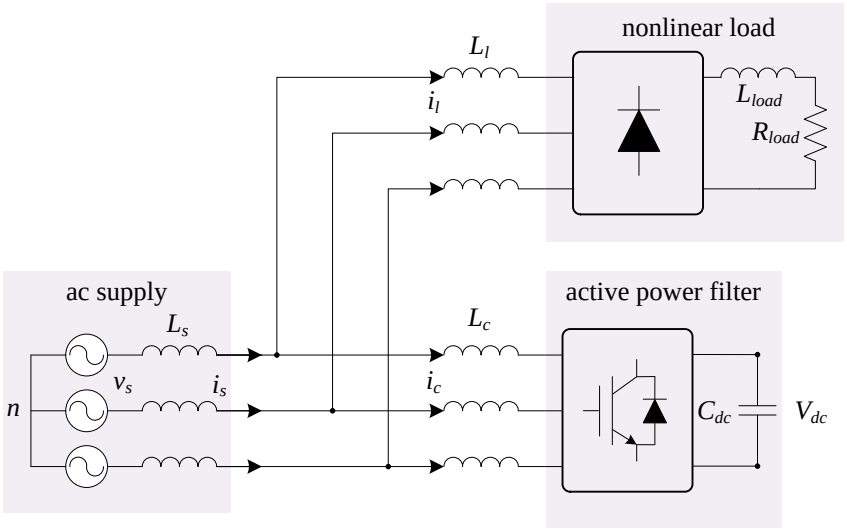

Figure 6.2. A typical three-phase three-wire shunt APF system.

Also, the nonlinear load, e.g. the frond-end stage of a variable speed drive (VSD) system, draws balanced but distorted three-phase currents i_l from the utility grid which can be written as,

$$\begin{cases} i_{la} = \sum_{n=1}^{\infty} \sqrt{2} I_{ln} \sin(n\omega t + \varphi_n) \\ i_{lb} = \sum_{n=1}^{\infty} \sqrt{2} I_{ln} \sin[n(\omega t - 2/3\pi) + \varphi_n] \\ i_{lc} = \sum_{n=1}^{\infty} \sqrt{2} I_{ln} \sin[n(\omega t + 2/3\pi) + \varphi_n] \end{cases} \quad (3\text{-}78)$$

where ω is the fundamental angular frequency, n equals to $6k \pm 1$ with k being an integer, and φ_n represents the phase shift between the n^{th} harmonic current and the grid voltage. The system instantaneous power P_l will simply be the dot product of (6-1) and (6-2) which can then be calculated as,

$$P_l = v_{sa} \cdot i_{la} + v_{sb} \cdot i_{lb} + v_{sc} \cdot i_{lc} = 3V_s I_{l1} \cos\varphi_1 + 3V_s \sum_{n,n\neq 1}^{\infty} I_{ln} \cos[(n \mp 1)\omega t \mp \varphi_n] \quad (3\text{-}79)$$

Clearly, the first term on the right hand side of (6-3) represents the active power demand by the nonlinear loads and the second term will be the harmonic power that needs to be compensated by the APF. It is interesting to observe that the DC-link harmonic power is in the order of 6*k*. This is because, in the stationary reference frame, the 5th harmonic current is the negative sequence component while the 7th is the positive one, and if rotated into synchronous reference frame, both of them will turn out to be the 6th harmonic components [17, 112], which are finally reflected in the DC-link of APF. Assuming that the DC-link capacitance C_{dc} is ideally large and the ripple across the DC bus voltage V_{dc} is very small, then the harmonic current i_{dcn} going into the DC-link capacitors can be calculated as,

$$i_{dcn} = 3V_s \sum_{n,n\neq 1}^{\infty} \frac{I_{ln} \cos[(n \mp 1)\omega t \mp \varphi_n]}{V_{dc}} \tag{3-80}$$

The resulting ripple voltage v_{dcn} will be,

$$v_{dcn} = i_{dcn} \cdot Z_{dcn} = 3V_s \sum_{n,n\neq 1}^{\infty} \frac{I_{ln} \cos[(n \mp 1)\omega t \mp \varphi_n]}{(n \mp 1)\omega C_{dc} V_{dc}} \tag{3-81}$$

It should be noted that the above calculation only applies when the ripple voltage is kept within an acceptable range so that the interaction between i_{dcn} and v_{dcn} can be neglected. Since the 5th and 7th harmonic currents are dominant in the three-phase three-wire power system, they can subsequently lead to the highest 6th order ripple voltage in the DC-link. If it is defined that the voltage variation should be within $\pm a\%$ (typically *a* is less than 1) of the nominal bus voltage, the capacitance can then be simply calculated by only concerning the 6th harmonic power S_{l6} in the DC-link as,

$$C_{dc} \geq \frac{S_{l6}}{6\omega \cdot (V_{dcn} \cdot V_{dc})} = \frac{S_{l6}}{6\omega \cdot (a\% \cdot V_{dc} \cdot V_{dc})} = \frac{100 S_{l6}}{6\omega a V_{dc}^2} \tag{3-82}$$

It is clear from the above equation that for a typical three-phase APF with 400V ($\pm 1\%$) bus voltage, it is expected to need at least 276μF DC-link capacitance to compensate 1KVA 6th harmonic power in a 60Hz AC system. In fact, the actual required DC-link

capacitance should be even larger than the value calculated from (6-6) because the ripple currents have significant impact on the lifetime of electrolytic capacitors and more capacitors should be paralleled to share this burden in a practical system design.

6.3. DC Active Power Filter — DC-link Compensator (DLC)

6.3.1. Principle of DC-link compensator (DLC)

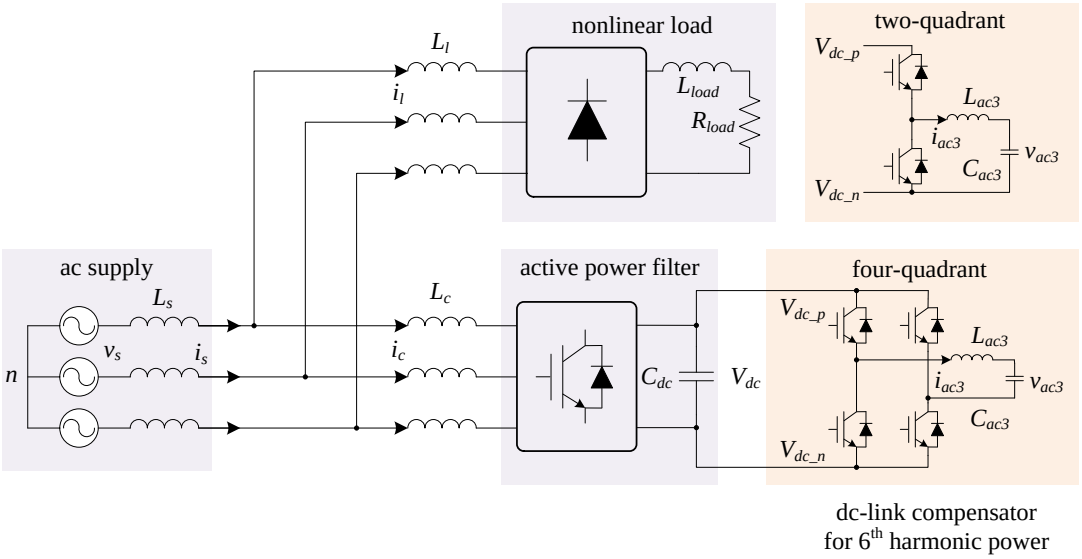

Figure 6.3. The proposed hybrid AC/DC active power filter including a conventional three-phase three-wire SAPF and a DLC.

Equation (6-3) shows that the harmonic power in a three-phase three-wire system is a time-varying component with frequency of 6*k*. Instead of smoothing such harmonics by using large electrolytic capacitors, the DCL is proposed in this section as shown in Figure 6.3 to offer an active approach to sink this harmonic power. As shown in Figure 6.3, the conventional shunt APF is equipped with high frequency AC capacitors and four active switches. In order to provide $6k^{th}$ harmonic power, the four switches will be modulated in such a way that the voltage across the AC capacitor is a sinusoidal waveform with frequency of 3*k*. If it is defined that the voltage v_{ac3k} and current i_{ac3k} of the AC capacitor are in the following form,

$$v_{ac3k} = \sqrt{2}V_{ac3k}\sin(3k\omega t) \tag{3-83}$$

$$i_{ac3k} = C_{ac3k}\frac{dv_{ac3k}}{dt} = 3k\omega C_{ac3k}\sqrt{2}V_{ac3k}\cos(3k\omega t) \tag{3-84}$$

The instantaneous power provided by this DLC can then be calculated as (the power in the filter inductor is very small and negligible),

$$\begin{aligned} v_{ac3k}\cdot i_{ac3k} &= \sqrt{2}V_{ac3k}\sin(3k\omega t)\cdot 3k\omega C_{ac3k}\sqrt{2}V_{ac3k}\cos(3k\omega t) \\ &= 3k\omega C_{ac3k}V_{ac3k}^2\sin(6k\omega t) \end{aligned} \tag{3-85}$$

The above equation indicates that the DLC is also able to provide 6th harmonic power (when k=1) and the amount of harmonic power relates to the AC capacitance with the following equation,

$$C_{ac3} = \frac{S_{l6}}{3\omega V_{ac3}^2} \tag{3-86}$$

Comparing (6-10) with (6-6), it is obvious that for compensating the same amount of 6th harmonic power, the theoretically required capacitance ratio between a conventional APF and the proposed DLC system will be,

$$\frac{C_{dc}}{C_{ac3}} = \frac{100S_{l6}}{6\omega aV_{dc}^2} / \frac{S_{l6}}{3\omega V_{ac3}^2} = \frac{300\omega V_{ac3}^2}{6\omega aV_{dc}^2} = \frac{25}{a}\cdot m_{ac3}^2 \tag{3-87}$$

where $m_{ac3} = \sqrt{2}V_{ac3}/V_{dc}$ is the modulation index applied to the DLC converter. For a very typical system design that has a = 0.5 and m_{ac3} = 0.9, the capacitance can theoretically be reduced by at least 40.5 times with the help of a DLC, and this is also the root reason that why film capacitors can be used to replace the expensive electrolytic ones. Similarly, more DLC converters can be parallel connected into the DC bus and designed in the above manner to compensate 12th, 18th or even higher order harmonics. However, their contributions are generally very limited because the voltage ripples caused by them are insignificant. Therefore, the first $6k^{th}$ harmonic in the DC-link will normally be of interest and become the target of the DLC in this thesis.

Some typical operating waveforms of a DLC designed for 6th harmonic power compensation are shown in the first three plots of Figure 6.4.

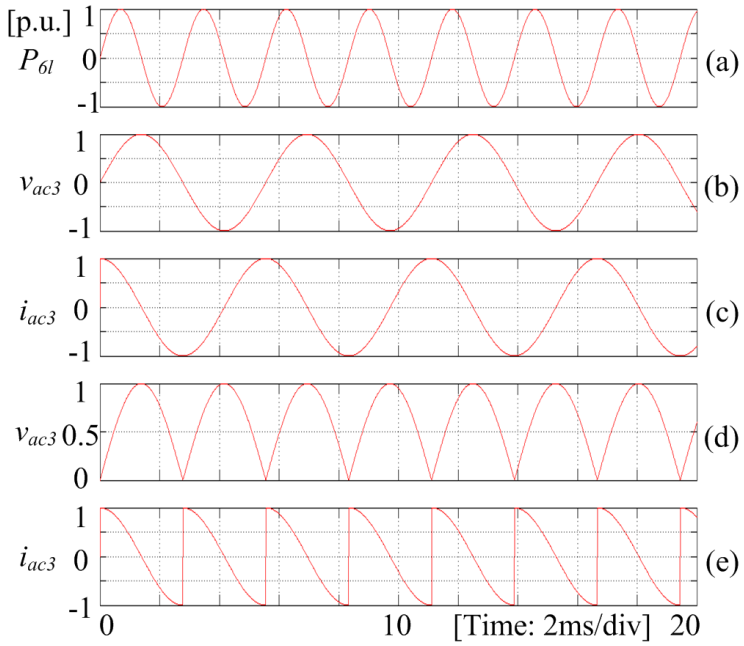

Figure 6.4. Idealized operating waveforms for four-quadrant (b) (c) and two-quadrant (d) (e) DC-link compensators.

It can be seen that the compensator is in effect a four-quadrant converter that can produce both positive/negative voltage/current. A potential problem with this configuration is its increased implementation complexity, because each compensator requires at least four active switches to operate. Since the DLC is particularly designed to control harmonic power and energy, which is determined by the square of the capacitor terminal voltage as expressed by (6-9), and the capacitor voltage is therefore not necessarily to be negative [113]. A simplified configuration of DLC is then derived and drawn in top right of Figure 6.3, which is essentially a two-quadrant converter that can only produce positive capacitor voltage. The typical operating waveforms of the two-quadrant DLC are then presented in Figure 6.4(d) and (e). It is obvious that this type of DLC features exactly the same harmonic compensation capacity. Moreover, this simplification has no impact on the reduction of capacitance, but reduces the cost and complexity of DLC converter. This is the reason that the two-quadrant DLC will be eventually selected as the prototype in the experimental verifications.

6.3.2. Design of DC-link compensator (DLC)

This sub-section presents the design of a three-phase three-wire shunt APF system used in comjunction with the proposed DLC to resolve the system harmonic problem. The overall circuit diagram is shown in Figure 6.3 and the associated system parameters are listed in Table 6.1. The harmonic power propagated into the DC-link of APF can be calculated by multiplying the three-phase currents i_c of APF converter with the three-phase AC supply voltages v_s. The 6th harmonic power can then be extracted by a notch filter (will be elaborated in the following section) tuned at 360Hz and its magnitude is found to be 200 VA. According to (6-6), in order to keep the voltage variation within 0.5%, the required capacitance will be,

$$C_{dc} \geq 100 S_{l6} / 6\omega a V_{dc}^2 = 100 \times 200 \div (6 \times 120\pi \times 0.5 \times 300^2) = 196.49 \mu F \qquad (3\text{-}88)$$

Compared with the minimum required DC-link capacitance derived in (6-12), the closest standard capacitance value is 220μF. As discussed above, the capacitance can be much reduced with the help of the DLC and to compensate the same amount of 6th harmonic power, the required AC capacitance is only,

$$C_{ac3} = S_{l6} / 3\omega V_{ac3}^2 = 200 \div [3 \times 120\pi \times (0.9 \times 300 \div \sqrt{2})^2] = 4.85 \mu F \qquad (3\text{-}89)$$

In this case, a 5μF film capacitor can be used as the AC output capacitor of DLC. Since most of the harmonics can be cancelled out by this AC capacitor, the main task of the DC-link capacitor of the APF is to get rid of very high order and switching harmonics. Therefore, a very small electrolytic capacitor is sufficient, e.g. 30μF, and its main task is to absorb high frequency harmonics. It is even possible to use film type DC-link capacitors with the voltage of a 180Hz sinusoidal waveform. Its magnitude is determined by (6-10) and the phase must be synchronized to the 6th harmonic power generated from the AC side in order to achieve perfect cancellation.

Table 6.1. System Parameters used for Simulation.

Elements	Parameters	Values
AC supply	supply voltage V_s	120 V
	line frequency f	60 Hz
	line impedance L_s	0.2 mH
APF converter	nominal power S_n	3 kVA
	filter inductance L_c	2 mH
	DC-link capacitance C_{dc}	33 μF
	DC-link voltage V_{dc}	400 V
DC-link compensator	filter inductance L_{ac3}	0.5 mH
	AC capacitance C_{ac3}	5 μF
	capacitor voltage V_{ac3}	255 V
	switching frequency f_{sw}	25 kHz
nonlinear load (see Fig. 1 for circuit)	smoothing inductance L_l	2 mH
	load inductance L_{load}	10 mH
	load resistance R_{load}	30 Ω
G_{pv}	K_{pv}	0.15
	τ_v	0.015
G_{cf}	K_{cv}	0.1
	τ_c	0.002

6.4. Control of Active Power Filter (APF) and DC-link Compensator (DLC)

With the review of conventional shunt APFs and comprehensive illustration of the proposed DLC operating principle, the control implementations for both APF and DLC will be elaborated in this section as follows.

6.4.1. Control of active power filter (APF)

The APF system is designed to compensate selective harmonic components in the line current through injecting harmonic currents into the grid with the same amplitude but opposite phase to the harmonic current produced by nonlinear loads. The control block diagram of APF system is shown in Figure 6.5, which is composed of an outer DC voltage controller and an inner current controller with parallel connection of fundamental and individual harmonic current controllers.

The DC voltage controller is to maintain the DC-link capacitor voltage constant. Its

realization can be just the stationary frame proportional-integral (PI) controller $G_v(s)$ written in (6-14)

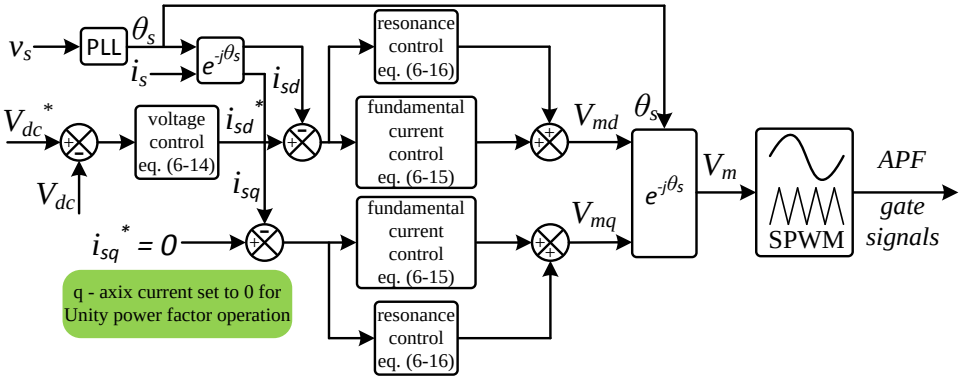

Figure 6.5. Control block diagram of APF.

$$G_v(s) = K_{pv}(1+\frac{1}{\tau_v s}) \tag{3-90}$$

where K_{pv} is the proportional gain, and τ_v is the time constant of the integral term. $G_v(s)$ should be designed to ensure relative slower dynamic response than the inner current controllers, so as to avoid transient interference between them.

The output of the DC voltage controller is then fed into the inner current control loop, acting as the active current reference. For a simple control implementation, only line currents i_s were sensed, replacing the complex control system with two set of sensors to measure both the nonlinear load and APF currents. The reactive current is set as zero to achieve unity power factor operation. The fundamental current is therefore regulated using the following PI controller in the synchronous dq frame rotating at the angular speed of the line voltage v_s:

$$G_{cf}(s) = K_{cv}(1+\frac{1}{\tau_c s}) \tag{3-91}$$

where K_{cv} is the proportional gain, and τ_c is time constant of the integral term.

Proceeding onto the compensation for harmonic currents, it can be alternatively implemented in either stationary or synchronous frame. It was proved in [114] that a

resonant controller in the synchronous frame is more effective, since it represents two equivalent resonant terms in the stationary frame for compensating a pair of harmonics. The harmonic current regulation in this APF system is thus implemented in the synchronous *dq* frame by using multiple paralleled resonant controllers expressed as,

$$G_{ch}(s) = \sum_{n=1}^{k} \frac{K_{ih} s}{s^2 + (6n\omega_n)^2} \tag{3-92}$$

where ω, K_{ih}, and k represent the nominal angular frequency, respective resonant gain, and the highest harmonic order that can be compensated, respectively. The summation of the outputs of fundamental and harmonic current controllers is subsequently transformed back into stationary frame and treated as the reference voltage for modulation of the APF converter.

6.4.2. Control of DC-link compensator (DLC)

As analyzed in previous sections, the DLC proposed in this chapter is to sink the 6th harmonic power which may cause considerable voltage ripple in the DC-link if its capacitance cannot meet the required minimum value. The control of the DLC is on the basis of accurate acquisition of AC capacitor's voltage reference, with which the DC-link compensator can cancel out exactly the same account of 6th harmonic power flowing into the DC-link of APF.

The gross harmonic power propagated into the DC-link of APF can be first calculated as,

$$S_l = v_{sa} \cdot i_{ca} + v_{sb} \cdot i_{cb} + v_{sc} \cdot i_{cc} \tag{3-93}$$

The 6th harmonic power can then be extracted by a notch filter tuned at 6 times of the fundamental frequency.

$$S_{l6} = \frac{K_6 s}{s^2 + K_6 s + (\omega_6)^2} \tag{3-94}$$

where K_6 determines the Q factor of this second order system and it mainly affects dynamic response.

The detection of 6th harmonic power using (6-18) gives rise to the acquisition of AC capacitor's voltage reference, and its root mean square (RMS) value can then be determined by (6-10). It should be noted that, in order to achieve perfect harmonic cancellation, the starting point of this reference voltage must be locked to the positive zero-crossing point of 6th harmonic power, as depicted in Figure 6.4. This can be done through the phase-locked loop (PLL) and voltage controlled oscillator (VCO) elements.

The obtained voltage reference is then fed into a classic dual loop controller to regulate the voltage of the AC capacitor. The outer voltage control loop is realized by a PI controller in order to minimize the steady-state tracking errors, and a simple proportional gain is employed in the inner current loop to improve system stability and dynamic response. It is know that this inner current controller is not necessarily to be PI, proportional resonant (PR) or other advanced controllers because its steady-state error will not affect the tracking accuracy of the outer voltage control loop. Besides this dual loop controller, a feed-forward path of output voltage is also implemented to decouple the system back electromotive force (EMF) so that the closed-loop compensators can have smaller contributions to the duty cycle calculation and the control system can gain more robustness [115]. The final control block diagram for DLC stage is shown in Figure 6.6.

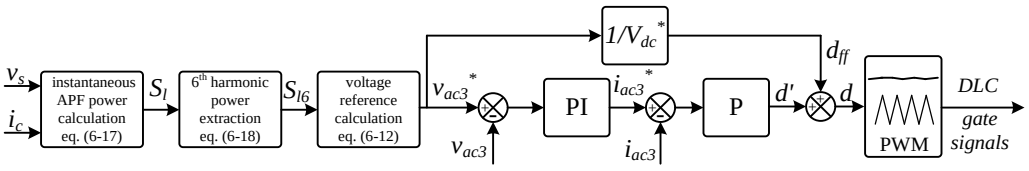

Figure 6.6. Control block diagram of DLC stage.

It should be noted that the DLC can only be activated when the AC capacitor's voltage is in the vicinity of zero volt. Otherwise, a large voltage difference Δv_{ac3} between the voltage reference and the instantaneous voltage of AC capacitor may occur, and very high dv/dt can result in undesired inrush current in the DLC circuit and thus influence

the normal operation of APF. This problem can be prevented by setting a threshold value ε for Δv_{ac3} to control the activation of DLC and expressed as follows (also as explicated in Figure 6.7):

$$A_{DLC} = \begin{cases} 1, & (v_{ac3}^{*} - v_{ac3}) = \Delta v_{ac3} \le \varepsilon \\ 0, & (v_{ac3}^{*} - v_{ac3}) = \Delta v_{ac3} > \varepsilon \end{cases} \tag{3-95}$$

where A_{DLC} is the enable signal for DLC, "1" denotes enabling DLC and "0" denotes disabling DLC.

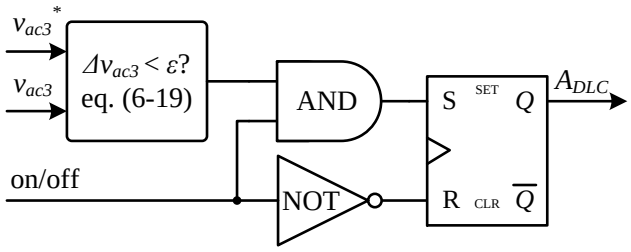

Figure 6.7. Logic operator for activation of DLC stage.

6.5. Simulation Results

The designed system in Sub-section 6.3.2 is simulated in Matlab/Simulink environment to prove the concept of the proposed DLC and the simulated results are shown in Figure 6.8. The relevant parameters used in simulation are listed in Table 6.1.

The APF is running alone with a 33μF DC-link capacitor when t<0.04s. It is obvious that the capacitance is too small to maintain constant bus voltage and the voltage variation in the DC-link of APF can be as high as 30V. This voltage variation in turn affects the current regulation of APF and the total harmonic distortion (THD) in the AC line is found to be 5.01%. In order to mitigate this undesired voltage ripple, the DLC is switched on at t = 0.04s and starts to shift the 6th harmonic power from the DC-link of APF to itself. As can be seen, the voltage variation of APF is dramatically reduced and the 6th voltage ripple across the DC-link is less than 1.2V. The peak-to-peak voltage is only 5V and it is mainly contributed by other high order harmonics. With this much smoother DC-link voltage, the current regulation of APF can be more accurate because of fewer disturbances and the THD of the line current is only 2.06% after operation of

the DC-link compensator, which is a very satisfactory result.

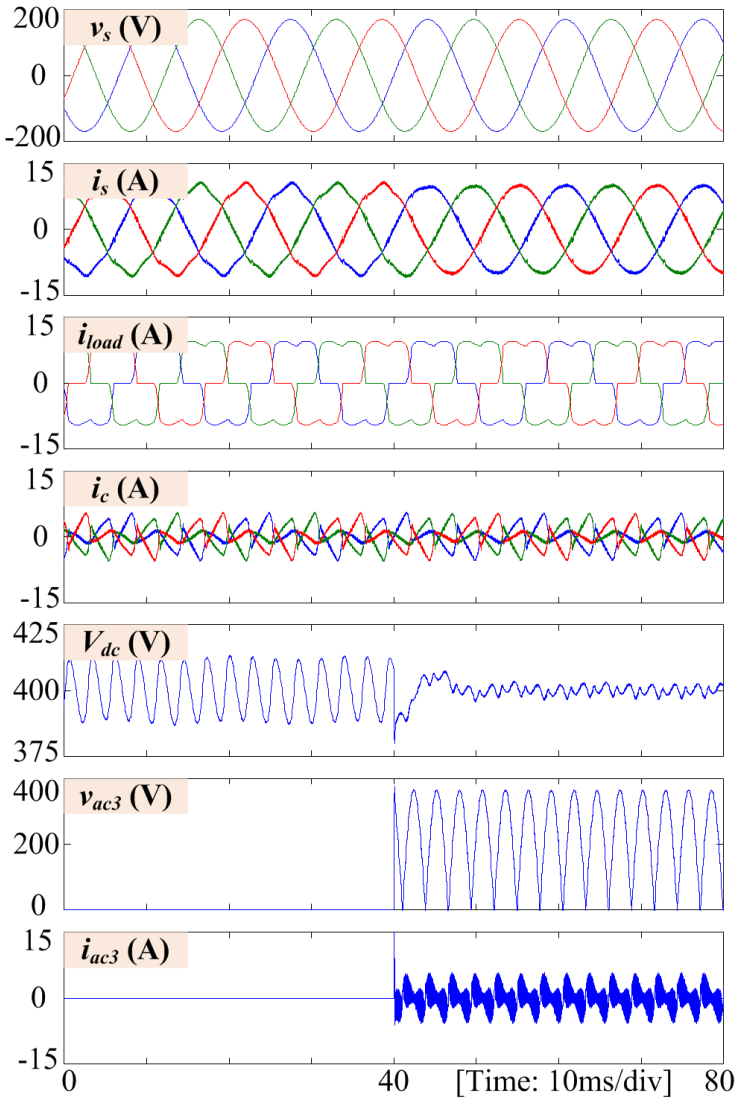

Figure 6.8. Simulated results showing the effectiveness of the proposed DLC concept.

6.6. Prototype Setup and Experiment Verifications

6.6.1. Description of proposed hybrid AC/DC power filter prototype

The proposed hybrid AC/DC active filters system was then validated via proportional scaled-down laboratory tests. The experimental circuit consists of a 2kVA APF, a DLC and a three-phase nonlinear load configured as shown in Figure 6.2. The control algorithms presented in Section 6.4 for both APF and DLC were executed on a dSPACE1103 real-time platform, and the digital signal processor TMS 240F240 was employed with its sampling frequency being set as 12.5kHz in the controller board,

which is the same as the switching frequency. The schematic diagram of overall experimental setup is shown in Figure 6.9. A transfer switch is used in the nonlinear load, allowing the APF system to be subjected to a 100% to 66.7% step-down nonlinear load change. All parameters in the experiment are listed in Table 6.2.

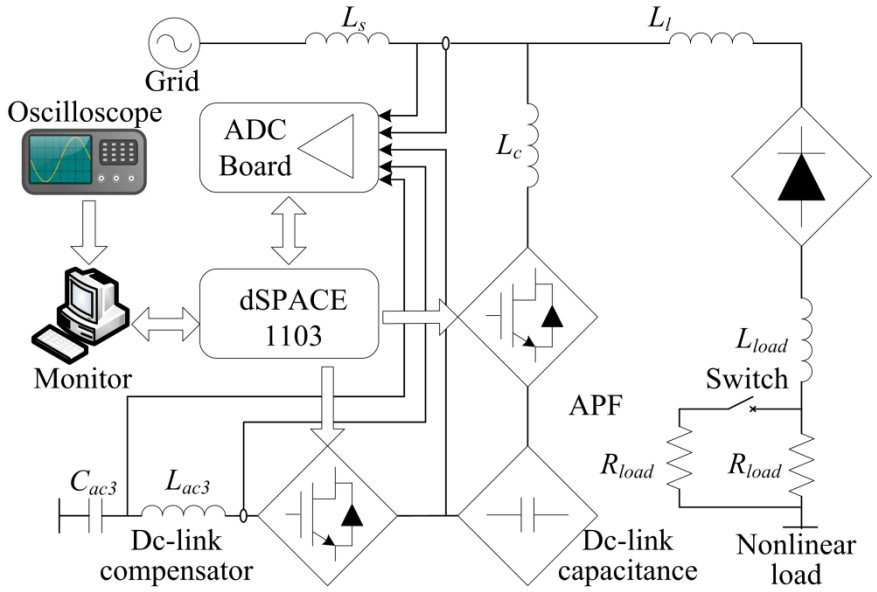

Figure 6.9. Experimental setup of the APF system with a DLC.

Table 6.2. System parameters used for scale-down laboratory experiments.

Elements	Parameters	Values
AC supply	supply voltage V_s	87 V
	line frequency f	60 Hz
	line impedance L_s	0.2 mH
APF converter	nominal power S_n	3 kVA
	filter inductance L_c	2 mH
	DC-link capacitance C_{dc}	33 μF
	dc-link voltage V_{dc}	300 V
DC-link compensator	filter inductance L_{ac3}	0.5 mH
	AC capacitance C_{ac3}	5 μF
	capacitor voltage V_{ac3}	265 V
	switching frequency f_{sw}	12.5 kHz
nonlinear load (see Fig. 1 for circuit)	smoothing inductance L_l	2 mH
	load inductance L_{load}	10 mH
	load resistance R_{load}	30 Ω
G_{pv}	K_{pv}	0.2
	τ_v	0.02
G_{cf}	K_{cv}	0.1
	τ_c	0.001

6.6.2. Experiment Results

The first set of experimental results is shown in Figure 6.10, during which the APF system is running alone and supplying 100% nonlinear load in the steady state. In this case, the designed DC-link capacitance (220μF) of the APF system in Sub-section 6.3.2 was intentionally replaced by two 15μF MKP1848 film type DC-link capacitors from Vishay in order to examine the ripple of DC-link voltage. As anticipated, it is obvious that the capacitance is too small to maintain constant bus voltage and the voltage variation in the DC-link of APF can be as high as approximately 20V.

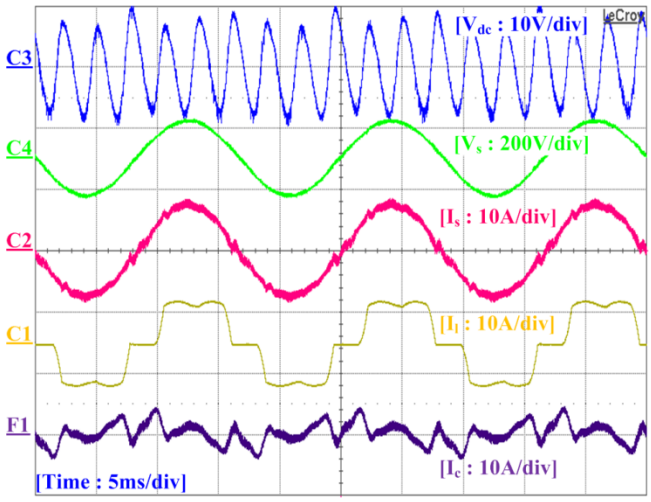

Figure 6.10. Experimental results of steady state performance of APF system with a 33μF dc-link capacitance.

The harmonic content of the DC-link voltage is listed in Table 6.3 and it is clear that the 6^{th} harmonic voltage is dominant with amplitude of 7.76V. Such voltage variation may in turn affect the current regulation of the APF and total harmonic distortion (THD) in the AC line current is found to be 4.77% with 0.16A 5^{th} harmonic current and 0.13A 7^{th} harmonic current, and its detailed spectrum is shown in Figure 6.11.

Table 6.3. Harmonic content in the DC-link voltage.

Unit (Volt)	6^{th}	12^{th}	18^{th}
w/o DLC	7.76	1.12	0.29
w DLC	0.36	0.84	0.23

The DLC was subsequently loaded to mitigate the undesired voltage ripple in the DC-link. Figure 6.12 then shows the steady-state performance of both APF and DLC

stages.

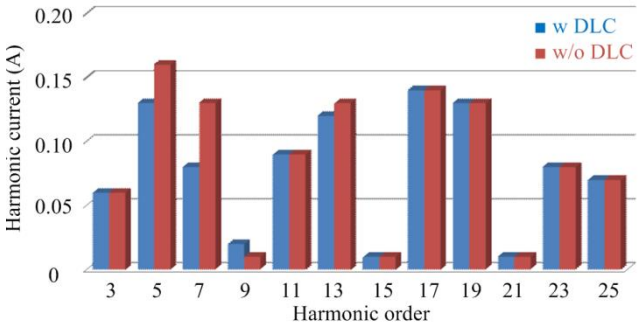

Figure 6.11. Harmonic current spectrum: APF versus APF with a DLC.

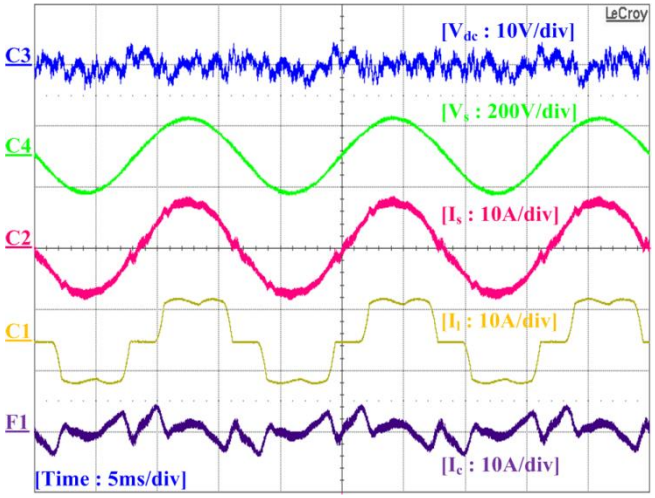

(a)

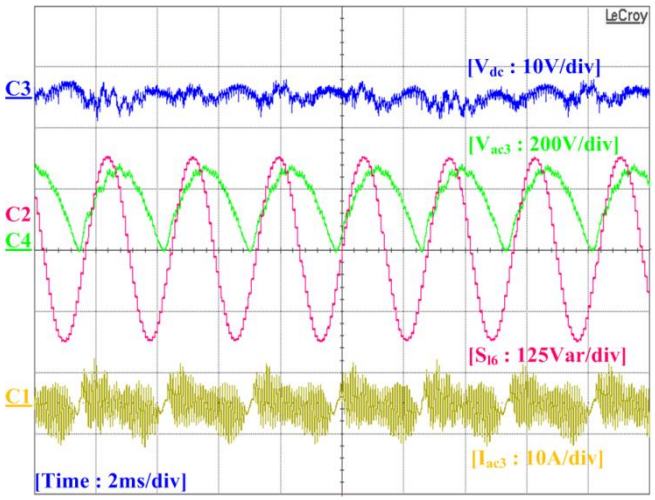

(b)

Figure 6.12. Experimental results of steady state performance of: (a) APF system; (b) dc-link compensator.

As can be seen in Figure 6.12(a), the voltage variation of APF is dramatically reduced since the DLC can shift the 6^{th} harmonic power from the DC-link of APF to itself. The peak-to-peak value of the reduced DC-link voltage is around 6V, which is mainly contributed by other higher order harmonics. With the help of the DLC, the 6^{th} harmonic voltage is suppressed from 7.76V to 0.36V and even the 12^{th} and 18^{th} harmonic voltages are also slightly decreased (see Table 6.3). The corresponding effect is of course better current regulation. With this much smoother DC-link voltage, the current regulation of the APF can be more accurate because of less disturbances and the THD of line current is now 4.18% after the operation of DLC. The 5^{th} and 7^{th} harmonics in the line current are reduced to 0.11A and 0.08A, respectively. On the DLC end, the peak value of stored 6^{th} harmonic power S_{l6} is read approximately as 200VA and this signal is generated from a digital-analog converter (DAC) channel. To sink the exact amount of 6^{th} harmonic power based on (6-10), the voltage of the AC capacitor is controlled as the half sinusoidal waveform with its peak value of 265V, as shown in Figure 6.12(b). These two waveforms are in accordance with those shown in Figure 6.4(a) and (d), and they prove the theoretical studies presented before.

The proposed APF system with DLC enabled is finally subjected to a 100% to 50% step down load change and the experimental results are shown in Figure 6.13. The sudden load decrease causes the DC-link voltage V_{dc} to increase to 360V. This overshoot voltage is slightly higher than expected which is partly due to the small DC-link capacitance used, and also partly due to the non-optimized voltage loop controller design. The DC-link voltage can finally be kept at the nominal value 300V within 5 line cycles and its variation also gets smaller after this transient state. As seen from Figure 6.13(a), the transient voltage spurt may directly affect the current regulation, and the grid current is found to have slight distortion lasting for about half a cycle time. However, this distortion is not obvious and has no impact on the APF system performance. Figure 6.13(b) then demonstrates that the actual voltage of AC capacitor of the DLC can smoothly change from 265V to 183V, which is in accordance to the change of harmonic power produced by the nonlinear load. In this case, the 6^{th} harmonic power can always be absorbed by the DLC and the variation of DC-link voltage can be maintained within an acceptable range at any load conditions.

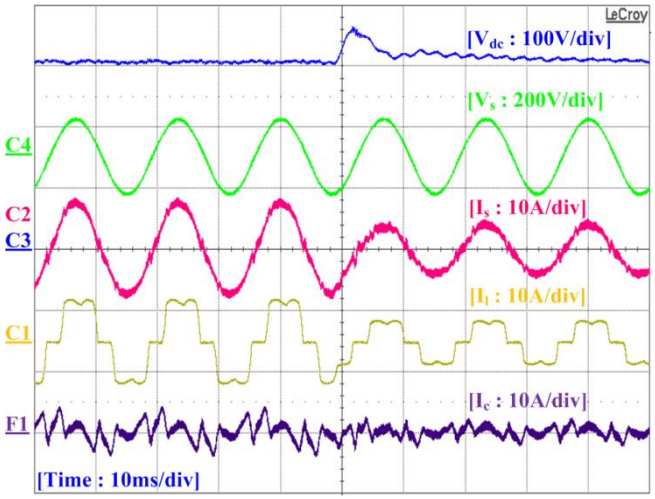

(a)

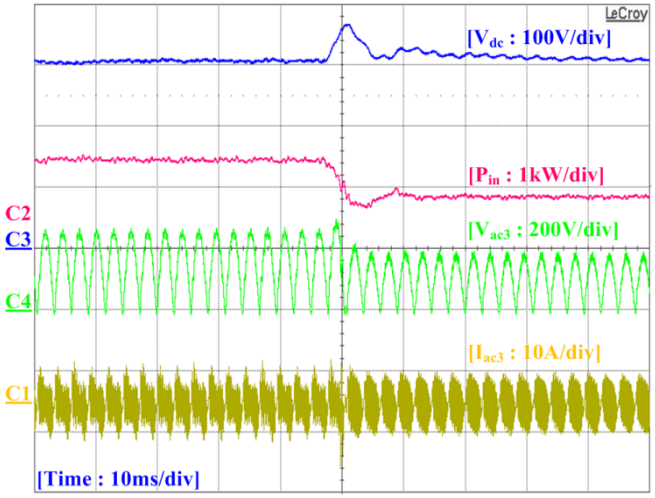

(b)

Figure 6.13. Experimental results of proposed APF system with a DLC when subjected to a 100% to 50% step-down load change.

6.7. Conclusions

This chapter presented a hybrid AC/DC active power filter which is the combination of a conventional APF in three-phase three-wire power systems and a proposed DLC. The attractiveness of the presented system is the significant capacitance reduction which can be achieved in the APF without compromising its performance and adding implementation complexity. The demonstrated results show that good harmonic compensation can be accomplished with only a 30μF DC-link capacitor and a 5μF AC capacitor used in the hybrid active filters system. Moreover, with the help of film

capacitors, the reliability of APF can be enhanced, and its lifetime can be expanded and the system weight and costs can all be reduced in the long term running, making it a very promising system solution for power quality issues.

Chapter 7 Conclusions and Recommendations

7.1. Conclusions

A hybrid AC/DC microgrid features higher operation efficiency, better integration compatibility, more power capacity and control flexibilities to fulfill the overall system reliability and power quality requirements which can hardly be achieved by any individual microgrid or single DG system. The core point of the research work in this thesis is to develop proper control strategies for reliable and efficient operations of hybrid microgrids whose potential benefits have not been exploited in previous literature researches.

In Chapter 2, the concept of hybrid AC/DC microgrid is introduced after an introductory review of DG and microgrid system. The feasibility of existing AC or DC architecture including their relevant advantages and various applications is summarized. An example of hybrid microgrid is then given to show its basic components as well as typical overall structure. The main advantages of the proposed hybrid AC/DC microgrids are subsequently summarized as: 1) higher conversion efficiency because of the elimination of unnecessary multi-conversion processes; 2) simplification of equipment and cost reduction of electronic products because of the elimination of front-end rectifiers for DC or ACwC loads in the current AC grid; 3) harmonic attenuation in AC system with the contribution of the interfacing converter which can sink the harmonic current in AC side into DC microgrid.

After an introduction of the proposed hybrid architecture, a hierarchical control scheme is proposed in Chapter 3 for managing reliable and economical operations of a stand-alone DC microgrid. The proposed control scheme includes: 1) Hierarchical Level I (HLI) is the primary control to maintain the bus voltage within specified limits through changing the operation modes of converters. The bus voltage in this level essentially acts as an indicator of supply-demand balance. A wireless control is therefore implemented for reliable operation of the grid; 2) Hierarchical Level II (HLII) is the secondary control to achieve real-time voltage regulation capability for the

system power modules and prioritizations for charge/discharge of the batteries with different SoCs. A reasonable compromise between the maximum power harvesting and effective battery charging is addressed in this level using coordination control based on a central energy management system; 3) Hierarchical Level III (HLIII) handles extreme operation conditions such as sudden load and source change due to system failures through load shedding or ballast.

Upon reliable operation of DC microgrids, the research focus is then moved onto the development of proper control schemes for reliable operation of autonomous hybrid AC/DC microgrids. With this intention, a GPS control is proposed in Chapter 4, where power balance maintenance within each sub-grid and power exchange management between two sub-grids are both taken into account. The power balance within each sub-grid is maintained by means of source droop control for power sharing among DG units in AC or DC sub-grid, while a rule of power exchange between two sub-grids is established and realized by the proposed GPS control. With GPS realization, all sources dispersed in both sub-grids are capable of sharing the total loads throughout the entire hybrid system. By doing so, the obvious advantages can be summarized as: 1) any single point of failure due to overstress in a certain source can be avoided; 2) sources with slower response to load transients are expected to have smaller variations, thus resulting in a short transient period; 3) design of the capacity of each sub-grid will no longer be constrained by respective local load profiles. Rather, their capacities can be chosen according to the entire load profiles since DGs in one network can be viewed as the back-up reserve for the other one; 4) all elements are managed in decentralized manner without information exchange. This provides an emergency operation scheme during communication failures for complex system with mass communications.

Concerning variable random loads and intermittent renewable sources, the hybrid microgrid can hardly be fully autonomous without DSs for energy buffering, power balancing and fault riding-through. With the consideration of integrating DSs into hybrid AC/DC system, a three-bus AC/DC/DS hybrid infrastructure is proposed in Chapter 5. In this layout, DGs and DSs with the same type are placed in the relevant AC, DC or DS bus in order to avoid the complexity of power management and enforce coincident control scheme to DGs and DSs. For managing the power flow and maintaining reliable operations of such a complex system, Chapter 5 proposes a

distributed control, which includes: 1) a fully decentralized control, in terms of source droop control for LPS in individual AC or DC network, GPS throughout AC and DC network and demand droop control for SPS among DS units, has been developed for decentralized operations; 2) a multi-level power exchange control for managing activation sequences among LPS, GPS and SPS has been proposed to restrain unnecessary power exchange due to GPS and reduce DS operations in SPS. With the proposed distributed control, each power module in the hybrid system can operate independently because of the fully decentralized control. The reliability of the overall hybrid system is therefore enhanced. Moreover, the optimal degree can also be improved because of the power exchange control since unnecessary power exchange and storage usage are reduced.

After the investigation on the basic operation of the hybrid system, further consideration of power quality issue and alternative solutions in hybrid microgrids are addressed in Chapter 6. In that chapter, the functionality of the interlinking converter (IC) is broadened to serve as a shunt APF, attenuating the harmonic current due to the nonlinear load in AC sub-grid. By doing so, the harmonic current will be injected into DC side, result in voltage ripples in the bus voltage due to the ripple power injection. To reduce voltage ripple in DC bus, a DC-link compensator (DLC) is proposed in Chapter 6 for decoupling the harmonic power from the DC-link of the APF. With proper system sizing and design, most of the harmonic power can be cancelled out by the DC-link compensator and the electrolytic capacitors used in the shunt APF system will be only responsible for filtering very high order or system switching harmonics, and the overall system size can therefore be significantly reduced. The electrolytic capacitors used in the shunt APF system can eventually be replaced by small film capacitors and the final system may feature much reduced size and costs, extremely long lifetime and very compact system design.

In a summary, the distributed control strategy and power quality improvement for hybrid AC-DC microgrid have been verified in theory, simulation and experiment, and will definitely facilitate the application and development of hybrid AC-DC microgrid in low voltage distribution systems.

7.2. Recommendations

Systematic research on proper control scheme for reliable operations and power quality improvement of hybrid AC/DC microgrids are carried out in this thesis. Several topics which are worthwhile for further in-depth investigation have not been investigated in this work. Interesting research topics recommended for future study are given as below.

Sources in hybrid AC/DC system are ideal DC sources, which might be impractical in practical applications. It is recommended that the development of proper control schemes should be combined with the development of models of real micro-sources, such as micro-turbine and renewable sources. Characteristics and dynamic response of specific micro-sources should be incorporated with the development of new control schemes. Moreover, distributed storage with different features like high power and high energy can be coordinately managed. The hybridization usage of distributed storages is recommended.

To improve the load sharing accuracy and system transient stability, it is possible to implement the other existing droop methods, such as droop control with virtual output impedance, power derivative and integral terms, and harmonic current sharing, to this hybrid microgrid system. Moreover, most of the research works related to droop control are concentrated on its application with voltage source inverter (VSI). The droop method applied to current source inverter (CSI) is seldom investigated. For the CSI, the *L* filter at AC side can be saved, and therefore, the output impedance of inverter can be reduced. However, the problem with CSI is the input *L* filter must be large. Therefore, it might be interesting to investigate proper control strategy for the purpose of reducing *L* filter while maintaining good performance.

The global stability of DC microgrids with a specific control strategy is affected by the stability of individual source/storage/load converter and their interactions. Stability issues for individual converter have been widely studied in the literatures with primary frequency domain analysis. However, the use of frequency domain analysis is around a single operation point and does not consider the overall interactions and boundary limits

of DC systems. Furthermore, the stability issues due to the mode switching are seldom found in the literature. Developing a theory of stability evolution for multi-converter based DC microgrids becomes challenge especially when the state transitions are taken into account.

In global power sharing control, the stability of AC or DC microgrids depends on the overall stability of the droop controlled parallel DGs, which have been widely investigated in the literatures. Combining both sub-grids with the IC together, the IC can be viewed as the load disturbance for each sub-grid. The global stability issue therefore includes the stability of individual sub-grid and the interactions between both sub-grids through the IC. The global stability analysis throughout hybrid AC/DC microgrids is not as straightforward as the stability analysis for single DG or sub-grid and it is therefore recommended as an interesting research topic for future study.

Finally, only nonlinear loads in AC microgrid are considered in this research work. The load disturbances including both unbalanced and nonlinear loads can be also taken into account in the hybrid microgrid system in the future.

Author's Publications

Journal Publications

1. **C. Jin**, P. Wang, J. Xiao, Y. Tang, and F. H. Choo, "Implementation of hierarchical control in dc microgrids," *IEEE Trans. Ind. Electron.*, vol. PP, no. 99, pp. 1-1. 2013

2. P. Wang, **C. Jin**, D. Zhu, P. C. Loh, and F. H. Choo, "Distributed Control for Autonomous Operation of a Three-Port ac/dc/ds Hybrid Microgrid," *Industrial Electronics, IEEE Transactions on* , vol.PP, no.99, pp.1,1. (early access)

3. Y. Tang, D. Zhu, **C. Jin**, P. Wang, and F. Blaabjerg, "A Three-Level Quasi-Two-Stage Single-Phase PFC Converter with Flexible Output Voltage and Improved Conversion Efficiency," *Power Electronics, IEEE Transactions on* , vol.PP, no.99, pp.1,1. (early access)

4. Y. Tang, F. Blaabjerg, P. C. Loh, **C. Jin**, and P. Wang, "Decoupling of Fluctuating Power in Single-Phase Systems through a Symmetrical Half-Bridge Circuit," *Power Electronics, IEEE Transactions on* , vol.PP, no.99, pp.1,1. (early access)

Conference Publications

1. **C. Jin**, and P. Wang, "Enhancement of low voltage ride-through capability for wind turbine driven dfig with active crowbar and battery energy storage system," in *Proc. Power and Energy Society General Meeting, 2010 IEEE*, 2010, pp. 1-8.

2. **C. Jin**, P. C. Loh, P. Wang, Y. Mi, and F. Blaabjerg, "Autonomous operation of hybrid ac-dc microgrids," in *Proc. Sustainable Energy Technologies (ICSET), 2010 IEEE International Conference on*, 2010, pp. 1-7.

3. P. Wang, X. Liu, **C. Jin**, P. C. Loh, and F. H. Choo, "A hybrid ac/dc micro-grid architecture, operation and control," in *Proc. Power and Energy Society General Meeting, 2011 IEEE*, 2011, pp. 1-8.

4. W. Mo, P. C. Loh, **C. Jin**, P. Wang, and F. Blaabjerg, "Six transformer based asymmetrical embedded z-source inverters," in *Proc. Applied Power Electronics Conference and Exposition (APEC), 2013 Twenty-Eighth Annual IEEE*, 2013, pp. 2273-2279.

5. **C. Jin**, Y. Tang, P. Wang, and X. Liu, "Reduction of Dc-link Capacitance for Three-Phase Three-Wire Shunt Active Power Filters," in *IECON 2013 - 39th Annual Conference on IEEE Industrial Electronics Society* , vol., no., pp., 10-13 Nov. 2013.

6. D. Zhu, Y. Tang, **C. Jin**, and P. Wang, "A High Efficiency Single-Phase PFC Converter for Electric Vehicle Charger Applications," in *IECON 2013 - 39th Annual Conference on IEEE Industrial Electronics Society* , vol., no., pp., 10-13 Nov. 2013.

Bibliography

[1] R. C. Dugan and T. E. McDermott, "Distributed generation," *IEEE Industry Applications Magazine*, vol. 8, no. 2, pp. 19-25, 2002

[2] F. Blaabjerg, R. Teodorescu, M. Liserre and A. V. Timbus, "Overview of control and grid synchronization for distributed power generation systems," *IEEE Trans. Ind. Electron.*, vol. 53, no. 5, pp. 1398-1409, 2006

[3] R. H. Lasseter, "Microgrids,"in *Proc. IEEE Power Engineering Society Transmission and Distribution Conference*, 2002, pp. 305-308

[4] J. M. Carrasco, L. G. Franquelo, J. T. Bialasiewicz, E. Galvan, R. C. P. Guisado, M. A. M. Prats, J. I. Leon and N. Moreno-Alfonso, "Power-electronic systems for the grid integration of renewable energy sources: A survey," *IEEE Trans. Ind. Electron.*, vol. 53, no. 4, pp. 1002-1016, 2006

[5] D. Boroyevich, I. Cvetkovic, D. Dong, R. Burgos, W. Fei and F. Lee, "Future electronic power distribution systems a contemplative view,"in *Proc. Optimization of Electrical and Electronic Equipment (OPTIM), 2010 12th International Conference on*, 2010, pp. 1369-1380

[6] Y. Sozer and D. A. Torrey, "Modeling and control of utility interactive inverters," *IEEE Trans. Power Electron.*, vol. 24, no. 11, pp. 2475-2483, 2009

[7] F. Blaabjerg, Z. Chen and S. B. Kjaer, "Power electronics as efficient interface in dispersed power generation systems," *IEEE Trans. Power Electron.*, vol. 19, no. 5, pp. 1184-1194, 2004

[8] J. A. Peas Lopes, C. L. Moreira and A. G. Madureira, "Defining control strategies for microgrids islanded operation," *Power Systems, IEEE Transactions on*, vol. 21, no. 2, pp. 916-924, 2006

[9] Y. Ito, Y. Zhongqing and H. Akagi, "Dc microgrid based distribution power generation system,"in *Proc. Power Electronics and Motion Control Conference, 2004. IPEMC 2004. The 4th International*, 2004, pp. 1740-1745 Vol.1743

[10] P. Biczel, "Power electronic converters in dc microgrid,"in *Proc. Compatibility in Power Electronics, 2007. CPE '07*, 2007, pp. 1-6

[11] X. Lie and C. Dong, "Control and operation of a dc microgrid with variable generation and energy storage," *IEEE Trans. Power Del.*, vol. 26, no. 4, pp. 2513-2522, 2011

[12] X. Liu, P. Wang and P. C. Loh, "A hybrid ac/dc microgrid and its coordination control," *IEEE Trans. Smart Grid*, vol. 2, no. 2, pp. 278-286, Jun. 2011

[13] D. Salomonsson, L. Soder and A. Sannino, "An adaptive control system for a dc microgrid for data centers," *IEEE Trans. Ind. Appl.*, vol. 44, no. 6, pp. 1910-1917, Nov. 2008

[14] P. Wang, L. Goel, X. Liu and F. H. Choo, "Harmonizing ac and dc: A hybrid ac/dc future grid solution," *Power and Energy Magazine, IEEE*, vol. 11, no. 3, pp. 76-83, May 2013

[15] J. M. Guerrero, L. Huang and J. Uceda, "Control of distributed uninterruptible power supply systems," *IEEE Trans. Ind. Electron.*, vol. 55, no. 8, pp. 2845-2859. Aug. , 2008

[16] J. Schonberger, R. Duke and S. D. Round, "Dc-bus signaling: A distributed control strategy for a hybrid renewable nanogrid," *IEEE Trans. Ind. Electron.*, vol. 53, no. 5, pp. 1453-1460, Oct. 2006

[17] C. Lascu, L. Asiminoaei, I. Boldea and F. Blaabjerg, "High performance current

controller for selective harmonic compensation in active power filters," *IEEE Trans. Power Electron.*, vol. 22, no. 5, pp. 1826-1835, 2007

[18] T. McNichol: 'Ac/dc: The savage tale of the first standards war' (John Wiley and Sons, 2006)

[19] M. E. Baran and N. R. Mahajan, "Dc distribution for industrial systems: Opportunities and challenges," *IEEE Trans. Ind. Appl.*, vol. 39, no. 6, pp. 1596-1601, Nov. 2003

[20] R. S. Balog, W. W. Weaver and P. T. Krein, "The load as an energy asset in a distributed dc smartgrid architecture," *IEEE Trans. Smart Grid*, vol. 3, no. 1, pp. 253-260, Mar. 2012

[21] A. Sannino, G. Postiglione and M. H. J. Bollen, "Feasibility of a dc network for commercial facilities," *IEEE Trans. Ind. Appl.*, vol. 39, no. 5, pp. 1499-1507, Sep. 2003

[22] P.-W. Lee , Y.-Z. Lee and B.-T. Lin, "Power distribution systems for future homes,"in *Proc. IEEE Int. Conf. Power Electronics and Drive Systems, (PEDS '99)*1999, pp. 1140-1146

[23] H. Kakigano, Y. Miura and T. Ise, "Configuration and control of a dc microgrid for residential houses,"in *Proc. Transm. Distrib. Conf.Expo.: Asia Pacific*, 2009, pp. 1-4

[24] K. Engelen, E. Leung Shun, P. Vermeyen, I. Pardon, R. D'Hulst, J. Driesen and R. Belmans, "The feasibility of small-scale residential dc distribution systems,"in *Proc. IEEE Annu. Conf. Ind. Electron, (IECON)*, 2006, pp. 2618-2623

[25] H. Valderrama-Blavi, J. M. Bosque, F. Guinjoan, L. Marroyo and L. Martinez-Salamero, "Power adaptor device for domestic dc microgrids based on commercial mppt inverters," *IEEE Trans. Ind. Electron.*, vol. 60, no. 3, pp. 1191-1203, Mar. , 2013

[26] D. J. Hammerstrom, "Ac versus dc distribution systemsdid we get it right?,"in *Proc. IEEE Power Eng. Soc. Gen. Meet.*, 2007, pp. 1-5

[27] P. Tulpule, S. Yurkovich, J. Wang and G. Rizzoni, "Hybrid large scale system model for a dc microgrid,"in *Proc. American Control Conf. (ACC)*, 2011, pp. 3899-3904

[28] T. M. Gruzs and J. Hall, "Ac, dc or hybrid power solutions for today's telecommunications facilities,"in *Proc. IEEE Int.Telecommun. Energy Conf. (INTELEC)*, 2000, pp. 361-368

[29] D. Salomonsson and A. Sannino, "Low-voltage dc distribution system for commercial power systems with sensitive electronic loads," *IEEE Trans. Power Del.*, vol. 22, no. 3, pp. 1620-1627, Jul. 2007

[30] H. Kakigano, M. Nomura and T. Ise, "Loss evaluation of dc distribution for residential houses compared with ac system,"in *Proc. 2010 Int. Power Electron. Conf. (IPEC)*, Jun. 21-24, 2010, pp. 480-486

[31] A. Pratt, P. Kumar and T. V. Aldridge, "Evaluation of 400v dc distribution in telco and data centers to improve energy efficiency,"in *Proc. IEEE Int. Telecommun. Energy Conf. (INTELEC)*, Sept. 30 - Oct. 4, 2007, pp. 32-39

[32] M. Amin, Y. Arafat, S. Lundberg and S. Mangold, "Low voltage dc distribution system compared with 230 v ac,"in *Proc. IEEE Electrical Power and Energy Conf. (EPEC)*, Oct. 3-5, 2011, pp. 340-345

[33] H. Kakigano, Y. Miura and T. Ise, "Low-voltage bipolar-type dc microgrid for super high quality distribution," *IEEE Trans. Power Electron.*, vol. 25, no. 12, pp. 3066-3075, Dec. 2010

[34] A. Kwasinski and C. N. Onwuchekwa, "Effects of instantaneous constant-power

loads on dc micro-grids for sustainable power systems,"in *Proc. 2010 Int. Power Electron. Conf. (IPEC)*, Jun. 21-24, 2010, pp. 862-869

[35] A. Kwasinski and C. N. Onwuchekwa, "Dynamic behavior and stabilization of dc microgrids with instantaneous constant-power loads," *IEEE Trans. Power Electron.*, vol. 26, no. 3, pp. 822-834, Mar. 2011

[36] X. Feng, J. Liu and F. C. Lee, "Impedance specifications for stable dc distributed power systems," *IEEE Trans. Power Electron.*, vol. 17, no. 2, pp. 157-162, Mar. 2002

[37] J. Guerrero, P. C. Loh, T.-L. Lee and M. Chandorkar, "Advanced control architectures for intelligent microgrids—part ii: Power quality, energy storage, and ac/dc microgrids," *IEEE Trans. Ind. Electron.*, vol. 60, no. 4, pp. 1263-1270, Apr. , 2013

[38] T. Ackermann, G. Andersson and L. Söder, "Distributed generation: A definition," *Electric Power Systems Research*, vol. 57, no. 3, pp. 195-204, 2001

[39] W. El-Khattam and M. M. A. Salama, "Distributed generation technologies, definitions and benefits," *Electric Power Systems Research*, vol. 71, no. 2, pp. 119-128, 2004

[40] G. Pepermans, J. Driesen, D. Haeseldonckx, R. Belmans and W. D'Haeseleer, "Distributed generation: Definition, benefits and issues," *Energy Policy*, vol. 33, no. 6, pp. 787-798, 2005

[41] C. Smallwood, "Distributed generation in autonomous and nonautonomous micro grids,"in *Proc. IEEE Rural Electric Power Conference*, 2002, pp. D1-D1_6

[42] P. P. Barker and R. W. De Mello, "Determining the impact of distributed generation on power systems: Part 1 - radial distribution systems,"in *Proc. Seattle, WA*, 2000, pp. 1645-1656

[43] M. T. Doyle, "Reviewing the impacts of distributed generation on distribution system protection,"in *Proc. Chicago, IL*, 2002, pp. 103-105

[44] Y. Zoka, H. Sasaki, N. Yorino, K. Kawahara and C. C. Liu, "An interaction problem of distributed generators installed in a microgrid,"in *Proc. IEEE International Conference on Electric Utility Deregulation, Restructuring and Power Technologies (DRPT2004)*, 2004, pp. 795-799

[45] N. Hatziargyriou, "Microgrids," *IEEE Power and Energy Magazine*, vol. 6, no. 3, pp. 26-30, 2008

[46] A. Arulampalam, M. Barnes, A. Engler, A. Goodwin and N. Jenkins, "Control of power electronic interfaces in distributed generation microgrids," *International Journal of Electronics*, vol. 91, no. 9, pp. 503-523, 2004

[47] R. H. Lasseter: 'Integration of distributed energy resources — the certs microgrid concept'. Available: http://certs.lbl.gov/certs-pubs.html, 2002

[48] R. H. Lasseter and M. Erickson: 'Integration of battery-based energy storage element in the certs microgrid'. Available: http://certs.lbl.gov/certs-pubs.html, 2009

[49] J. D. Kueck: 'Microgrid energy management system'. Available: http://certs.lbl.gov/certs-pubs.html, 2003

[50] H. Jiayi, J. Chuanwen and X. Rong, "A review on distributed energy resources and microgrid," *Renewable and Sustainable Energy Reviews*, vol. 12, no. 9, pp. 2465-2476, 2008

[51] R. H. Lasseter and P. Paigi, "Microgrid: A conceptual solution,"in *Proc. Power Electronics Specialists Conference, 2004. PESC 04. 2004 IEEE 35th Annual*, 2004, pp. 4285-4290 Vol.4286

[52] P. Piagi and R. H. Lasseter, "Autonomous control of microgrids,"in *Proc. Power Engineering Society General Meeting, 2006. IEEE*, 2006, pp. 8 pp.

[53] S. Xu, S. Lukic and A. Q. Huang, "Dc zonal micro-grid architecture and control,"in *Proc. IECON 2010 - 36th Annual Conference on IEEE Industrial Electronics Society*, 2010, pp. 2988-2993

[54] J. M. Guerrero, J. C. Vasquez, J. Matas, L. G. de Vicuna and M. Castilla, "Hierarchical control of droop-controlled ac and dc microgrids—a general approach toward standardization," *IEEE Trans. Ind. Electron.*, vol. 58, no. 1, pp. 158-172, Jan. 2011

[55] X. Cao , J. Chen , Y. Xiao and Y. Sun, "Building-environment control with wireless sensor and actuator networks: Centralized versus distributed," *IEEE Trans. Ind. Electron.*, vol. 57, no. 11, pp. 3596-3605, Nov. , 2010

[56] S. K. Mazumder, M. Tahir and K. Acharya, "Master-slave current-sharing control of a parallel dc-dc converter system over an rf communication interface," *IEEE Trans. Ind. Electron.*, vol. 55, no. 1, pp. 59-66, Jan. , 2008

[57] J. M. Guerrero, J. Matas, V. Luis Garcia de, M. Castilla and J. Miret, "Decentralized control for parallel operation of distributed generation inverters using resistive output impedance," *IEEE Trans. Ind. Electron.*, vol. 54, no. 2, pp. 994-1004, Apr. , 2007

[58] J. M. Guerrero, M. Chandorkar, T. Lee and P. C. Loh, "Advanced control architectures for intelligent microgrids—part i: Decentralized and hierarchical control," *IEEE Trans. Ind. Electron.*, vol. 60, no. 4, pp. 1254-1262, Apr. , 2013

[59] L. Hao, C. Bong Jun, Z. Weihua and S. Xuemin, "Stability enhancement of decentralized inverter control through wireless communications in microgrids," *IEEE Trans. Smart Grid*, vol. 4, no. 1, pp. 321-331, Mar. , 2013

[60] T.-F. Wu, Y.-E. Wu, H.-M. Hsieh and Y.-K. Chen, "Current weighting distribution control strategy for multi-inverter systems to achieve current sharing," *IEEE Trans. Power Electron.*, vol. 22, no. 1, pp. 160-168, Jan. , 2007

[61] K. Sun, Z. Li, X. Yan and J. M. Guerrero, "A distributed control strategy based on dc bus signaling for modular photovoltaic generation systems with battery energy storage," *IEEE Trans. Power Electron.*, vol. 26, no. 10, pp. 3032-3045, Oct. 2011

[62] S. Anand, B. G. Fernandes and M. Guerrero, "Distributed control to ensure proportional load sharing and improve voltage regulation in low-voltage dc microgrids," *IEEE Trans. Power Electron.*, vol. 28, no. 4, pp. 1900-1913, Apr. , 2013

[63] J. Bryan, R. Duke and S. Round, "Decentralized generator scheduling in a nanogrid using dc bus signaling,"in *Proc. IEEE Power Eng. Soc. General Meeting*, 2004, pp. 977-982

[64] J.-S. Moon, J.-H. Lee, I.-Y. Ha, T.-K. Lee and C.-Y. Won, "An efficient battery charging algorithm based on state-of-charge estimation for electric vehicle,"in *Proc. Int. Electrical Machines and Systems Conf. (ICEMS)*, Aug. 20-23, 2011, pp. 1-6

[65] P. Waltari, T. Suntio, A. Tenno and R. Tenno, "The effects of intermittent charging on vrla battery life expectancy in telecom applications,"in *Proc. IEEE Int.Telecommun. Energy Conf. (INTELEC)*, 2002, pp. 121-127

[66] M. Bhatt, W. G. Hurley and W. H. Wolfle, "A new approach to intermittent charging of valve-regulated lead-acid batteries in standby applications," *IEEE Trans. Ind. Electron.*, vol. 52, no. 5, pp. 1337-1342, Oct. 2005

[67] S. Armstrong, M. E. Glavin and W. G. Hurley, "Comparison of battery charging

algorithms for stand alone photovoltaic systems,"in *Proc. IEEE Power Electron. Specialists Conf. (PESC)*, Jun. 15-19 2008, pp. 1469-1475

[68] X. Liu, P. Wang, P. C. Loh, F. Gao and F. H. Choo, "Control of hybrid battery/ultra-capacitor energy storage for stand-alone photovoltaic system,"in *Proc. Energy Conversion Congress and Exposition (ECCE), 2010 IEEE*, 2010, pp. 336-341

[69] O. Tremblay, L. A. Dessaint and A. I. Dekkiche, "A generic battery model for the dynamic simulation of hybrid electric vehicles,"in *Proc. Vehicle Power and Propulsion Conference, 2007. VPPC 2007. IEEE*, 2007, pp. 284-289

[70] T. Esram and P. L. Chapman, "Comparison of photovoltaic array maximum power point tracking techniques," *Energy Conversion, IEEE Transactions on*, vol. 22, no. 2, pp. 439-449, 2007

[71] S. Jain and V. Agarwal, "A new algorithm for rapid tracking of approximate maximum power point in photovoltaic systems," *Power Electronics Letters, IEEE*, vol. 2, no. 1, pp. 16-19, 2004

[72] N. Femia, G. Petrone, G. Spagnuolo and M. Vitelli, "Optimization of perturb and observe maximum power point tracking method," *IEEE Trans. Power Electron.*, vol. 20, no. 4, pp. 963-973, 2005

[73] F. Liu , S. Duan , F. Liu , B. Liu and Y. Kang, "A variable step size inc mppt method for pv systems," *IEEE Trans. Ind. Electron.*, vol. 55, no. 7, pp. 2622-2628, 2008

[74] M. C. Chandorkar, D. M. Divan and R. Adapa, "Control of parallel connected inverters in standalone ac supply systems," *IEEE Trans. Ind. Appl.*, vol. 29, no. 1, pp. 136-143, 1993

[75] A. Tuladhar, K. Jin, T. Unger and K. Mauch, "Parallel operation of single phase inverter modules with no control interconnections,"in *Proc. Applied Power Electronics Conference and Exposition, 1997. APEC '97 Conference Proceedings 1997., Twelfth Annual*, 1997, pp. 94-100 vol.101

[76] C.-C. Hua, K.-A. Liao and J.-R. Lin, "Parallel operation of inverters for distributed photovoltaic power supply system,"in *Proc. Power Electronics Specialists Conference, 2002. pesc 02. 2002 IEEE 33rd Annual*, 2002, pp. 1979-1983

[77] J. M. Guerrero, L. Garcia de Vicuna, J. Matas, M. Castilla and J. Miret, "Output impedance design of parallel-connected ups inverters with wireless load-sharing control," *IEEE Trans. Ind. Electron.*, vol. 52, no. 4, pp. 1126-1135. Aug. , 2005

[78] J. M. Guerrero, J. Matas, V. de, x00F, L. G. a, M. Castilla and J. Miret, "Wireless-control strategy for parallel operation of distributed-generation inverters," *IEEE Trans. Ind. Electron.*, vol. 53, no. 5, pp. 1461-1470. Oct. , 2006

[79] A. Tuladhar, J. Hua, T. Unger and K. Mauch, "Control of parallel inverters in distributed ac power systems with consideration of line impedance effect," *IEEE Trans. Ind. Appl.*, vol. 36, no. 1, pp. 131-138, 2000

[80] J. M. Guerrero, L. Garcia de Vicuna, J. Matas, M. Castilla and J. Miret, "A wireless controller to enhance dynamic performance of parallel inverters in distributed generation systems," *IEEE Trans. Power Electron.*, vol. 19, no. 5, pp. 1205-1213, 2004

[81] R. Majumder, B. Chaudhuri, A. Ghosh, G. Ledwich and F. Zare, "Improvement of stability and load sharing in an autonomous microgrid using supplementary droop control loop," *Power Systems, IEEE Transactions on*, vol. 25, no. 2, pp. 796-808, 2010

[82] J. Chen , J. Chen , R. Chen , X. Zhang and C. Gong, "Decoupling control of the

non-grid-connected wind power system with the droop strategy based on a dc micro-grid,"in *Proc. World Non-Grid-Connected Wind Power and Energy Conference, 2009. WNWEC 2009*, 2009, pp. 1-6

[83] P. C. Loh, D. Li, Y. K. Chai and F. Blaabjerg, "Autonomous control of interlinking converter with energy storage in hybrid ac/dc microgrid," *IEEE Trans. Ind. Appl.*, vol. 49, no. 3, pp. 1374-1382. May. , 2013

[84] P. C. Loh, D. Li, Y. K. Chai and F. Blaabjerg, "Autonomous operation of hybrid microgrid with ac and dc subgrids," *IEEE Trans. Power Electron.*, vol. 28, no. 5, pp. 2214-2223. May. , 2013

[85] C. Jin, P. C. Loh, P. Wang, Y. Mi and F. Blaabjerg, "Autonomous operation of hybrid ac-dc microgrids,"in *Proc. IEEE Int. Conf. Sustain. Energy Techno.*, 2010, pp. 1-7

[86] P. C. Loh and F. Blaabjerg, "Autonomous control of distributed storages in microgrids,"in *Proc. IEEE Int. Conf. Power Electron. and ECCE Asia*, May/Jun. 2011, pp. 536-542

[87] S.-J. Ahn, J.-W. Park, I.-Y. Chung, S.-I. Moon, S.-H. Kang and S.-R. Nam, "Power-sharing method of multiple distributed generators considering control modes and configurations of a microgrid," *IEEE Trans. Power Del.*, vol. 25, no. 3, pp. 2007-2016. Jul., 2010

[88] A. Mohamed, V. Salehi and O. Mohammed, "Real-time energy management algorithm for mitigation of pulse loads in hybrid microgrids," *IEEE Trans. Smart Grid*, vol. 3, no. 4, pp. 1911-1922. Dec. , 2012

[89] W. Baochao, M. Sechilariu and F. Locment, "Intelligent dc microgrid with smart grid communications: Control strategy consideration and design," *IEEE Trans. Smart Grid*, vol. 3, no. 4, pp. 2148-2156., Dec. 2012

[90] M. Sechilariu, W. Baochao and F. Locment, "Building integrated photovoltaic system with energy storage and smart grid communication," *IEEE Trans. Ind. Electron.*, vol. 60, no. 4, pp. 1607-1618, Apr. , 2013

[91] R.-J. Wai, S.-J. Jhung, J.-J. Liaw and Y.-R. Chang, "Intelligent optimal energy management system for hybrid power sources including fuel cell and battery," *IEEE Trans. Power Electron.*, vol. 28, no. 7, pp. 3231-3244., Jul. 2013

[92] C. Mid-Eum, K. Seong-Woo and S. Seung-Woo, "Energy management optimization in a battery/supercapacitor hybrid energy storage system," *IEEE Trans. Smart Grid*, vol. 3, no. 1, pp. 463-472., Mar. 2012

[93] J. M. Guerrero, J. Matas, V. Luis Garcia de, M. Castilla and J. Miret, "Decentralized control for parallel operation of distributed generation inverters using resistive output impedance," *IEEE Trans. Ind. Electron.*, vol. 54, no. 2, pp. 994-1004. Apr. , 2007

[94] X. Lu, K. Sun, J. M. Guerrero, J. C. Vasquez, L. Huang and R. Teodorescu, "Soc-based droop method for distributed energy storage in dc microgrid applications,"in *Proc. IEEE Int. Symp. Ind. Electron.*, 2012, pp. 1640-1645

[95] H. Akagi, A. Nabae and S. Atoh, "Control strategy of active power filters using multiple voltage-source pwm converters," *IEEE Trans. Ind. Appl.*, vol. IA-22, no. 3, pp. 460-465, 1986

[96] L. Gyugyi and E. C. Strycula, "Active ac power filters,"in *Proc. IEEE/IAS Annu. Meeting*, 1976

[97] F. Z. Peng, H. Akagi and A. Nabae, "A new approach to harmonic compensation in power systems-a combined system of shunt passive and series active filters," *IEEE Trans. Ind. Appl.*, vol. 26, no. 6, pp. 983-990, 1990

[98] H. Fujita and H. Akagi, "The unified power quality conditioner: The integration

of series and shunt-active filters," *IEEE Trans. Power Electron.*, vol. 13, no. 2, pp. 315-322, 1998

[99] N. He, D. Xu and L. Huang, "The application of particle swarm optimization to passive and hybrid active power filter design," *IEEE Trans. Ind. Electron.*, vol. 56, no. 8, pp. 2841-2851, 2009

[100] H. Fujita and H. Akagi, "A practical approach to harmonic compensation in power systems-series connection of passive and active filters," *IEEE Trans. Ind. Appl.*, vol. 27, no. 6, pp. 1020-1025, 1991

[101] X. Yuan, W. Merk, H. Stemmler and J. Allmeling, "Stationary-frame generalized integrators for current control of active power filters with zero steady-state error for current harmonics of concern under unbalanced and distorted operating conditions," *IEEE Trans. Ind. Appl.*, vol. 38, no. 2, pp. 523-532, 2002

[102] S. Rahmani, N. Mendalek and K. Al-Haddad, "Experimental design of a nonlinear control technique for three-phase shunt active power filter," *IEEE Trans. Ind. Electron.*, vol. 57, no. 10, pp. 3364-3375, 2010

[103] A. Chandra, B. Singh, B. N. Singh and K. Al-Haddad, "An improved control algorithm of shunt active filter for voltage regulation, harmonic elimination, power-factor correction, and balancing of nonlinear loads," *IEEE Trans. Power Electron.*, vol. 15, no. 3, pp. 495-507, 2000

[104] N. Mendalek, K. Al-Haddad, F. Fnaiech and L. A. Dessaint, "Nonlinear control technique to enhance dynamic performance of a shunt active power filter," *Electric Power Applications, IEE Proceedings* -, vol. 150, no. 4, pp. 373-379, 2003

[105] M. E. Ortuzar, R. E. Carmi, J. W. Dixon and L. Moran, "Voltage-source active power filter based on multilevel converter and ultracapacitor dc link," *IEEE Trans. Ind. Electron.*, vol. 53, no. 2, pp. 477-485, 2006

[106] M. Basu, S. P. Das and G. K. Dubey, "Parallel converter scheme for high-power active power filters," *Electric Power Applications, IEE Proceedings* -, vol. 151, no. 4, pp. 460-466, 2004

[107] A. Varschavsky, J. Dixon, M. Rotella and L. Moran, "Cascaded nine-level inverter for hybrid-series active power filter, using industrial controller," *IEEE Trans. Ind. Electron.*, vol. 57, no. 8, pp. 2761-2767, 2010

[108] O. Vodyakho and C. C. Mi, "Three-level inverter-based shunt active power filter in three-phase three-wire and four-wire systems," *IEEE Trans. Power Electron.*, vol. 24, no. 5, pp. 1350-1363, 2009

[109] A. Lahyani, P. Venet, G. Grellet and P. J. Viverge, "Failure prediction of electrolytic capacitors during operation of a switchmode power supply," *IEEE Trans. Power Electron.*, vol. 13, no. 6, pp. 1199-1207, 1998

[110] S. Li, B. Ozpineci and L. M. Tolbert, "Evaluation of a current source active power filter to reduce the dc bus capacitor in a hybrid electric vehicle traction drive,"in *Proc. Energy Conversion Congress and Exposition, 2009. ECCE 2009. IEEE*, 2009, pp. 1185-1190

[111] L. Asiminoaei, E. Aeloiza, P. N. Enjeti and F. Blaabjerg, "Shunt active-power-filter topology based on parallel interleaved inverters," *IEEE Trans. Ind. Electron.*, vol. 55, no. 3, pp. 1175-1189, 2008

[112] Y. Tang, P. C. Loh, P. Wang, F. H. Choo, F. Gao and F. Blaabjerg, "Generalized design of high performance shunt active power filter with output lcl filter," *IEEE Trans. Ind. Electron.*, vol. 59, no. 3, pp. 1443-1452, 2012

[113] P. T. Krein, R. S. Balog and M. Mirjafari, "Minimum energy and capacitance requirements for single-phase inverters and rectifiers using a ripple port," *IEEE*

Trans. Power Electron., vol. 27, no. 11, pp. 4690-4698, 2012

[114] R. Teodorescu, F. Blaabjerg, M. Liserre and P. C. Loh, "Proportional-resonant controllers and filters for grid-connected voltage-source converters," *Electric Power Applications, IEE Proceedings*, vol. 153, no. 5, pp. 750-762, 2006

[115] P. C. Loh and D. G. Holmes, "Analysis of multiloop control strategies for lc/cl/lcl-filtered voltage-source and current-source inverters," *IEEE Trans. Ind. Appl.*, vol. 41, no. 2, pp. 644-654, 2005